Controlling Metamaterials with Radiation and Controlling Radiation with Metamaterials

A *Thesis Submitted*

in Partial Fulfilment of the Requirements

for the Degree of

Doctor of Philosophy

by

Sangeeta Chakrabarti

to the

DEPARTMENT OF PHYSICS

INDIAN INSTITUTE OF TECHNOLOGY KANPUR

May, 2010

CERTIFICATE

It is certified that the work contained in this thesis entitled "**Controlling Metamaterials with Radiation and Controlling Radiation with Metamaterials**" by **Sangeeta Chakrabarti**, has been carried out under my supervision and that this work has not been submitted elsewhere for a degree.

S. Anantha Ramakrishna

Prof. S. Anantha Ramakrishna

Department of Physics

IIT Kanpur

Harshawardhan

Prof. Harshawardhan Wanare

Department of Physics

IIT Kanpur

May, 2010

SYNOPSIS

Name of the student: **Sangeeta Chakrabarti** Roll Number: **Y5209067**

Degree for which submitted: **Doctor of Philosophy**

Thesis Title: **Controlling metamaterials with radiation and controlling radiation with metamaterials**

Department: **Physics**

Thesis Supervisors: **Dr. S. Anantha Ramakrishna**,
Dr. H. Wanare

Month and Year of Thesis Submission: **May 2010**

Metamaterials are a class of artificial structured composite media typically structured at length scales much smaller than the wavelength of the incident radiation. Unlike naturally occurring substances that depend on atomic and molecular resonances for their properties, the electromagnetic response of metamaterials is governed by the geometric resonances of the underlying structure. They effectively behave like homogeneous media when the incident wavelength is much larger compared to the size of the inclusions and can be described by effective medium parameters like an effective permittivity and an effective permeability at almost any frequency. Metamaterials can be designed to have a resonant electric, magnetic or even a chiral and bianisotropic response. The large dispersion of the material parameters near the resonance frequencies enables metamaterials to have properties not usually found in nature. They have paved the way for developing media with a negative index of refraction, super-lenses and electromagnetic cloaks, etc. Their resonant response, however, limits their applicability due to the intrinsically high

levels of dissipation associated with them. In addition, the question of the applicability of effective medium theories to metamaterials, particularly those at optical frequencies, is very important because the strength of the resonances are found to become weaker in metallic structures at high frequencies. Thus, metamaterials need to be designed appropriately in order to be homogenizable. Metamaterials for future applications will be required to have controllable responses with low levels of losses.

In this thesis, the properties of metamaterials, particularly their behaviour at optical frequencies, has been studied and a new paradigm for controlling their response has been presented. It is a well-known fact that metamaterials can be designed to operate at a predetermined frequency. While the low frequency behaviour of metamaterials (when they can be treated as effectively homogeneous media) is comparatively easier to explain theoretically and demonstrate practically, their high frequency response is much more complicated. This is due to the departure of the constituent metal from the Ohmic conductor-like behaviour and the deviations of metamaterials from effective medium theories. The work presented here proposes to increase the versatility of metamaterials by making their properties amenable to control by applied fields as well as reduce the optical losses. The thesis can broadly be divided into two parts. The first part deals with metamaterial behaviour at optical frequencies and schemes using coherent optical processes like coherent absorption, Electromagnetically Induced Transparency or Raman processes of imbedded atomic/ molecular materials for controlling the metamaterial response. Control schemes have been proposed for the magnetic response of two classes of metamaterials, viz., the conventional Split Ring Resonator (SRR)-based metamaterials at infra-red frequencies as well as those consisting of plasmonic loop inclusions at optical frequencies. The case of a plasma-like wire mesh metamaterial and the possibility of dynamically opening pass-bands below the plasma frequency has also been investigated. The second part deals with the transformation of the fields in the electromagnetic response of superstructures of negative and positive index media built up from both electric and magnetic metamaterials. Here, the novel electromagnetic response of checkerboards of positive and negative index media has been analysed from

the point of view of the complementary medium theorem, revealing how it is possible to tailor the transmission of radiation (ideally at any frequency, and for any angle of incidence) across these structures. The large local field enhancements in the system are notable.

The **first chapter** is introductory, where the ideas of negative refractive index and metamaterials with independent electric and magnetic responses have been explained. A discussion on effective medium theories and the procedures for homogenizing metamaterial structures to define effective medium parameters is included. In addition, phenomena such as the bianisotropic response of SRRs and the dispersion of surface plasmons, have been critically discussed. The concepts behind various atomic/molecular phenomena such as coherent control, electromagnetically induced transparency and Raman processes, which have been used later in this thesis as a means of manipulating the response of metamaterials, have also been explained in detail.

In the **second chapter**, a discussion of the behaviour of metallic metamaterials which may possess negative material parameters with the aim of optimizing their performance at high (optical and NIR) frequencies has been presented. This includes a theoretical study of the behaviour of Split Ring Resonator (SRR) based metamaterials and the gradual weakening and eventual breakdown of effective medium theories used to describe these media with increase in frequency. It has been shown that even when the metamaterial is treated as a reasonably effective medium and described by effective medium parameters, the homogenization theories show distinct signs of breaking down. The electric field of the incident radiation begins to interact with the individual structures, affecting the retrieved effective material (dielectric and magnetic) parameters of the SRRs. Next, it is shown that a medium consisting of arrays of split ring resonators in vacuum can have negative phase velocity (suggesting a negative index of refraction) for specific polarizations of the incident field at optical frequencies. The size of the SRR is comparable to the wavelength of the incident radiation and thus, the length scales of this system are such that effective medium theories can no longer be applied. The electric fields interact strongly with the symmetric SRRs at these frequencies. The negative

phase velocity is found to arise from plasmonic excitations of the SRR and it can no longer be explained by invoking the negative permittivity and the negative permeability of the metamaterial. The focussing of light by arrays of SRR (both ordered and disordered), in the manner of the Veselago lens, has also been demonstrated. These results show that the focussing properties and the negative phase velocity arise primarily from excitations of localized resonances and cannot be attributed to purely band structure effects like the all-angle negative refraction. These results have been published in S. Chakrabarti and S.A. Ramakrishna, JNOPM, **14**, 143 (2007) and S. Chakrabarti *et. al.* arXiv:physics/0703003.

In the **third chapter**, a scheme for parametrically controlling the magnetic response of homogenizable SRR-based metamaterials has been proposed and studied in detail. The control scheme consists of using coherent optical fields for driving the resonant permittivity of an embedding dielectric medium. This results in being able to tune the capacitance of the SRR dynamically using an external control field. The response of composite (SRR + resonant dielectric) medium has been studied both analytically as well as numerically. The effect of embedding the metamaterial in the frequency-dispersive background (either Lorentz-type or EIT-like) is manifested in the splitting of the negative permeability band and a modified (frequency-dependent) filling fraction and dissipation factor. The modified material parameters are strongly dependent upon the resonant frequencies and the line width of the embedding medium, while for an embedding medium exhibiting Electromagnetically Induced Transparency (EIT), they also depend on the strength of the coupling field via the Rabi frequency and its detuning. The changes in the magnetic response are found to occur over narrow frequency intervals, which makes them suitable for narrow band applications. However, it is found that the narrow band effects survive the broadening effects of disorder and structural imperfections due to an increase in the filling fraction at resonance. The results are also found to be stable against the large levels of dissipation associated with mesoscopic metallic structures. These results are published in S. Chakrabarti *et. al.*, Optics Express, **16**, 19504 (2008) and S. Chakrabarti *et. al.*, arXiv:1003.2932.

The **fourth chapter** deals with the behaviour and the control of the response of plasmonic metamaterials at optical frequencies. These media have the added advantage of a greater ease of fabrication by self-organization methods compared to SRR-based metamaterials. The behaviour of a plasmonic metamaterial composed of silver nanorods arranged on circular loops has been studied in detail, for both the cases when the magnetic field or when the electric field of the incident radiation is oriented along the axis of the nanorods. In the former case, the loop shows a magnetic resonance arising from the collective plasmonic response of the nanorods. Control over the magnetic response is demonstrated numerically by embedding the loops in a Raman-active medium (CS_2) and using the Inverse Raman Effect. There is a splitting of the magnetic resonance, resulting in the formation of propagating bands within the band gap region of the 'bare' metamaterial. Due to the highly dissipative nature of the effective medium, the new band formed results in a sharp decrease in reflectivity. In the latter case, when the electric field of the incident radiation is aligned along the nanorod axes, the metamaterial is seen to behave like an effective dilute plasma, whose plasma frequency is determined solely by the filling fraction of the metal. We theoretically demonstrate the control of this plasma-like effective response of the metamaterial by making it transmittive in the forbidden frequency region below its plasma frequency by embedding it in a coherent atomic/molecular medium. This provides a large positive dielectric permittivity in the vicinity of the resonance, and renders the effective permittivity positive over a narrow range of frequencies. Processes such as EIT can provide additional control to switch and tune the new transmission bands. This has been demonstrated using Raman processes in sodium vapour infused into the array, and subsequently, the formation of switchable transmission bands has been numerically demonstrated using EIT in the same medium. This has been published in S. Chakrabarti *et. al.*, Optics Letters, **34**, 3728 (2009).

In the **fifth chapter**, a study of the electromagnetic response of 2-D checkerboards of negative refractive index materials has been presented from the viewpoint of the generalized perfect lens theorem or the complementary media theorem. The complementary medium theorem of Pendry and Ramakrishna states that any medium can be

optically cancelled by an equal thickness of material constructed to be an inverted mirror image of the medium, with ϵ and μ reversed in sign. Checkerboards can be arranged in two complementary layers, in which case the transmittance predicted by this exact result is unity. However, these systems are extremely singular and are very sensitive to numerical errors. The ray picture often predicts a result opposite to the full wave solutions of Maxwell's equations and is useless to predict the properties of these systems with very large localized modes. Thus, calculations need to be carried out with very fine levels of discretization in order to get rid of the spurious plasmonic resonances arising due to inadequate discretization and such spurious resonances can obscure the actual behaviour of the system. The focussing effects in 2-D checkerboards of dissipative but homogeneous negative refractive index have been discussed. The results show that the subwavelength focussing is still retained to a large extent, even for high levels of dissipation. These results have also been compared with those obtained for silver checkerboards, where only one parameter (the permittivity) is negative. Imaging by checkerboard structures with small finite extents has also been studied and presented here. These results have been published in S. Chakrabarti *et. al.*, Optics Express, **14**, 12950 (2006), S. Guenneau *et. al.*, PNFA, **5**, 63 (2007) and S. Chakrabarti *et. al.* (to be submitted).

ACKNOWLEDGEMENTS

At the very beginning, I would like express gratitude and appreciation for the people who have been closely associated with me and particularly with the writing of this thesis.

First of all I would like to thank my thesis supervisors Dr. S. Anantha Ramakrishna and Dr. Harshawardhan Wanare for their guidance and criticism. Working with them has been a very enriching and enjoyable experience.

I am grateful to Dr. Amit Dutta and Dr. Sreerup Raychaudhuri for their advice and help whenever I needed it.

I shall always cherish the memories of the days at I spent with my friends Joyoshi, Purbasha, Srirupa, Tirtha, Samriddhi, Jayashis and Sandip, who made life at Presidency College and during M.Sc. at IIT Kanpur enjoyable with their pranks and liveliness. Arpana, Rajni, Richa, Dibyendu, Subhayan-da, Ashok-da, Victor, Lipsa and Uma are some of the people who made 'Ph.D. life' memorable and fun with their company.

I thank my parents Dr. S.K. Chakrabarti and Mrs. Swagata Chakrabarti, and my brother, Saurav, for their unwavering support to me all throughout my academic career. I owe everything to their encouragement and guidance and words are inadequate to express my indebtedness to them. My extended family also deserves a special mention — our dogs, cats, birds and fishes — without whom life would have been drab and monotonous.

Finally, I thank my fiance, Karthick for his support, help and criticism of my work.

INDIAN INSTITUTE OF TECHNOLOGY KANPUR

PUBLICATIONS

1. **Finite checkerboards of dissipative negative refractive index**,
   Sangeeta Chakrabarti, S. Anantha Ramakrishna and S. Guenneau
   Optics Express, **14**, 12950 (2006)

2. **Cloaking and imaging effects in plasmonic checkerboards of negative ϵ and and μ and dielectric photonic crystal checkerboards**,
   S. Guenneau, S. Anantha Ramakrishna, S. Enoch, Sangeeta Chakrabarti, G. Tayeb and B. Gralak
   Photonics and Nanostructures Fundamentals and Applications, **5**, 63 (2007)

3. **Negative refractive index of metamaterials at optical frequencies**,
   S. Anantha Ramakrishna and Sangeeta Chakrabarti
   MRS 2006 Fall , Paper: 0964R0102

4. **Metamaterials with negative refractive index at optical frequencies**,
   S. Anantha Ramakrishna, Sangeeta Chakrabarti and Olivier J.F. Martin
   arxiv.org/abs/physics/0703003

5. **Design of metallic metamaterial structures at high frequencies**,
   Sangeeta Chakrabarti and S. Anantha Ramakrishna
   Journal of Nonlinear Optics and Photonic Materials, **17**, 143 (2008)

6. **Coherently Controlling Metamaterials**,
   Sangeeta Chakrabarti, S. Anantha Ramakrishna and Harshawardhan Wanare
   Optics Express, **16**, 19504 (2008)

7. **Switching a Plasmalike Metamaterial via Embedded Resonant Atoms Exhibiting Electromagnetically Induced Transparency**,
   Sangeeta Chakrabarti, S. Anantha Ramakrishna and Harshawardhan Wanare
   Optics Letters, **34**, 3728 (2009)

8. *Coherent control of metamaterials*,
   Sangeeta Chakrabarti, S. Anantha Ramakrishna and H. Wanare
   Proc. SPIE, **Vol. 7392**, 73921S (2009)

9. **Coherently Controlling Metamaterial Resonances with Light**,
   Sangeeta Chakrabarti, S. Anantha Ramakrishna and Harshawardhan Wanare
   (*submitted to Phys. Rev. A*, 2010)

10. **Visible Transmission of Light Through Gold Nano-checkerboards: Theory and Experiments**,
    Sangeeta Chakrabarti, N. Shukla, S. Anantha Ramakrishna, S. Dhamodharan, V. N. Kulkarni, S. Guenneau, Fanny Guenneau and Stefan Enoch
    (*in preparation*, 2010)

NOTATION

SRR - Split Ring Resonator

MG-theory - Maxwell Garnet theory

NRM - Negative Refractive Index Medium

EIT - Electromagnetically Induced Transparency

ω_S - Stokes frequency

ω_{AS} - Anti-Stokes frequency

NIR - Near Infrared

TMM - Transfer Matrix Method

PML - Perfectly Matched Layers

FEM - Finite Element Method

Contents

List of Figures

List of Tables

Chapter 1

Introduction

The idea of negatively refracting or 'left handed' media had its genesis more than four decades ago in a speculative paper by V. Veselago [1]. According to him, the vectors **E** (electric field), **H** (magnetic field) and **k** (wave vector) of an electromagnetic wave would form a left-handed triad during their propagation through a medium whose material parameters, the permittivity ϵ and permeability μ are both negative. These vectors form a right-handed triad for electromagnetic wave propagation through most isotropic media for which both ϵ and μ are positive. The refractive index of such media would thus be negative, as one could infer from considerations of the wave-vector, **k**. However, the Poynting vector, $\mathbf{S} = \mathbf{E} \times \mathbf{H}$, still points along the forward direction (Fig 1.1). The **S** and **k** are antiparallel and hence, materials with a negative refractive index can be thought of as media that have a negative phase velocity. Media with a negative index of refraction permit the propagation of waves with a reversed wave vector, leading them to be also termed as *backward wave media*. Negative index media can be thought of as extreme cases of anisotropic media (like crystals) which do not usually have **S** and **k** parallel although the media considered here are isotropic. The reversal of the direction of **k** results in several interesting consequences for wave propagation such as a modified Snell's law of refraction for such media, a negative angle for Cerenkov radiation and a reversed Goos-Hänchen shift [2, 3, 4, 5, 6, 7, 8].

Negatively refracting media would also necessarily have to be dispersive and dissipa-

tive in order to conform to the conservation of energy. Otherwise, negative dispersionless material parameters ϵ and μ would imply that the energy density

$$W = \frac{\epsilon_0 \epsilon}{2} E^2 + \frac{\mu_0 \mu}{2} H^2 < 0 \quad \text{(incorrect)}. \tag{1.1}$$

This implies that the permittivity and the permeability must be complex-valued functions of the frequency. The material parameters of causal negatively refracting media must satisfy the famous Kramers-Kronig relations [9]

$$\begin{aligned}
\mathrm{Re}[\epsilon(\omega)] - 1 &= \frac{1}{\pi} \mathcal{P} \int_{-\infty}^{\infty} \frac{\mathrm{Im}[\epsilon(\omega')]\ d\omega'}{\omega' - \omega}, && (1.2)\\
\mathrm{Im}[\epsilon(\omega)] &= -\frac{1}{\pi} \mathcal{P} \int_{-\infty}^{\infty} \frac{\mathrm{Re}[\epsilon(\omega')] - 1\ d\omega'}{\omega' - \omega}, && (1.3)\\
\mathrm{Re}[\mu(\omega)] - 1 &= -\frac{1}{\pi} \mathcal{P} \int_{-\infty}^{\infty} \frac{\mathrm{Im}[\mu(\omega')]\ d\omega'}{\omega' - \omega}, && (1.4)\\
\mathrm{Im}[\mu(\omega)] &= \frac{1}{\pi} \mathcal{P} \int_{-\infty}^{\infty} \frac{\mathrm{Re}[\mu(\omega')] - 1\ d\omega'}{\omega' - \omega} && (1.5)
\end{aligned}$$

(where $\mathcal{P}$ is the Cauchy principal value), for causality to hold. The resonant forms of the dispersive permittivity or the permeability of resonant dielectric or magnetic media obtained for generic modes [9, 10] constituting the negative refractive index medium satisfy the above Kramers-Kronig relations. However, since the integrals in these relations involve frequencies extending upto infinity (as effective medium theories become inapplicable at high frequencies), the Kramers-Kronig relations must be applied to metamaterials carefully.

In the absence of naturally occuring media which could display negative material parameters, Veselago's predictions were regarded as academic curiosities. While naturally occuring materials can possess $\epsilon < 0$ (such as metals below their plasma frequencies), the magnetic response of most media die out at low frequencies (in the GHz range). Veselago's ideas were revitalized in 2000 when Sir John Pendry published his seminal paper about a perfect lens [11] consisting of a slab of material whose refractive index is negative. He showed theoretically that such a slab of material whose refractive index n = -1 has the power to focus all the Fourier components associated with an image,

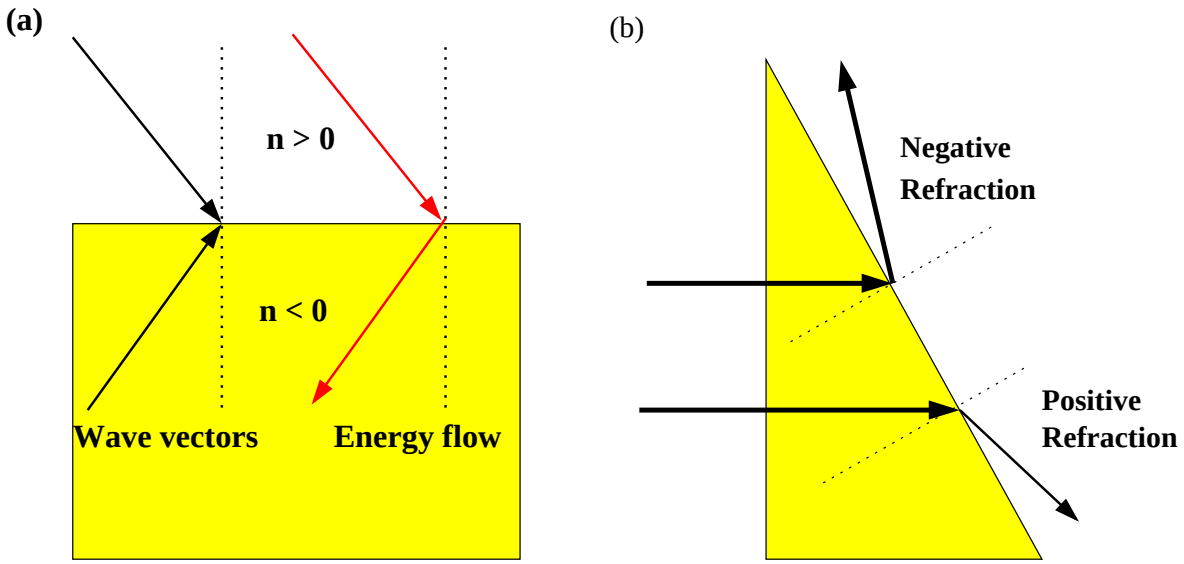

Figure 1.1: (a) Schematic representation of refraction occurring at the interface of a medium whose $n > 0$ and one whose $n < 0$. The energy flow and the wave vectors are oppositely directed in the $n < 0$ medium.
(b) Diagram illustrating the difference between positive and negative refraction. In the case of negative refraction, the refracted ray lies on the same side of the normal as the incident ray.

including all the evanescent ones. Hence, unlike a conventional lens, it is not limited by the wavelength of radiation, and has been called the 'perfect lens'. In the same year, Smith *et. al.* gave the first experimental demonstration of media displaying negative index of refraction [12, 2]. Since then, it is in the context of designing materials with negative material parameters that metamaterials have come to play a decisive role. Here, it is to be noted that simply embedding a negative magnetic medium within a negative dielectric medium does not produce negative refractive index [13]. There are issues of inhomogeneous fields which have to be taken care of [14] before a negative index of refraction can be generated.

Metamaterials, which are essentially structured composite materials exhibiting novel electromagnetic behaviour, is an actively researched subject today [15, 16, 17, 18]. These materials contain structural inhomogeneities which are much smaller compared to the wavelength of incident radiation, and yet much larger than atomic/molecular length-scales. The radiation responds to the macroscopic resonances of these geometric struc-

tures while not being able to resolve their geometric details, enabling their characterization by effective material parameters ϵ_{eff} and μ_{eff}, much like in the case of homogeneous media. In the case of metamaterials, the periodicity of the structure is not particularly important and their response is mainly due to single scatterer localized resonances. This is to be contrasted with the behaviour of periodically arranged dielectric structures in photonic crystals where stop bands and band gaps arise due to Bragg scattering [19, 20] caused by the periodic arrangement. Here, the periodicity of the structure, which is comparable to the wavelength of the impinging radiation, rules out a homogenized description of the medium.

In this thesis, the behaviour and control of metamaterials at optical frequencies has been studied. Schemes for controlling the effective magnetic or electric response of metamaterials using coherent optical processes have been presented in this thesis. The inaccuracies in using a homogenization approach for characterizing the behaviour of magnetic metamaterials at near infrared and optical frequencies has been investigated (Chap. 2). In Chap. 3, parametric control over the effective magnetic response of SRR-based metamaterials, using coherent optical processes has been studied in detail. Chap. 4 contains a study of plasmonic metamaterials and schemes for controlling their magnetic and electric response. All the metamaterials studied in this thesis are metallic. Silver has been considered as the constituent metal as it is one of the least dissipative metals. Finally, in Chap. 5, the transmission properties of checkerboard structures of alternating positive and negative index media have been investigated. In the sections of this chapter that follow, a selection of the basic ideas regarding metamaterials and coherent control processes for the optical control of atomic/ molecular transitions has been presented. This selection is presented with a view to facilitate understanding the effects and phenomena described in the subsequent chapters of this thesis.

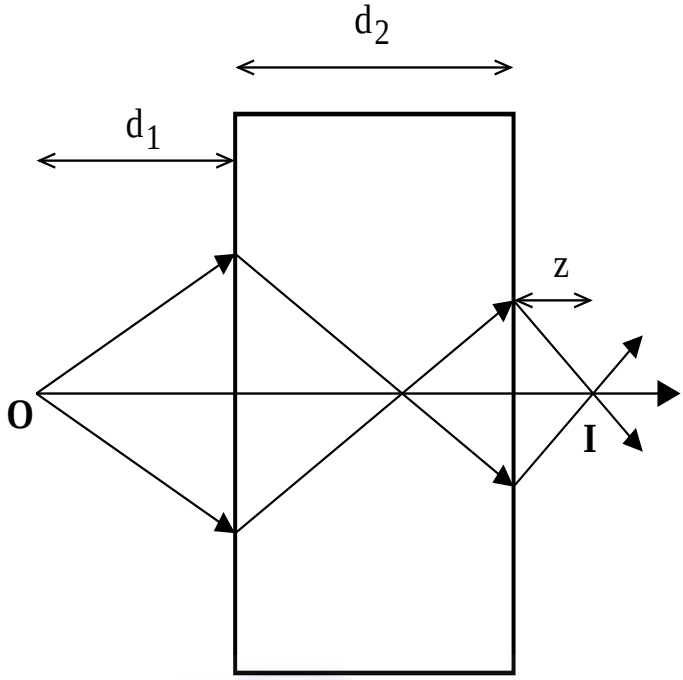

Figure 1.2: The action of the Perfect Lens proposed by Pendry. Characterized by unit transmittivity, this lens focusses the propagating as well as the evanescent modes from an object. The resulting image, which contains the subwavelength features of the object, is 'perfect'. The distance at which the image is formed is $z = d_2 - d_1$.

1.1 The Perfect Lens

Pendry's proposal for a perfect lens [11] that would overcome the Diffraction Limit for conventional lenses and focus even subwavelength features of an object, is a direct consequence of Veselago's idea of a negatively refracting medium. A perfect lens is simply a slab of NRM perfectly impedance-matched to its surroundings so that there is no reflection at the interfaces for a wave incident at any angle or for any transverse wave vector. The figure (Fig. 1.2) shows that an object placed a distance d_1 away from a NRM slab of thickness d_2 comes to a second focus when $z = d_2 - d_1$. The lens is characterized by perfect transmittivity, for both the propagating *and* the evanescent waves and all waves are focussed by it at the frequency when $n = -1$. The perfect refocussing of light occurs as the NRM cancels the phase acquired or amplifies the amplitude lost by the waves in travelling across an equal thickness of vacuum. The focussing of the evanescent waves occurs via surface plasmon modes at the interfaces with vacuum. The slab of NRM cancels the decay of evanescent waves and they emerge

from the slab amplified by the transmission process. This process, by itself, does not violate any energy conservation laws simply because purely evanescent waves do not transport energy in non-dissipative media! It only implies a local field enhancement in the system. Thus, in the perfect lens, both the propagating as well as the evanescent modes contribute to the image and the resolution of the image formed is only limited by the degree of imperfection in the lens (deviation from the condition $\epsilon = -1,\ \mu = -1$). In the limit of large wave-vectors ($k_x \to \infty$), the amplification of the evanescent waves leads to a divergence in the electromagnetic energy due to the absence of a large wave vector cut-off [21]. In principle, however, there is always a cut-off wave-vector $\sim 1/a$, where a is a length scale set by the underlying structure of the metamaterial. The unphysical divergences go away when $\epsilon = \mu = -1$ are understood to be $\epsilon = -1 + i\delta_e, \mu = -1 + i\delta_m$, i.e., the media are taken to be slightly dissipative [22].

Using the technique of co-ordinate transformation [23, 22, 24], it has been shown that it is possible to have perfect lenses in geometries other than the planar slab lens. Perfect lenses having a curved geometry possess the greater advantage of producing a magnified image which contains both the far-field as well as the near-field information. Perfect lenses have been proposed for spherical [25] and cylindrical geometries, as well as perfect corner reflectors consisting of slabs of NRM [26].

1.2 Homogenization of Metamaterials

The interaction of structurally isotropic and non-chiral metamaterials with electromagnetic radiation may be described by two complex parameters ϵ_{eff} and μ_{eff} provided that the radiation has a wavelength (λ) that is much larger compared to the size (a) of the inclusions, i.e., $\lambda \gg a$. The effective material parameters are thus derived from a coarse-grained spatial averaging of the properties of the individual constituent structures. Two levels of averaging are implicit here. First, it is assumed that the inclusions are large enough on a molecular scale to be described by the bulk material parameters of the constituent materials. Second, they are small compared to the lengths over which the

applied fields vary and retardation effects can be neglected. One is able to distinguish only a few average quantities, such as the dipolar, or in some cases, the quadrupolar fields. Thus, we have

$$\langle \mathbf{D} \rangle = \epsilon_0 \tilde{\epsilon}_{\text{eff}} \cdot \langle \mathbf{E} \rangle, \quad \langle \mathbf{B} \rangle = \mu_0 \tilde{\mu}_{\text{eff}} \cdot \langle \mathbf{H} \rangle, \tag{1.6}$$

which define the effective permittivity $\tilde{\epsilon}_{\text{eff}}$ and the effective permeability $\tilde{\mu}_{\text{eff}}$ of the metamaterial. In general, both $\tilde{\epsilon}_{\text{eff}}$ and $\tilde{\mu}_{\text{eff}}$ are tensors. There are, in essence, two approaches which are used for homogenization. The first one involves averaging the fields internal to the structure while the second one makes use of the emergent quantities like the reflection and the transmission coefficients, and obtaining an equivalent effective medium. In order to homogenize the metamaterial, slabs of it which are of finite extent along the direction of propagation of the wave and infinite along the two other directions, are considered. Here we discuss a few techniques for homogenizing metamaterials and assigning effective material parameters to them.

1.2.1 Effective medium theories

(i) *Maxwell-Garnett effective medium theory*: The Maxwell-Garnett theory [27] has very successfully described the properties of dilute composite dielectric media. The composite medium is assumed to consist of small particles (radius $a \ll \lambda$, filling fraction f) of permittivity ϵ_i embedded in a host medium whose permittivity is ϵ_h. This theory incorporates the electromagnetic field distortions due to the dipole fields, yielding an effective permittivity given by

$$\epsilon_{\text{eff}} = \epsilon_h + 3f\epsilon_h \frac{\epsilon_i - \epsilon_h}{\epsilon_i + 2\epsilon_h}. \tag{1.7}$$

The size parameter of the particles (defined as $x = 2\pi a\sqrt{\epsilon_i}/\lambda$) is $\ll 1$, justifying the assumption of a spatially uniform field over the region of the particle. In the case of a

denser composite, the effective dielectric permittivity is found to be

$$\epsilon_{\text{eff}} = \epsilon_h \frac{\epsilon_i(1+2f) + 2\epsilon_h(1-f)}{\epsilon_i(1-f) + \epsilon_h(2+f)}, \tag{1.8}$$

assuming the inclusions to be point particles.

The Maxwell-Garnett theory can be extended to account for the finite size of the particles. This is essential in order to have better agreement of theoretical predictions with experimentally obtained results. Ruppin [28] has presented a comparative study of such extended Maxwell-Garnett theories. Among these, Doyle's approach [29], utilizing the Mie scattering technique, has been found to be the most successful. An effective permittvity

$$\epsilon_{\text{eff}} = \epsilon_h \frac{x^3 + 3ifa_1}{x^3 - 3ifa_1}, \tag{1.9}$$

is obtained, where a_1 describes the electric dipole within the framework of the Mie theory. Similarly, an effective magnetic permeability

$$\mu_{\text{eff}} = \mu_h \frac{x^3 + 3ifb_1}{x^3 - 3ifb_1}, \tag{1.10}$$

where b_1 is the magnetic dipole, should also be possible. This implies that an appropriate configuration of non-magnetic dielectric particles can possess a non-unit μ_{eff} if the magnetic Mie scattering contributes significantly. It is to be noted that the extended MG theories always yield a complex ϵ_{eff}, where the imaginary part represents radiation losses rather than absorption. However, Bohren [30] has pointed out that unlike the original MG theory, the extended theories do not always obey the scaling law, in the sense that $\epsilon_i \rightarrow \alpha\epsilon_i, \epsilon_h \rightarrow \alpha\epsilon_h$ does not necessarily lead to $\epsilon_{\text{eff}} \rightarrow \alpha\epsilon_{\text{eff}}$, except when $x \rightarrow 0$, warranting a certain degree of caution in their usage. All the extended versions of the MG theory tend to the correct limit as the size parameter $x \rightarrow 0$. Lamb *et. al.* [31] have shown that MG theories are appreciably affected for filling fractions larger than 0.3 - 0.5 in a periodic simple cubic structure or an aperiodic structure.

(ii) *Bruggeman theory*: The Bruggeman theory is conceptually somewhat different from the MG theory. A typical element of the two phase medium is assumed to be embedded in an effective medium whose properties are to be determined self-consistently. A self-consistent solution is obtained by solving for the local field around the element and demanding that the fluctuations of the local field around its effective value should average to zero. The following relation [32] defines the effective permittivity in this case:

$$f\frac{\epsilon_i - \epsilon_{\text{eff}}}{\epsilon_i + 2\epsilon_{\text{eff}}} + (1-f)\frac{\epsilon_h - \epsilon_{\text{eff}}}{\epsilon_h - \epsilon_{\text{eff}}} = 0 \tag{1.11}$$

Both these theories, in their original form, neglect the role of the distorted near field for the particles as well as their retarded induced polarization. These effects may become significant for higher filling fractions [32]. In essence, these theories are quasistatic theories whose applicability is limited to grain sizes $\ll \lambda$.

1.2.2 Homogenization theories

(i) *Homogenization by field averaging methods*: Here, we discuss a method which was used by Pendry *et. al.* [10, 33] in deriving the effective medium properties of periodic artificial magnetic structures. This technique is based on averaging the local fields according to

$$H^i_{\text{eff}} = \frac{1}{a}\int \mathbf{H}\cdot\mathbf{dx_i}, \quad E^i_{\text{eff}} = \frac{1}{a}\int \mathbf{E}\cdot\mathbf{dx_i}, \tag{1.12}$$

$$D^i_{\text{eff}} = \frac{1}{a^2}\int \mathbf{D}\cdot\mathbf{dS_i}, \quad B^i_{\text{eff}} = \frac{1}{a^2}\int \mathbf{B}\cdot\mathbf{dS_i}. \tag{1.13}$$

$\mathbf{E}_{\text{eff}}$ and $\mathbf{H}_{\text{eff}}$ are defined by averaging $\mathbf{E}$ and $\mathbf{H}$ along the sides of the unit cell, while $\mathbf{D}_{\text{eff}}$ and $\mathbf{B}_{\text{eff}}$ are defined by averaging $\mathbf{D}$ and $\mathbf{B}$ over the appropriate faces of the unit cell (Fig. 1.3). These quantities represent a set of averaged fields which may replace the local fields that vary throughout the unit cell. The unit cell should not intersect any of the structures contained within it, in order to preserve the continuity of the parallel components of $\mathbf{E}_{\text{eff}}$ and $\mathbf{H}_{\text{eff}}$.

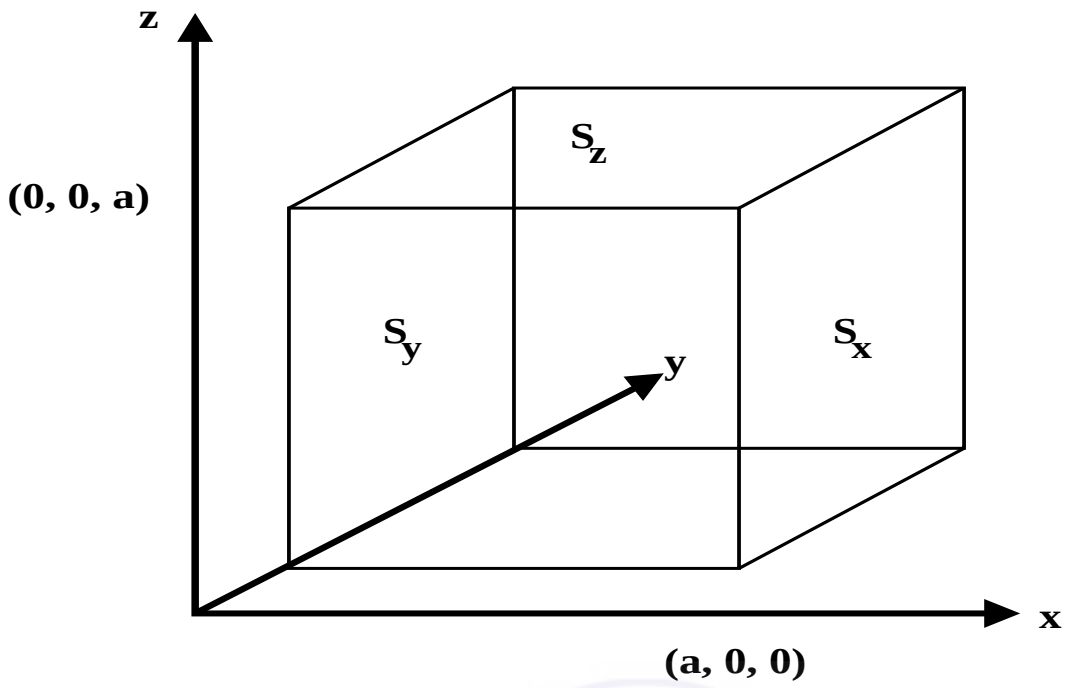

Figure 1.3: One of the procedures for averaging the local fields inside a metamaterial and determining ϵ_{eff} and μ_{eff} consists of averaging the **E** and the **H** fields over the edges of the cubic unit cell, along with averaging the **D** and the **B** fields over the appropriate faces of the unit cell.

Ideally a should be negligibly small with respect to the wavelength. However, even though this condition may not be satisfied exactly, the procedure can still be applied to obtain useful (and consistent) information about the properties of the (effective) medium on many occasions.

(ii) *Homogenization using the reflection and transmission coefficients*: In an experiment performed to investigate the effective-medium behaviour of a metamaterial, the quantities usually measured are the reflection coefficient R and the transmission coefficient T. Smith *et. al* [34] inverted the classical relations for R and T for a slab of isotropic and homogeneous material of thickness d to obtain

$$T = \left[\cos(nk_z d) - \frac{i}{2}(Z + \frac{1}{Z})\sin(nk_z d)\right]^{-1} e^{-ik_z d}, \tag{1.14}$$

$$R = \frac{-i}{2}(Z - \frac{1}{Z})\sin(nk_z d) T e^{-ik_z d}, \tag{1.15}$$

where Z and n are the effective impedance and the effective refractive index of the

medium, respectively. Further, inverting the above relations, they obtained:

$$n = \pm \arccos\left(\frac{1-r^2+t^2}{2t}\right), \tag{1.16}$$

$$Z = \pm \left[\frac{(1+r)^2-t^2}{(1-r)^2-t^2}\right]^{1/2}. \tag{1.17}$$

Here, $r = R$ and $t = T\exp(ik_z d)$. Finally, ϵ_{eff} and μ_{eff} can be obtained as:

$$\epsilon_{\text{eff}} = \frac{n}{Z}, \quad \mu_{\text{eff}} = nZ. \tag{1.18}$$

Since n and Z are complex functions with multiple branches, their values have an inherent ambiguity. This is resolved by determining them for several slab thicknesses and requiring a continuous function for $epsilon_{\text{eff}}$ and μ_{eff} with frequency. Any other ambiguity is usually resolved by demanding that $\text{Re}(Z) > 0$ and $\text{Im}(n) > 0$ for absorptive, causal media. However, there remains an ambiguity in the phase factor for reflected waves due to the choice of an appropriate reference plane. Another interesting feature that crops up is the appearance of $\text{Im}(\mu_{\text{eff}}) < 0$ with $\text{Re}(\epsilon_{\text{eff}}) < 0$ or $\text{Im}(\epsilon_{\text{eff}}) < 0$ with $\text{Re}(\mu_{\text{eff}}) < 0$ for negative permittivity and negative permeability metamaterials respectively. According to Soukoulis *et. al.*, this antiresonant behaviour [35] appears to be an intrinsic property of the retrieved parameters of a metamaterial, occuring because of finite spatial periodicity, which also sets a maximal wave number $k_{\text{max}} = \pi/a$ (assuming the periodicity to be a). This sets an upper bound on the value of n the effective medium can have. Although surprising, antiresonant behaviour does not violate any physical principle as long as the total energy dissipated inside the medium

$$W = \frac{1}{4\pi}\int d\omega\ \omega\left[\text{Im}[\epsilon_{\text{eff}}(\omega)]|E(\omega)|^2 + \text{Im}[\mu_{\text{eff}}(\omega)]|H|^2\right] > 0. \tag{1.19}$$

This condition does not require $\text{Im}[\epsilon_{\text{eff}}(\omega)]$ and $\text{Im}[\mu_{\text{eff}}(\omega)]$ to be simultaneously positive. However, it should be noted that many other factors such as anisotropy and bianisotropy are usually neglected in the above retrieval procedure and this affects the retrieved parameters.

Chen *et. al* [36] have suggested an improved method for determining the effective medium parameters using the S-parameters for a metamaterial slab. As the method proposed by Smith and others may not yield unambiguous results if the effective boundaries of the slab have not been determined correctly, they proposed the use of an optimization procedure for determining these. While the unit cell boundaries may be considered to be the effective slab boundaries for 1-D metamaterials, the optimization procedure yields better results for 2-D metamaterials or asymmetric unit cells. Further, they have also stated that in certain cases, it is not possible to use the criterion $\mathrm{Re}(Z) \geq 0$ directly. In such cases, the sign of Z has to be determined from the corresponding n by demanding that $\mathrm{Im}(n) \geq 0$ for a passive metamaterial.

However, it is to be noted that in the case of the homogenizable metamaterials studied in this thesis, the method of Smith *et. al.* was usually found to be adequate. The situations where effective medium parameters were not retrieved have more to do with the *breakdown* of the homogenization approach itself, rather than the inadequacy of the procedure adopted. In such cases, information regarding the response of the system was extracted from the band structures, the reflectivity-transmittivity spectra and/or the field maps of the electric/magnetic fields.

1.2.3 Limitations of the effective medium approach

The effective medium theories detailed above have their own limitations. They have to be applied carefully to the systems under consideration, keeping in mind the fact that a blind implementation of the procedures may not lead to consistent physical results. We list some of the major limitations of effective medium theories.

(i) Effective medium theories become invalid when the underlying metallic inclusions are not much smaller than the effective wavelength in the medium. Examples of such systems include metamaterials whose unit cells are significantly large at the frequencies of interest and photonic crystals. In some cases, the periodicity of the structure may also affect the retrieved values of μ_{eff} and ϵ_{eff}.

(ii) Further, homogenization cannot be carried out if the wave propagation inside the

medium cannot be described by a single propagating mode.
Failure to comply with these two conditions may result in the formation of unphysical numerical artifacts such as the antiresonant behaviour [35], which has been attributed to the periodicity of the underlying structure. Most metamaterials demonstrated have a structural size of $\sim \lambda/6$, although conservative estimates demand them to be much smaller.

For consistency, the retrieved parameters themselves may be verified by comparing results obtained using several retrieval methods. This is particularly true for the retrieval methods which use quantities like R and T and those utilizing the internal fields. In the former case, the retrieved parameters should be independent of the angle of incidence while in the latter case, they must be independent of the volume element considered. Even in the cases where the medium is not strictly homogenizable, a set of restricted equivalent medium parameters may be defined for specific angles of incidence. However, these quantities cannot be used for consistently calculating other properties of the medium such as the heating rate. The extended MG theories are examples of restricted effective medium theories [28]. Spatial dispersion may also occur in the long wavelength limit for wire array metamaterials for radiation incident obliquely. In such cases, it has been argued that the spatial dispersion should be incorporated into the effective medium model [37].

1.3 Negative Material Parameters

1.3.1 Negative Permittivity

At optical frequencies, many metals have a negative permittivity, as the conduction electrons can be assumed to be free against a background of static positive ions. This is responsible for the plasma-like behaviour of metals and the associated negative permittivity at frequencies below the plasma frequency. Upto the plasma frequency, the plasma prevents electromagnetic radiation from penetrating into the metal. The Drude

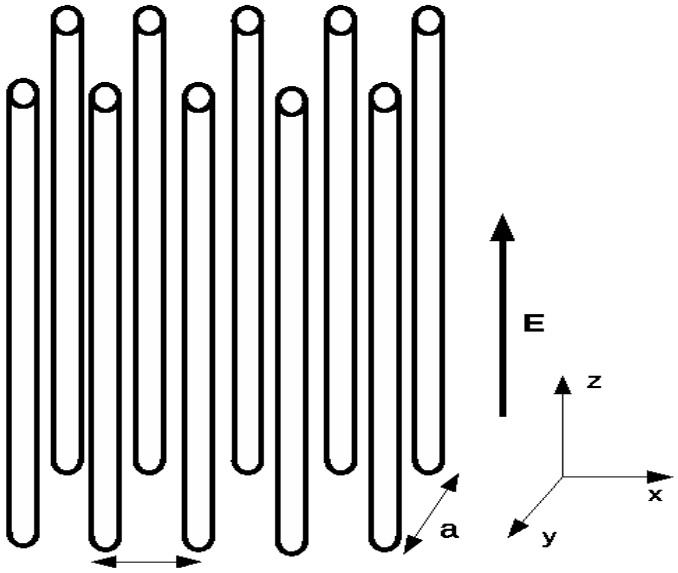

Figure 1.4: Schematic representation of the wire-array metamaterial which behaves like an effective plasma when the electric field of the incident radiation is aligned along the wire axes. The response is, however, anisotropic as the wires are along one direction only.

model for the dielectric permittivity of a metal yields a permittivity

$$\epsilon(\omega) = 1 - \frac{\omega_p^2}{\omega(\omega + i\gamma)} \tag{1.20}$$

which is negative below ω_p. Above ω_p, the metal behaves like an ordinary positive dielectric, ω_p is the bulk plasma frequency and corresponds to a bulk excitation of the free electron gas.

Metamaterials have been designed to generate both negative permittivity as well as negative permeability. They have even been designed to give chiral or bianisotropic material parameters. Here, the discussion has been limited only to metamaterials that have a negative permittivity or a negative permeability or both. Metallic wire-mesh structures have been proposed as negative dielectric media [38, 39]. These structures consist of an array of infinitely long, parallel and very thin metallic wires (radius r) on a square lattice of side a, aligned parallel to the electric field of the incident radiation (Fig. 1.4). Within the quasi-static picture, (wavelength $\lambda \gg r$), the radiation does not sense the individual wire structures but experiences on the whole a reduced

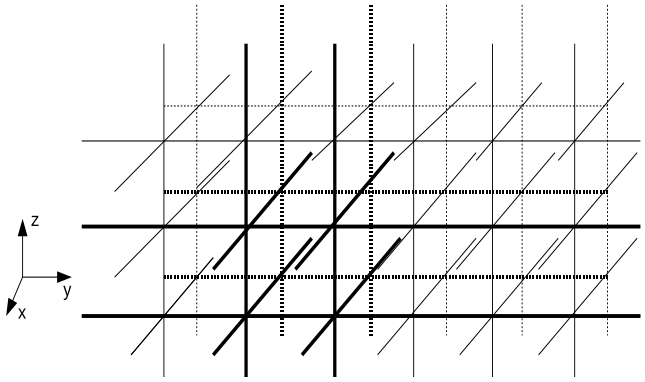

Figure 1.5: Schematic diagram of a wire array metamaterial consisiting of a three-dimensional lattice of connected wires which behaves like an effective, isotropic artificial plasma. In the case of a similar configuration of unconnected wire, spatial dispersion becomes an important issue.

average charge density. In addition, the large inductance of the thin wires for the currents induced makes it appear as though the electrons have acquired a large effective mass. These two effects result in an effective plasma-like response with a much lower plasma frequency. Neglecting the effect of the finite conductivity of the wires (and hence dissipative losses), one obtains [15]

$$\epsilon(\omega) = 1 - \frac{2\pi c^2}{\omega^2 a^2 \ln(a/r)} \tag{1.21}$$

where the plasma frequency $\omega_p^2 = 2\pi c^2/a^2 \ln(a/r)$. Assuming the wires to have a finite conductivity σ, the preceding expression gets modified to yield [15]

$$\epsilon(\omega) = 1 - \frac{\omega_p^2}{\omega^2 + i(\epsilon_0 a^2 \omega_p^2/\pi r^2 \sigma)\omega} \tag{1.22}$$

This medium is anisotropic with negative permittivity only for waves with the electric field aligned parallel to the wires. To achieve a reasonably isotropic response, meshes of wires oriented along all the three orthogonal directions are required (Fig. 1.5). Connec-

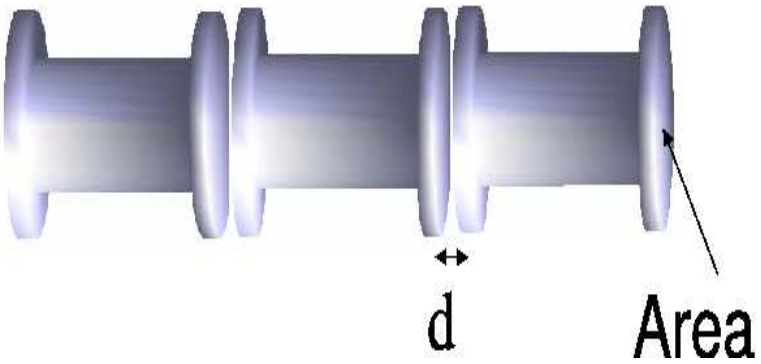

Figure 1.6: Schematic diagram of the cut-wire metamaterial whose response is akin to an array of periodically-placed electric dipoles.The metamaterial has an effective Lorentz permittivity with a negative permittivity band.

tivity of the wires in the three directions is required to form a truly three-dimensional low frequency plasma. The effects of the connectivity of the wires has also been investigated by several researchers, with the issues of strong spatial dispersion playing a more important role for meshes made of unconnected wires [39, 37]. However, the fabrication of three-dimensional connected wires is difficult and this poses a barrier for mass production. The polarization induced in the direction orthogonal to the wires is also small and can be neglected for very thin wires ($r \ll \lambda$). The waves, which sense only the wires parallel to the electric field, thus have a longitudinal mode. Schurig *et. al.* have proposed an inductive capacitive resonator with a strong electric response, as an alternative to wire media [40].

Instead of having extremely long ('infinite') wires, one can also have arrays of discontinuous conducting wire segments ('cut wires'), as shown in Fig. 1.6. The main difference between this configuration and the previous one is due to the capacitance between adjacent wire segments. Neglecting the thickness of the wires and their self capacitance, assuming that the length of each segment, $\ell \gg d$, the distance between adjacent segments, the following expression for the effective permittivity may be obtained [41]:

$$\epsilon(\omega) = 1 + \frac{\omega_p^2}{\omega_0^2 - \omega^2 - i\Gamma\omega}. \tag{1.23}$$

Here, ω_0, the resonance frequency and Γ, the dissipation factor, are given by

$$\omega_0 = \sqrt{\frac{2\pi c^2 d}{\epsilon_h A(\ell + d)\ln(a/r)}}, \tag{1.24}$$

$$\Gamma = \frac{a^2 \epsilon_0 \omega_p^2}{\pi r^2 \sigma}, \tag{1.25}$$

respectively. In the preceding expression, ϵ_h and A denote the permittivity of the medium in the capacitive gaps while A is the cross-sectional area of each cut face of the wire segment. Thus, the 'cut wire' metamaterial exhibits a Lorentz-type permittivity with a negative permittivity band over the frequency interval $\left[\omega_0, \sqrt{\omega_0^2 + \omega_p^2}\right]$. Since dipole moments can be formed across the gaps between the segments, the response of the medium is akin to an array of periodically placed dipoles.

1.3.2 Negative Permeability

The magnetic response of most natural materials begins to tail off at frequencies in the GHz range. Further, materials such as ferrites, which remain moderately active upto frequencies of about 100 GHz, are often heavy and do not have suitable mechanical properties. Thus, while it is extremely difficult to even obtain a magnetic response at microwave frequencies, obtaining a negative permeability is much more so. Landau and Lifshitz [42] have shown how the magnetic activity arising due to orbital currents at optical frequencies should be negligible. It is to be noted, however, that their treatment neglects the polarization currents in the system.

Metamaterials have come to play an important role in this context. Structured materials with considerable magnetic activity (both paramagnetic and diamagnetic) can be designed for operation at a desired frequency. Pendry *et. al.* [10] have shown that is possible to generate a resonant magnetic response and hence, a negative effective permeability μ_{eff}, by means of appropriately designed metamaterials. In the case of these structured media, the magnetic moments of the induced real and displacement current distributions contributes to an effective magnetization, if the electric polarizability of

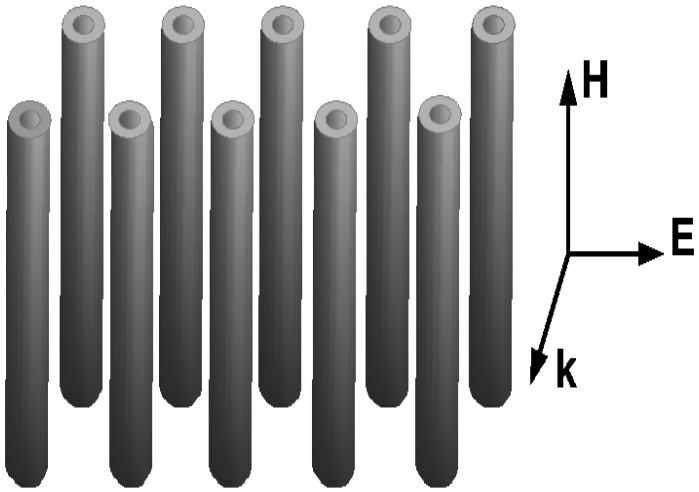

Figure 1.7: An array of metallic cylinders which effectively has a diamagnetic magnetic response, but cannot possess a negative permeability.

the medium is low.

An Array of Metal Cylinders: While most materials tend to be diamagnetic naturally as a consequence of Lenz's law, an array of metallic cylinders can be used to produce an effective diamagnetic response [10]. The model is shown in Fig. 1.7. The magnetic field along the cylinder axes induces circumferential surface currents which generate an opposing magnetization. Assuming a uniform depolarizing field and frequencies low enough so that the skin effect is small, the effective relative permeability of the medium is [10]

$$\mu_{\text{eff}}(\omega) = 1 - \frac{\pi r^2/a^2}{1 + i(2\rho/\mu_0 \omega r)}. \tag{1.26}$$

Here ρ is the resistance per unit length of the cylinder. Thus, the response of this medium is diamagnetic. But it is not sufficient to generate negative magnetic permeability. The limitations of this structure were overcome by including capacitive elements into this structure, as discussed below.

The Split Ring Resonator (SRR): Split Ring Resonators form the structural and functional unit of most of the metamaterials that exhibit negative permeability today.

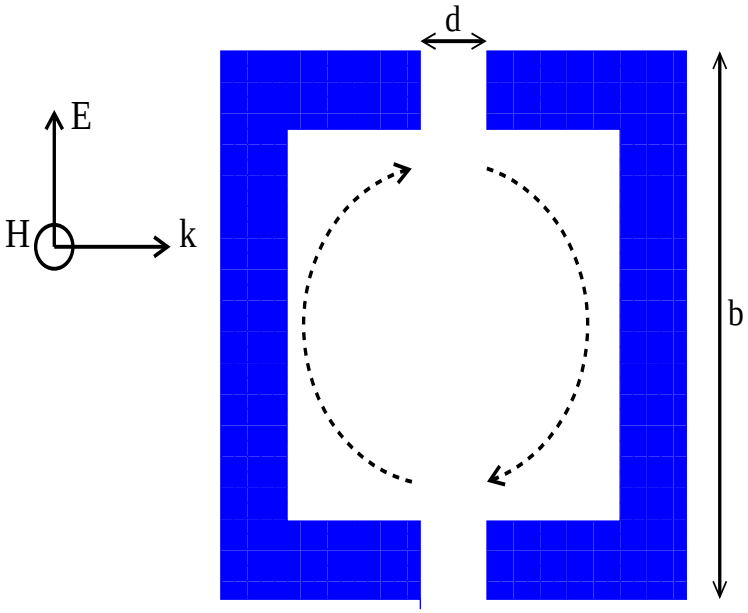

Figure 1.8: Schematic diagram of a typical SRR showing the direction of the currents induced by the magnetic field of the incident radiation. This magnetic field can drive a resonant LC circuit through the inductance, resulting in a dispersive effective permeabilty.

Pendry's original proposal [10] defined them to be concentric metallic cylindrical shells with a (capacitive) gap in between them. Fig. 1.8 shows a typical SRR. The working principle of the SRR is quite simple. The magnetic field of the incident electromagnetic radiation can drive a resonant LC circuit through the inductance, leading to a dispersive effective permeability. L and C represent the inductance and the capacitance, respectively, of the equivalent circuit formed by the SRR. A metamaterial consisting of an array of SRR exhibits an effective negative permeability (μ_{eff}) given by [10]:

$$\mu_{\text{eff}}(\omega) = 1 + \frac{f\omega^2}{\omega_m^2 - \omega^2 - i\Gamma\omega}. \tag{1.27}$$

Here f is the filling fraction of the metal, ω_m is the magnetic resonance frequency defined as $\omega_m = 1/\sqrt{LC}$and Γ is the dissipation in the metamaterial, which is primarily dictated by the levels of dissipation in the metal of which the SRR is made. The actual values of ω_m and Γ depend on the details of the geometry.

The SRR has a negative permeability band above the resonance frequency ω_m. Above this frequency, the response of the SRR is out of phase with the driving field and $\mu_{\text{eff}} < 0$

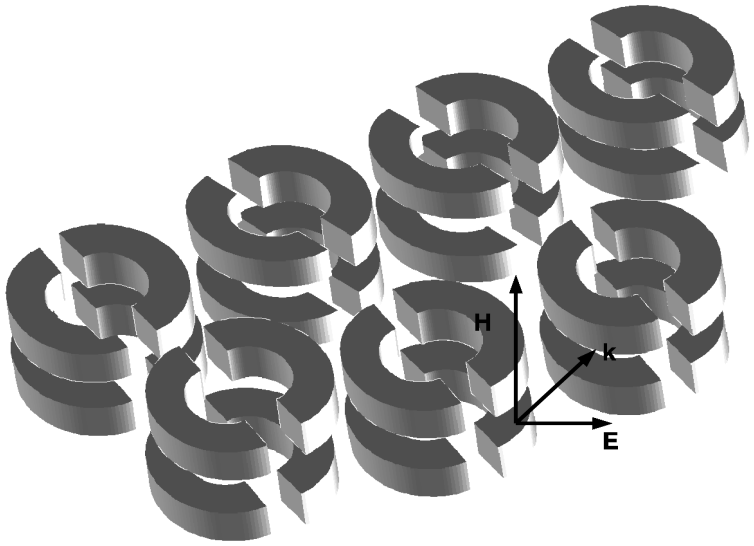

Figure 1.9: A pictorial depiction of a SRR-based metamaterial showing the arrangement of the SRR, periodically in the horizontal plane and stacked up in the vertical direction. The medium displays uniaxial magnetic activity and a negative magnetic permeability when the magnetic field is oriented along the (common) cylindrical axis of the SRRs.

up to a magnetic plasma frequency ω_{mp}. This leads to a gap in the dispersion relation for $\omega_m < \omega < \omega_{mp}$. The appearance of the bulk longitudinal magnetic plasma mode at ω_{mp} (due to the induced currents), mimics the presence of free magnetic poles. The nature of the resonance depends upon the metal used for fabricating the SRR. The resistivity of the metal, in general, broadens the resonance, while for extremely resisitive materials, the resonance may be so highly damped that the region of negative μ_{eff} can disappear altogether. The SRR-based metamaterials (as shown schematically in Fig. 1.9) produce a uniaxial magnetic response when the magnetic field of the radiation is oriented along the axis of the SRR. Thus, the magnetic response in the other directions is nearly zero. This highly anisotropic response was sought to be rectified by interleaved orthogonal planes of planar SRRs [10]. Balmaz and Martin [43] proposed a novel configuration consisting of two orthogonal intersecting SRR. This has a reasonably isotropic response for any wave incident on it normal to the plane of the rings.

1.3.3 SRRs and scaling

The SRR forms an almost model system for studying the origin and the nature of the magnetic response of metamaterials. Circuit models in the quasi-static limit have been developed to explain the resonant magnetic nature of their response to incident radiation and their behaviour at microwave frequencies is in remarkable agreement with these theoretical models. As described earlier, their resonant behaviour can be ascribed to an internal inductance (L) and capacitance (C) within each element and they exhibit a resonant magnetic permeability of the form of Eq. 1.27. As mentioned earlier, the width of the resonance and the modulation extent of the negative μ band are primarily determined by the intrinsic levels of dissipation in metal.

SRRs can be suitably designed for operating at any desired frequency. Maxwell's equations appear to suggest that one can increase the operating frequencies by merely scaling down the size of the structures. As an example, one can consider the case where the structural dimensions are halved as the unit cell becomes smaller. If the SRR is considered to be a series LC circuit, the resonance frequency is expected to double every time. However, this does not happen at high frequencies and in fact, the resonance frequency begins to saturate as the structural dimensions are reduced [44].

1.3.4 Scaling to high frequencies

The behaviour of SRR-based magnetic metamaterials at high frequencies shows significant deviations from their behaviour at lower frequencies. The simplistic idea of reducing the length-scales involved for obtaining a magnetic resonance at high frequencies does not work. The main problem is due to the fact that at high frequencies, metals no longer behave as perfect conductors and electromagnetic fields begin to penetrate into the metal. At these frequencies, the dispersive nature of the metal itself needs to be taken into account. The deviations from the ideal behaviour may be explained by means of a simple model [15, 44] considering the circular metallic resonator shown in Fig. 1.10.

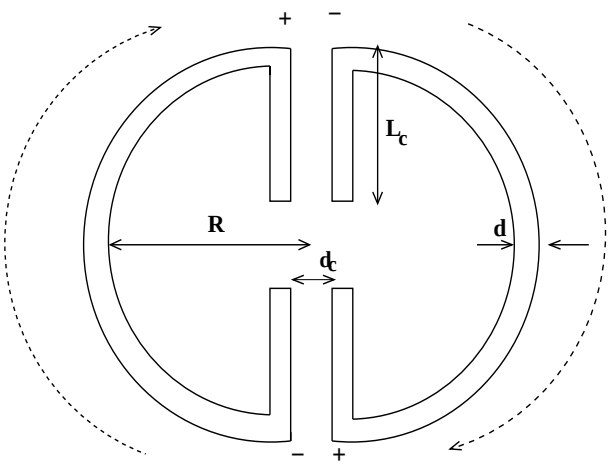

Figure 1.10: The equivalent ring model for the SRR used to study its magnetic response at high frequencies. This model is used to get an insight into the lack of high frequency scaling in SRRs.

A time-varying magnetic field H_{ext} along the cylindrical axis of the structure and a strong skin effect are assumed. The displacement current is then estimated to be

$$j_\phi = -i\omega\epsilon_0\epsilon_m E_\phi. \tag{1.28}$$

This creates a potential drop

$$V_r = \int_0^\pi E_\phi r d\phi \tag{1.29}$$

The potential drop across each capacitive gap is

$$\begin{aligned} V_C &= \frac{1}{C}\int I(t)dt \\ &= \frac{j_\phi \tau_c d_c}{-i\omega\epsilon_0\epsilon L_c}. \end{aligned} \tag{1.30}$$

The total emf induced around the loop is given by

$$2V_r + 2V_c = i\omega\mu_0\pi r^2 H_{\text{int}}. \tag{1.31}$$

Subsequently, the magnetic fields inside and outside the split cylinders can be related

to each other as:

$$\frac{H_{\text{ext}}}{H_{\text{int}}} = 1 - \frac{\mu_0 \epsilon_0 \omega^2 \pi r^2 \tau_c}{(2\pi r/\epsilon_m + 2\tau_c d_c/\epsilon L_c)} \tag{1.32}$$

Next, considering the averaged magnetic induction

$$B_{\text{eff}} = \mu_0 H_{\text{int}} + (1-f)\mu_0 H_{\text{ext}} \tag{1.33}$$

and the effective magnetic field

$$H_{\text{eff}} = H_{\text{ext}}, \tag{1.34}$$

the following expression for the effective permeability is obtained:

$$\begin{aligned} \mu_{\text{eff}} &= \frac{B_{\text{eff}}}{\mu_0 H_{\text{eff}}} \\ &= 1 + \frac{f\mu_0 \epsilon_0 \omega^2 \pi r^2}{[(2\pi r/\epsilon_m \tau_c) + 2d_c/\epsilon L_c] - \epsilon_0 \mu_0 \omega^2 \pi r^2 \tau_c} \end{aligned} \tag{1.35}$$

Most metals have a plasma-like dispersion at high frequencies. One can safely approximate the dielectric permittivity of the metal by

$$\epsilon_m(\omega) \simeq -\frac{\omega_p^2}{\omega(\omega + i\gamma)}. \tag{1.36}$$

when the frequency is small compared to ω_p and the magnitude of the background permittivity is small in comparison. Defining two new quantities, viz., the inertial and the geometric inductance given by the expressions

$$L_i = \frac{2\pi r}{\epsilon_0 \tau_c \omega_p^2}, \tag{1.37}$$

$$L_g = \mu_0 \pi r^2, \tag{1.38}$$

the effective permeability can be written as [44]

$$\mu_{\text{eff}} = 1 - \frac{f'\omega^2}{\omega^2 - \omega_0^2 + i\Gamma'\omega}. \tag{1.39}$$

Here, f', ω_0 and Γ' are the quantities:

$$\omega_0 = \frac{1}{\sqrt{(L_i + L_g)C}} \tag{1.40}$$

$$\Gamma' = \frac{L_i}{L_i + L_g}\gamma \tag{1.41}$$

$$f' = \frac{L_g}{L_i + L_g}f. \tag{1.42}$$

The inertial inductance arises solely due to the electronic mass since $\omega_p^2 = Ne^2/m\epsilon_0$, where N and m are the electron density and the electron mass, respectively. In addition, the effective damping factor also increases and resistive losses become more effective, resulting in the broadening of the response. Thus, even if the size of the SRR unit is reduced, the inertial inductance would still be present, preventing scaling of the operating frequencies beyond a certain limit, while the accompanying increase in damping may cause the region of negative permeability to vanish altogether. However, it is still possible to salvage the situation to some extent by adding more capacitive gaps to the SRR. It is to be noted that although the ring model accounts for the lack of scaling in SRR, it does not take into consideration the stray capacitance in the system which causes the resonance frequency to be lower than than the value predicted by circuit theory. Further, there is always the chance that unless designed carefully, the size of the unit cell may become comparable to the free space wavelength at resonance, resulting in the breakdown of effective medium theories.

Bianisotropy in SRR media

A bianisotropic medium is one characterised by constitutive relations of the form

$$\mathbf{D}(\mathbf{x}, \omega) = \tilde{\epsilon} \cdot \mathbf{E}(\mathbf{x}, \omega) + \tilde{\alpha} \cdot \mathbf{B}(\mathbf{x}, \omega), \tag{1.43}$$

$$\mathbf{H}(\mathbf{x}, \omega) = \tilde{\beta} \cdot \mathbf{E}(\mathbf{x}, \omega) + \tilde{\mu^{-1}} \cdot \mathbf{B}(\mathbf{x}, \omega). \tag{1.44}$$

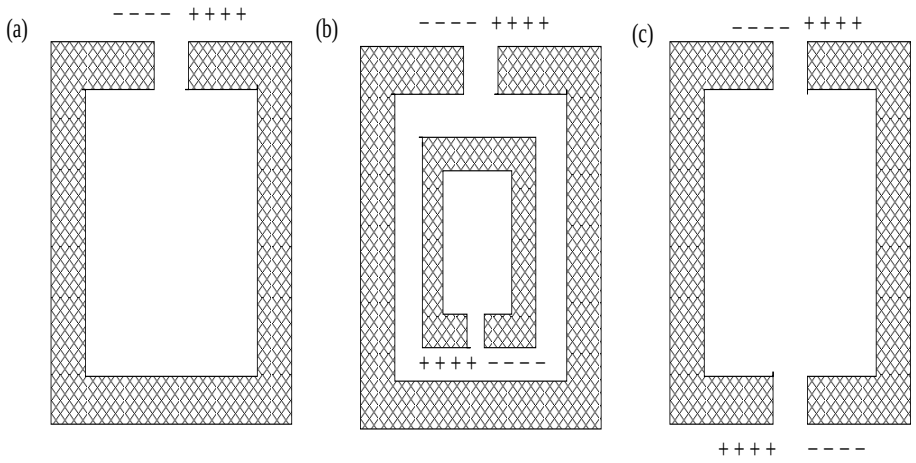

Figure 1.11: (a) and (b): Bianisotropic SRRs of square cross-section showing the possibility of the development of a net electric dipole moment even when the systems are driven by a magnetic field. The symmetric SRR in (c) is not bianisotropic due to the cancellation of the dipoles arising due to the charge distribution.

Here, $\tilde{\epsilon}$ is the permittivity dyadic, $\tilde{\mu}$ is the permeability dyadic, while $\tilde{\alpha}$ and $\tilde{\beta}$ are the magnetoelectric dyadics. A bianisotropic medium provides cross-coupling between electric and magnetic fields. When placed in an electric or a magnetic field, a bianisotropic medium becomes both polarized *and* magnetized simultaneously.

A split-ring resonator with a single split is bianisotropic as a large electric dipole moment is generated across the capacitive gap. This could very well overshadow the weaker magnetic response of the SRR. As a result, a low electrical polarizability of the ring is preferred. Symmetric SRRs with two splits are not bianisotropic as the dipole moments across opposite ends cancel each other leaving behind only a weaker electric quadrupole moment (See Fig. 1.11). The original SRR proposed by Pendry [10], is also bianisotropic as it develops an electric polarization (which can also be driven by the electric field) in between the two split rings.

The electric dipole moments formed in the single split rings can be nullified by rotating adjacent SRRs in the arrays by 180 degrees. However, this results in doubling the unit cell size. Thus, bianisotropy in SRRs can be minimized by either a single symmetric SRR or by arranging SRRs symmetrically within the array so that the net dipole moment cancels out. At high frequencies, when the SRR unit cell size becomes comparable to the wavelength, some of the responses of symmetric SRRs appear similar

to bianisotropic behaviour. This is, however, an artefact of the inaccurate description by effective medium theories and is discussed further in Chap. 2.

However, it has been shown in Chap. 2 that the breakdown of effective medium theories at high frequencies leads to the development of an apparent bianisotropic behaviour, even in symmetric SRR systems. This behaviour has been subsequently analysed in detail.

Arrays of dielectric cylinders Arrays of dielectric cylinders have also been proposed as an alternative means of generating a negative permeability [45]. This response arises due to the single-scatterer resonances (Mie resonances) of the system. These resonances are the electromagnetic analogue of the resonant scattering from a potential well, with the scatterers (cylinders) with a larger permittivity than the surrounding medium playing the role of an attractive potential for photons. To be specific, in this case, the zeroth-order TE Mie resonance gives rise to the magnetic activity of the system. The resonant size parameters of the system can be determined using the poles of the coefficients of the internal fields. It has been found that in the case of the zeroth-order Mie resonance, the azimuthally-directed polarization currents are enhanced. This results in the enhancement of the magnetic field along the cylinder axis. Thus, for an array of identical cylinders, these localized magnetic modes are capable of giving rise to a macroscopic magnetization, and hence, a non-zero magnetic susceptibility of the system. The resultant effective permeability of the array is strongly dispersive in the vicinity of the Mie resonance and also attains negative values. The effective permeability of the metamaterial has been found to be given by the expression [45]

$$\mu_{\text{eff}}(\omega) = \frac{2\pi}{d^2}\frac{c\int_0^a J_0(nkr)r\ dr + \int_a^{d/\sqrt{\pi}}\left[J_0(kr) - a_0 H_0^{(1)}(kr)\right] r\ dr}{J_0(kd/2) - a_0 H_0^{(1)}(kd/2)}, \tag{1.45}$$

where d defines the size of the unit cell, c is the speed of light and a is the radius of each cylinder. The integration is performed over a circular area such that $d^2 = \pi r^2$, considering the contribution of only the resonant zeroth-order Mie mode. Similar ideas have been applied to high permittivity dielectric spheres to produce 3-D metamaterials [46].

1.4 Surface Plasmons

The negative material parameters of metamaterials enables them to support resonant electromagnetic surface states. In this section, we present a brief discussion on the nature of these surface modes.

A negative dielectric permittivity enables a metal-vacuum interface to support resonances called surface plasmons on the surface of the metal [47, 48, 49]. These are collective excitations of the electrons with the charges displaced parallel to the interface, and the wave decaying exponentially into the medium on either side. The surface plasmons are thus localized on the surface of the metal (Fig. 1.12). At very short wavelengths, the fields are essentially electrostatic in nature. The condition for their existence at a vacuum/metal interface is

$$\epsilon(\omega) + 1 = 0. \tag{1.46}$$

Neglecting losses, $\omega_{sp} = \omega_p/\sqrt{2}$, where ω_{sp} is the surface plasma frequency. Thus, surface plasmons are degenerate at $\omega = \omega_{sp}$ for large wave-vectors. The dispersion relation for surface plasmons at the interface of a positive and a negative dielectric is :

$$k_x = \frac{\omega}{c}\left[\frac{\epsilon_+\epsilon_-}{\epsilon_+ + \epsilon_-}\right]^{1/2}, \tag{1.47}$$

where k_x is the parallel wave vector, and ϵ_+ and ϵ_- are the permittivities of the positive and the negative dielectric respectively. Thus, for a metal-vacuum interface, $k_x > \omega/c$, making it impossible to excite surface plasmons on a perfectly flat surface using propagating electromagnetic modes.

In a manner analogous to the above, surface plasmons of a magnetic nature (s-polarized waves) may exist at the interface between a medium with positive permeability and one with negative permeability [50, 51].

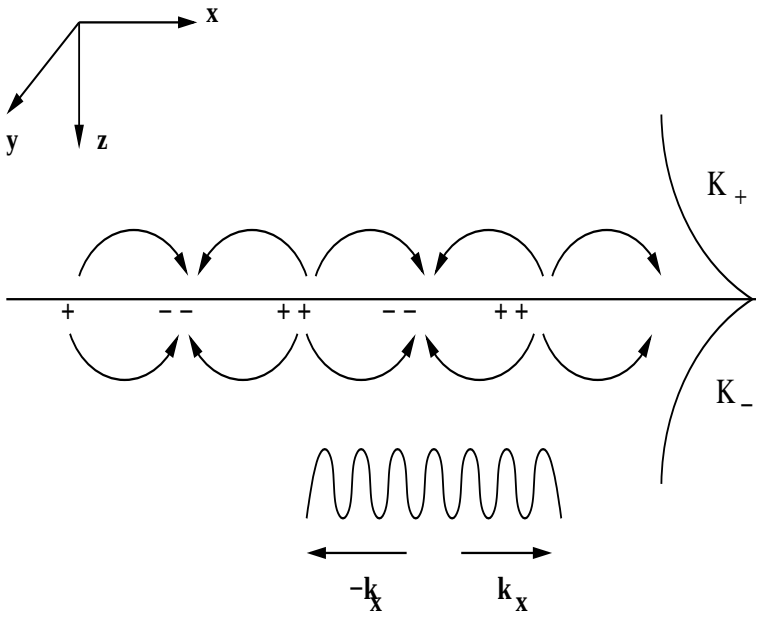

Figure 1.12: A surface plasmon at the interface between positive and negative dielectric media, showing the exponential decay of the fields perpendicular to the interface between the two media. The surface plasmon mode itself propagates along the interface.

1.4.1 The role of surface plasmons in the perfect lens

Surface plasmon modes play a crucial role in the subwavelength focussing action of a perfect lens. As already mentioned, the amplification of evanescent waves occurs by means of these modes. The conditions satisfied in the perfect lens, viz., $\epsilon_+ = \epsilon_-, \mu_+ = -\mu_-$, are ideal for the excitation of surface plasmons of electric or magnetic nature, for the incident p-polarized or s-polarized waves, respectively. When these conditions are satisfied simultaneously at a single frequency ω, we have:

$$\frac{(k_x^2 - \epsilon_+\mu_+k_0^2)^{1/2}}{\epsilon_+} + \frac{(k_x^2 - \epsilon_-\mu_-k_0^2)^{1/2}}{\epsilon_-} = 0, \tag{1.48}$$

$$\frac{(k_x^2 - \epsilon_+\mu_+k_0^2)^{1/2}}{\mu_+} + \frac{(k_x^2 - \epsilon_-\mu_-k_0^2)^{1/2}}{\mu_-} = 0, \tag{1.49}$$

where $k_0 = \omega/c$.

These relations are satisfied for all k_x and thus, the plasmon modes (of both kinds) become degenerate. The presence of the second interface detunes the plasmons on each interface so that that the fields of the surface plasmon exactly cancel the incident field just after the first boundary of the slab, while the fields of the two surface plasmons

again cancel exactly just before the slab (for zero reflectivity). This coherent action of the surface plasmon fields results in the perfect lens action (see [15] and references therein).

1.4.2 Plasmon resonances in small particles

Plasmonic resonances in small particles are examples of highly localized surface plasmons, which give rise to interesting absorption spectra very different from the behaviour of the bulk material. In the case of metallic particles, the deviations from the behaviour of the bulk metal are even more distinct. The intense shape-dependent absorption spectra can be described adequately using classical electromagnetic theory [52]. Mie theory predicts the existence of certain complex frequencies at which the scattering coefficient diverges [53]. The modes associated with these frequencies are thus virtual. Nevertheless, at real frequencies close to these complex frequencies, the scattering coefficients are large. The modes associated with these frequencies are the surface modes and they occur at specific frequencies for particles of specific shapes. The lowest frequency mode is known as the Fröhlich mode. For example, in the case of spherical particles, a surface mode exists when the condition [53, 52]

$$\epsilon_m + 2\epsilon_b = 0, \tag{1.50}$$

where $\epsilon_m = \epsilon'_m + i\epsilon''_m$ is the permittivity of the metal (adequately described by the Drude theory) and ϵ_b is the permittivity of the background medium. Thus, the condition for the existence of the surface mode is

$$\mathrm{Re}[\epsilon_m] + 2\epsilon_b = 0, \quad \mathrm{Im}[\epsilon_m] \simeq 0. \tag{1.51}$$

Similarly, for cylindrical particles, a surface mode exists when [53, 52]

$$\epsilon_m + \epsilon_b = 0. \tag{1.52}$$

These conditions can also be obtained in a simpler manner using electrostatics [52].

1.5 Coherent optical effects in atomic and molecular media

One of the primary aims of this thesis is to propose controlling the metamaterial response at optical and NIR frequencies by embedding them in resonant dielectric media. Thus, one uses effects like coherent control, Electromagnetically Induced Transparency and Raman processes, which are explained purely from the standpoint of quantum mechanics, to actively control the resonant behaviour of metamaterials, which are geometric in origin and can be treated classically within the framework of Maxwell's equations. Some of these phenomena, which have been used in subsequent chapters, have been described in this section.

1.5.1 Coherent control

Quantum mechanical transitions naturally permit a picture akin to wave phenomena which can be subject to constructive and destructive interferences. This is a consequence of the fundamental principle of superposition of quantum states. Thus, in principle, quantum phenomena of any kind are amenable to control by coherent optical radiation. The theoretical possibilities that have been presented for coherent control are quite spectacular. In fact, calculations have suggested and experiments have demonstrated that appropriate laser pulses or pulse sequences can be used to break strong bonds, force molecules to climb anharmonic ladders, change reaction pathways, transform local modes into energy eigenstates, etc [54]. A variety of control schemes with multiple lasers have been suggested. These involve the manipulation of competing interfering pathways to a final state resulting in either a constructive or destructive interference leading to the enhancement or the suppresion of the transition [55]. Typically, the two pathways may differ by accessing different intermediate states, requiring the use of several control fields

coherently phase-locked together. For simple systems with a relatively lesser number of isolated intermediate and final states, this scheme is an attractive one for practical implementation. However, the situation is greatly complicated in the case of polyatomic molecules which can have a great many potentially different interfering pathways.

The essential process for achieving control within the framework of quantum mechanics consists of the active manipulation of the probability amplitudes of the transition pathways resulting in constructive or destructive interference. The final state itself may be a coherent superposition of several eigenstates. It should be noted that successful control over these processes will be determined by the delicate destructive and constructive interference of the multiple pathways. In order to observe these interferences, the pathways must have a definite phase relationship, i.e., they must be driven to coherence. However, the presence of collisions and other mechanisms tend to destroy the coherence. Historically, the first proposed scheme for coherent control was based on the interference between several excitation paths leading to the same final state [56, 57]. One path is excited by a multiphoton transition, while the other is excited by a one-photon transition, with the latter photons being harmonically generated from the first ones. This ensures that the final state reached by both the paths have the same energy. In addition, the coherence relationship between the electric fields is well-defined [58]. Coherent control may be used to produce remarkable changes in the optical properties of atomic/molecular media. Among other effects, it has led to the demonstration of the phenomena of Electromagnetically Induced Transparency (EIT) [59, 60], superluminal [61] and subluminal [62] propagation of light, stopped light [63, 64], enhanced index of refraction [65, 66], etc.

1.5.2 Electromagnetically Induced Transparency

The linear response of an atom to light at a resonant frequency is described by the first order susceptibility $\chi^{(1)}$. The imaginary part of this quantity defines the absorption in the medium while the real part determines the refractive index. The optical response of an atomic/molecular medium can be modified by the laser-induced coherence of the

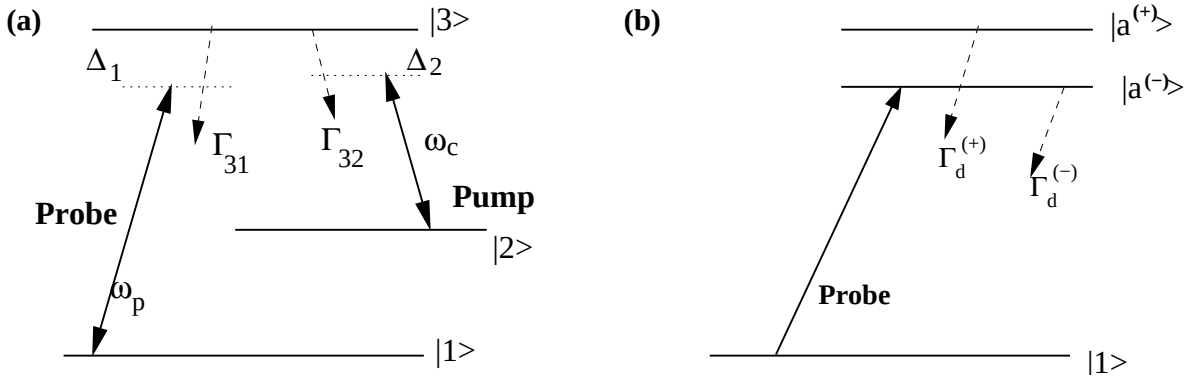

Figure 1.13: The level scheme for observing EIT in a three-level Λ system. Fig. (a) shows the Λ scheme for EIT in a three-level system when a strong control field is applied. Fig. (b) is the dressed state picture for the same scheme.

atomic states which leads to a quantum interference of excitation pathways that control the optical response. Electromagnetically Induced Transparency uses this scheme to eliminate the absorption and the refraction of light at a resonant frequency of a transition. Electromagnetically Induced (EIT) was proposed by Harris in 1989 [59]. The essence of this phenomenon lies in the effect known as Coherent Population Trapping (CPT), which was discovered by Alzetta *et. al.* [67] in 1976. The first experimental demonstration of EIT was carried out by Boller *et. al.* [60] using optically opaque strontium vapour with an atomic density of $\sim 5 \times 10^{15}\text{cm}^{-3}$. Fig. 1.13 and Fig. 1.14 illustrate the possible schemes for EIT to occur in an optically thick medium. Of these, the first (the Λ configuration) is the most useful involving two ground states coupled to an excited state, while the other two are of limited utility, due to the absence of a metastable state [68].

The Λ configuration offers a pedagogic model for explaining the occurrence of EIT. Let us consider the Λ scheme in some detail. The $|1\rangle \rightarrow |2\rangle$ transition is assumed to be dipole forbidden. The idea of laser-dressed eigenstates of the three-level atom provides a means of illustrating the connection between EIT and maximal coherence. Within the dipole approximation, the atom-laser interaction is expressed in terms of the Rabi frequency [69]

$$\Omega_c = \frac{\vec{\mu} \cdot \mathbf{E_c}}{\hbar}, \tag{1.53}$$

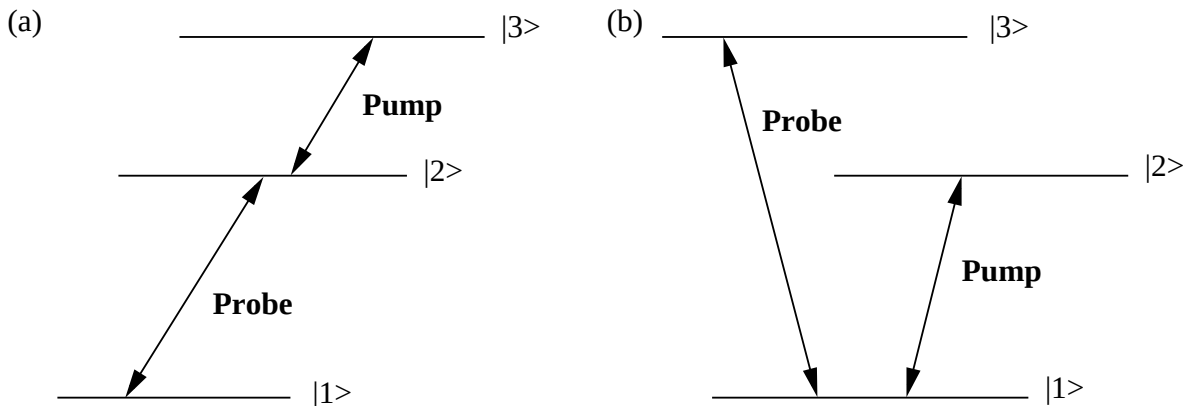

Figure 1.14: The ladder and the vee level schemes for EIT in three-level systems. These are hindered by the lack of a metastable state.

where $\mathbf{E_c}$ is the coupling electric field having a frequency ω_c and $\vec{\mu}$ is the transition electric dipole moment across the $|1\rangle \rightarrow |2\rangle$ transition. The eigenstates of the total Hamiltonian which includes this interaction are the dressed states [68]. One of these states has the form $|\psi^0\rangle = \alpha|1\rangle - \beta|2\rangle$, the *dark state*, which contains no amplitude of the state $|3\rangle$ and is effectively decoupled from the light fields. The occurrence of EIT can be explained as the result of the system moving into the dark state $|\psi^0\rangle$ under the action of two laser fields satisfying the two-photon resonance condition and assisted by the incoherent decays from the excited state. As the population is trapped in the ground states $|1\rangle$ and $|2\rangle$, no absorption takes place. Thus, the population in the state $|3\rangle$ is zero and there is no spontaneous emission or light scattering. For a weak probe, the dark state $|\psi^0\rangle$ tends towards the state $|1\rangle$ which is immune to any further probe absorption. An alternative way to view this is as follows. The atomic system has two ways of reaching the dissipative state $|3\rangle$. It can do so directly by the $|1\rangle \rightarrow |3\rangle$ transition or via the path $|1\rangle \rightarrow |3\rangle \rightarrow |2\rangle \rightarrow |3\rangle$. Since Ω_c is strong, the two paths are comparable in amplitude and thus, they can exhibit strong quantum interference.

In actual atomic systems, the dephasing rate of the forbidden transition is non-zero due to atomic collisions. All the important features of EIT remain observable inspite of this as long as the control Rabi frequency is sufficiently large [68]. EIT effects can be observed in dense atomic gases or even solids [70, 71], as long as their exists a metastable transition with a dephasing rate much longer than that of the levels between

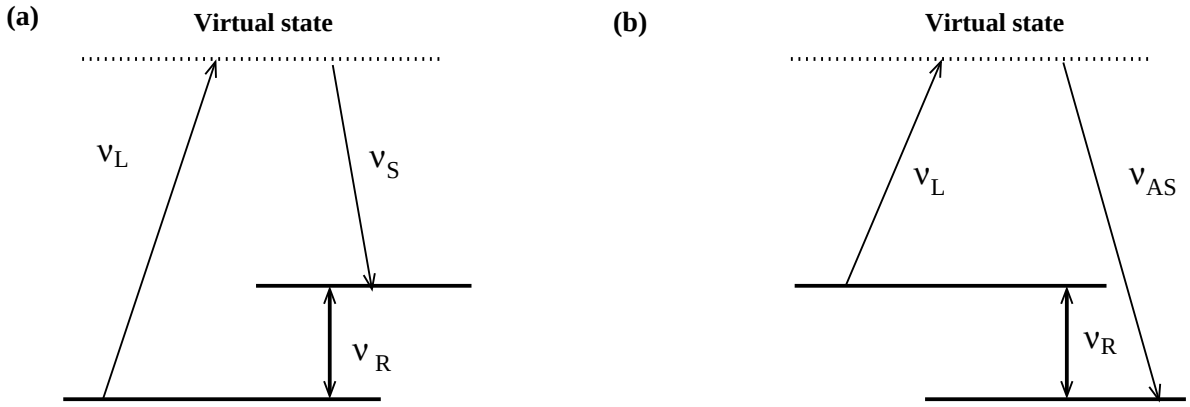

Figure 1.15: The level scheme for Raman Effect showing the emission of Stokes radiation at ν_S or anti-Stokes radiation at $\nu_{\rm AS}$ with the absorption of radiation at ν_L.

which transparency is to be induced.

1.5.3 Raman Scattering

Raman scattering or the Raman effect is the inelastic scattering of photons discovered by Sir C. V. Raman in liquids. When light is scattered from an atom or molecule, most photons are elastically scattered (Rayleigh scattering [53]), such that the scattered photons have the same energy (frequency) and wavelength as the incident photons. However, a small fraction of the light is scattered such that the scattered photons having a frequency different from, and usually lower than, the frequency of the incident photons. The frequency shifts arise due to the characteristic frequencies of the target molecules. Raman spectroscopy is used mostly as a tool for studying the vibrational energy levels of molecules and of lattice optical branch vibrations in crystals. In this method, a cell containing the sample is irradiated with a narrow band optical wave. Spectral analysis of the scattered radiation reveals the presence of frequencies that are lower by amounts equal to the vibrational frequencies of the medium. This occurs by means of a process known as Stokes scattering. Frequencies greater than the incident frequency by amounts equal to the vibrational frequencies are also generated although their intensities are much lower due to the requirement that the molecule must initially be in the excited state. The probability for a molecule to initially be in the excited state is exponentially smaller for a medium in thermal equilibrium. This process is

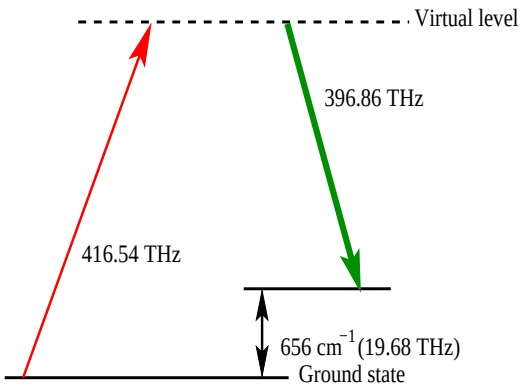

Figure 1.16: The proposed level scheme for Inverse Raman Effect using two molecular levels in CS_2. A strong pump field applied at a frequency ν_0 enables the resonant absorption of the probe field at an anti-Stokes frequency $\nu_0 + \nu_R$.

known as anti-Stokes scattering. These processes have been schematically represented in Fig. 1.15.

Stimulated Raman scattering is a process in which laser radiation at a frequency $\omega_{\rm L}$ leads to the absorption of a photon. Both Stokes and anti-Stokes absorption is possible. This results in a non-linear susceptibility ($\chi_{\rm NL}$) which is Lorentzian in nature. Consequently, the medium has a Lorentz permittivity

$$\chi_{\rm NL}(\omega) = \frac{\epsilon_0 N \left(\frac{\partial\alpha}{\partial X}\right)_0^2 |E|^2}{8m\left(\omega_0^2 - \omega^2 - i\gamma\omega\right)}, \tag{1.54}$$

where X is the normal vibrational co-ordinate, $\left(\frac{\partial\alpha}{\partial X}\right)_0$ is the differential polarizability of the molecule, E is the amplitude of the driving (laser) field while N and m are the number density and the mass of the species involved in the vibro-rotational dynamics of the molecule, respectively.

1.5.4 The Inverse Raman Effect

Studies of the normal and stimulated Raman scattering involve irradiating the scattering medium with monochromatic light of frequency ν_0 and energy density ρ_0. This light is absorbed and simultaneously light is also emitted (either spontaneously or by stimulation), at either the Stokes frequency $(\nu_0 - \nu_R)$ or the anti-Stokes frequency

($\nu_0 + \nu_R$) [72, 73], together with a change in the energy states of the atoms or the molecules. Here, ν_R is the molecular level spacing of the medium. Jones and Stoicheff, [72], irradiated the scattering medium simultaneously with intense monochromatic light of frequency ν_0 and an intense continuum. They observed sharp and strong absorption lines at a frequency $\nu_0 + \nu_R$ (anti-Stokes) in the spectrum of the continuum after it traversed the medium. This absorption, arising from stimulated Raman scattering, has been called the 'Inverse Raman Effect' (Fig. 1.16). It is thus essentially a competing process in which light at the anti-Stokes wavelength is attenuated in the presence of an intense pump, as opposed to the Stokes gain in Raman amplification. The Inverse Raman Effect and stimulated Raman scattering are corollary processes, with similar spectral characteristics. The semiclassical theory of radiation can be used to describe stimulated Raman scattering and the associated Inverse Raman effect by using second-order perturbation methods [73].

A part of this thesis has been devoted to the study of the electromagnetic response of composite metamaterials. The composite metamaterials investigate combine the attributes of EIT and metamaterials, raising the possibility of dynamic control over their behaviour. One simple design involves immersing the metamaterial in a dilute atomic gas whose frequency-selective absorption can be exploited to manipulate the metamaterial response. Furthermore, a combination of light fields accords extra control over the metamaterial via the absorption and dispersion of the atomic gas through the atomic coherence (quantum) route, based on effects like EIT. However, working at near-resonant conditions necessarily involves a large dispersion with frequency accompanied by high levels of dissipation. In this context, it has been shown that EIT-based control, which exploits the large frequency-dispersion, provides substantially decreased loss which is even lower than the metallic losses in a narrow-bandwidth regime. The large variation of the refractive index of the EIT medium results in the freezing of currents in the metallic inclusions of the metamaterial, thereby lowering loss. It has also been shown to be of use in generating narrow switchable propagating bands in metamaterials which behave like a dilute plasma. However, it must also be recognized that experimentally

implementing this scheme for controlling the response of metamaterials carries its own challenges. In addition to the accurate fabrication of an appropriately designed metamaterial at the desired frequency, the limiting effects of the metallic inclusions on the quantum phenomena must be overcome.

भारतीय प्रौद्योगिकी संस्थान कानपुर
INDIAN INSTITUTE OF TECHNOLOGY KANPUR

Chapter 2

Behaviour of Split-Ring Resonator Metamaterials at High Frequencies

The possibility of obtaining a metamaterial with a resonant magnetic response and negative refractive index at optical frequencies is a very exciting one. Most natural materials have a relative magnetic permeability that is approximately unity at optical frequencies, the same as vacuum, although their relative dielectric permittivity can be considerably different from unity. The reason for this is the weak coupling of the magnetic field of the light to the atoms in the medium. Landau and Lifshitz stated that the magnetic susceptibility ceases to hold any physical significance at relatively low frequencies and that accounting for the deviations of the permeability from unity is an over-refinement [42]. In addition, they state that in the optical frequency range and upwards, the magnetic susceptibility is no longer a meaningful quantity and one must put $\mu = 1$. As discussed in Sec. 1.3.3, designing metamaterials with an effective magnetic response at high (optical) frequencies is quite difficult. At optical frequencies, the permittivity of the metallic inclusions may become comparable in magnitude to the permittivity of the host medium, leading to the formation of surface plasmons at their interface. These surface plasmon resonances may however be used to realize alternative schemes for generating a negative permeability.

The electromagnetic response of slabs of Split Ring Resonators (SRR) at high (op-

tical and NIR) frequencies has been studied in this chapter. At these frequencies, effective medium descriptions gradually become inaccurate, finally resulting in the situation where the effective medium approach can no longer be applied. The retrieved parameters for the SRR metamaterials, when treated as reasonably effective media, themselves provide a few clues to the weakening of homogenization approaches. At optical frequencies, the metamaterials studied can no longer be homogenized and their response at optical frequencies has been studied using their band structures, reflectivity profiles and field maps. The negative phase velocity that these media can exhibit under suitable conditions is explained on the basis of localized plasmonic resonances, rather than the LC-resonance of an effective electric circuit driven by the magnetic field of the incident radiation. The electric field of the incident radiation is shown to be able to resonantly drive the SRR. Finally, the response of a series of SRRs, differing from each other only in the width of their capacitive gaps, has been investigated in detail. This allows us to study the gradual evolution of the magnetic resonance of the SRR, beyond the point where effective medium theories break down and finally when the SRR units are $\lambda/2$ — the photonic crystal limit.

2.1 The SRR embedded in a dielectric background

O'Brien et.al. [74] have described a split-ring resonator that is magnetically active at near-infra-red frequencies. Scaling to NIR frequencies was made possible by using a symmetric SRR with multiple capacitive gaps, which increased the capacitances 'connected' in series with each other. This, however, increases the size to wavelength ratio and makes the application of effective medium theories to a slab of such SRRs questionable. However, embedding the SRR in an appropriate dielectric medium reduces the size to wavelength ratio, by increasing the net capacitance of the SRR. The additional gaps need to be placed symmetrically to avoid bianisotropy, which has already been discussed in Chap. 1, Sec. 1.3.4.

An array of the SRRs they studied (Fig. 2.1 (a)) exhibited a negative permeabil-

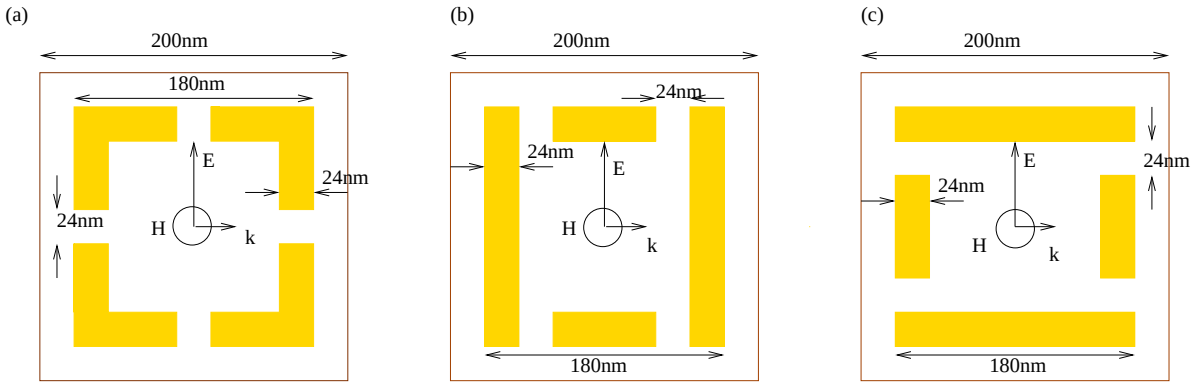

Figure 2.1: Schematic diagram showing the constructions of the unit cells of the SRRs embedded in a the lossless dielectric of $\epsilon = 4.0$. Arrays of such SRR exhibit a negative-μ stop band around a wavelength of 1.5μm. The unit cell is a square whose side $a = 300$ nm.

ity stop-band in the technologically important telecommunications wavelength band ($\sim$ 1.5μm). While acknowledging the fact that the ratio of the unit cell size to the wavelength for the SRR in question might not be small enough to classify the SRR array as a truly effective medium, the authors used a homogenization procedure outlined in Ref. [34] to retrieve μ_{eff}, ϵ_{eff} and n_{eff} for the system. They also found that the resonance frequency obtained from numerical simulations using the Transfer Matrix Method-based PHOTON codes [75, 76] differed from that obtained using a quasistatic analysis of an equivalent simple circuit ring structure for the SRR by about 15%. This difference in frequencies was attributed to the presence of parasitic self-capacitances which the ring model fails to take into account. However, these capacitances automatically come into play in a full-wave calculation. In this section, the effect of redesigning these SRRs (by modifying their self-capacitance) on their response to incident electromagnetic radiation has been investigated. Each case presented here differs only in that the capactive gaps have now been redistributed keeping the number of gaps constant. Thus, they are expected to respond identically to exciting radiation within the description of effective medium theories. A discussion of the numerical results for simulations performed using the PHOTON codes, considering these SRR to be embedded in an ideal, lossless dielectric medium of $\epsilon = 4.0$, follows below.

Consider the three SRR designs for the unit cell of a metamaterial as shown in

Fig. 2.1. The SRRs are considered to lie in the $x-z$ plane and assumed to be invariant along the y direction. The polarization of the incident radiation has been indicated in the diagram (Fig. 2.1). The usual SRR mechanism can be invoked to explain the functioning of these SRRs. The SRR shown in Fig. 2.1 (b) and Fig. 2.1 (c) are expected to have a lower resonance frequency owing to the increased self-capacitance across the shorter stubs. The metal itself was modelled as having a permittivity given by the Drude form:

$$\epsilon(\omega) = \epsilon_\infty - \frac{\omega_p^2}{\omega(\omega + i\gamma_m)}. \tag{2.1}$$

where ϵ_∞ represents the 'static' permittivity of the metal, ω_p is its plasma frequency and γ_m is the dissipation factor. Experimentally observed values for the permittivity of silver [77] were used in these calculations. The values of the constants in the above equation can be approximated as follows: $\epsilon_\infty = 5.7$, $\omega_p = 9.013$ eV (2176 THz) and $\gamma = 0.018$ eV (4.3 THz).

Band-gaps (indicative of a negative permeability band) were found to occur above the magnetic resonance frequencies of 186 THz, 184 THz and 179 THz for SRRs (a), (b) and (c) respectively as shown in Fig. 2.2 (a) - (c) and further corroborated by the reflectivity and the transmittivity plotted in Fig. 2.2 (d) - (f). At these frequencies, the unit cell size ($a = 300$nm), is $\sim \lambda/6$. The length-scales of the present set of SRRs enable the application of reasonably effective medium theories to them and allow them to be described by an effective ϵ and an effective μ. The effective medium parameters (μ_{eff}) extracted using the complex reflection and transmission coefficients [34] are shown in Fig. 2.3. Fig. 2.3 (a) - (c) show the effective impedance (Z) for each of the structures in Fig. 2.1 (a) - (c), respectively, and in each case, the peak in Z that is associated with the magnetic resonance can be clearly identified. Fig. 2.3 (d) - (f) represent the retrieved permeability for the structures shown in Fig. 2.1 (a) - (c), respectively. Thus, it is seen that in each case, the origin of the band gap for arrays of the SRR metamaterials in each of these cases can be traced to a magnetic resonance resulting in a negative permeability band. The same retrieval procedure also yields the effective permittivity

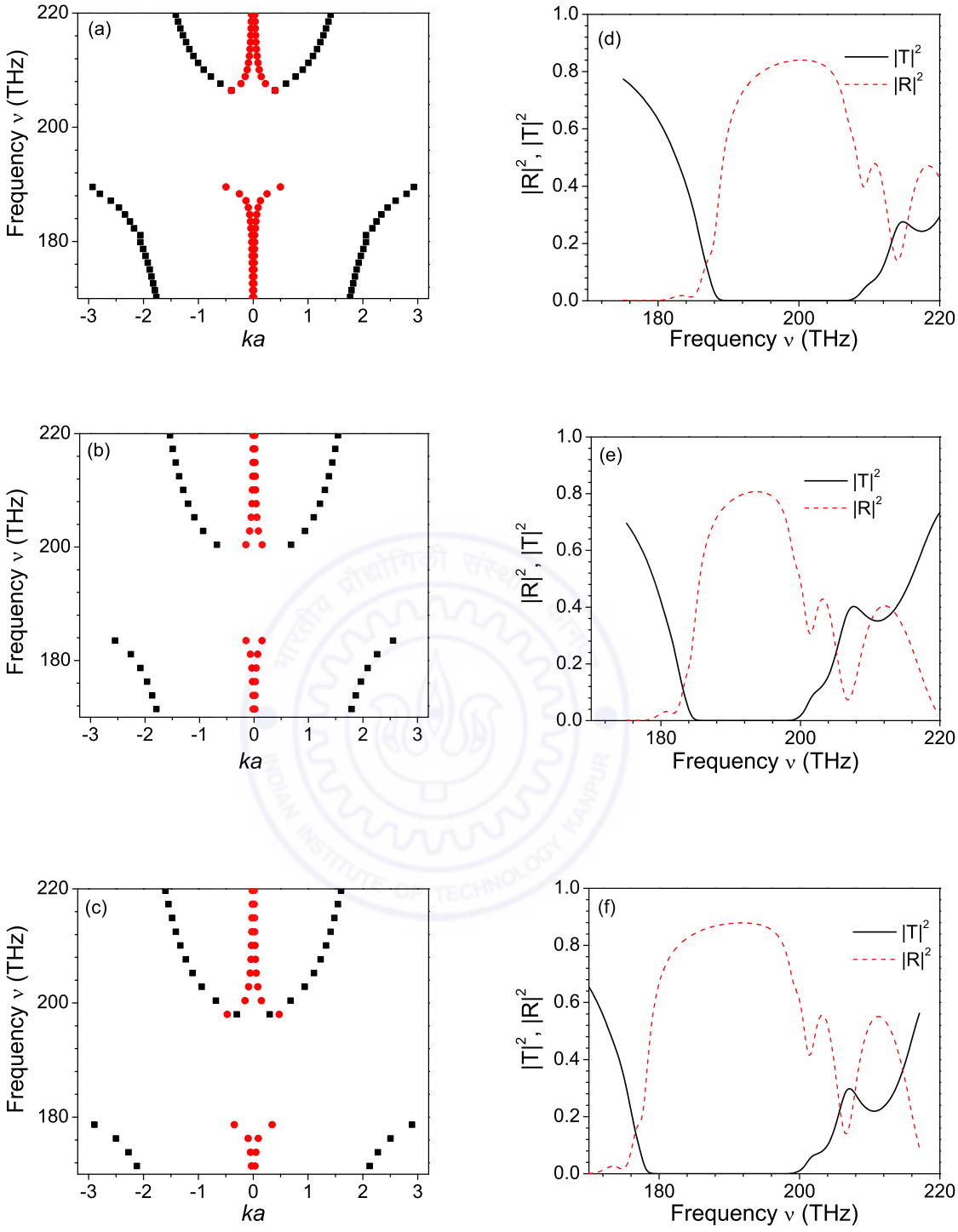

Figure 2.2: (a) - (c) The band structures for each of the SRRs shown in Fig. 2.1 (a) - (c) respectively. The band gaps are seen to occur at slightly different frequencies in each case.
(d) - (f) The reflectivity and the transmittivity corresponding to the band structures shown in (a) - (c) respectively, for individual slabs consisting of four layers of SRRs (a), (b) and (c) respectively. Additional peaks due to Fabry Pérot resonances are also observed.

of a slab consisting of such SRRs. As described in Chap. 1, ϵ_{eff} exhibits antiresonant behaviour, a fact which has been explained to be the result of the finite periodicity of the system [35].

Had the structures (a), (b) and (c) been truly homogenizable, they would have exhibited very similar electromagnetic behaviour as they have roughly the same total inductance and total capacitance. Their resonance frequencies could vary slightly due to their different capacitances. However, as the band structures and the retrieved permeabilities illustrate, a detailed look at their responses throws up a number of differences. The differences that one notes immediately are: (i) There is a shift in the resonance frequency from structure to structure. (ii) The bandwith of the negative μ band gap changes considerably. (iii) There is also a change in the strength of the μ resonance(the magnitude of the modulation of the μ in the negative permeability band).

The differences in the electromagnetic response of each of these SRRs can be understood as follows. Structures (b) and (c) which have lower resonance frequencies, possess a slightly higher capacitance due to the increased self-capacitance of the shorter middle stubs. The orientation of these SRR with respect to the electric field of the incident electromagnetic radiation also appears to play an important role. The electric field of the incident radiation is seen to be able to interact with two, none and four of the (charged) capacitive gaps in the cases of (a), (b) and (c) respectively. The effect of this interaction is manifested in the strength of the resonance that is observed in each case. It is to be noted that had the SRRs considered here been truly homogenizable (in the strictest sense of the term), their magnetic response would have been independent of their orientation with respect to the electric field of the incident radiation. This is so because these SRR are not bianisotropic due to their symmetric structure and in the quasi-static approximation, the dipole moments formed in the ring due to the accumulation of charge across the gaps cancel out. Further, it can be easily seen that structures (b) and (c) can be obtained from one another by means of a simple rotation by $\pi/2$ about the y-axis, an operation which should not affect their magnetic response along y. Thus, one can conclude that at length-scales and frequencies such as the ones considered

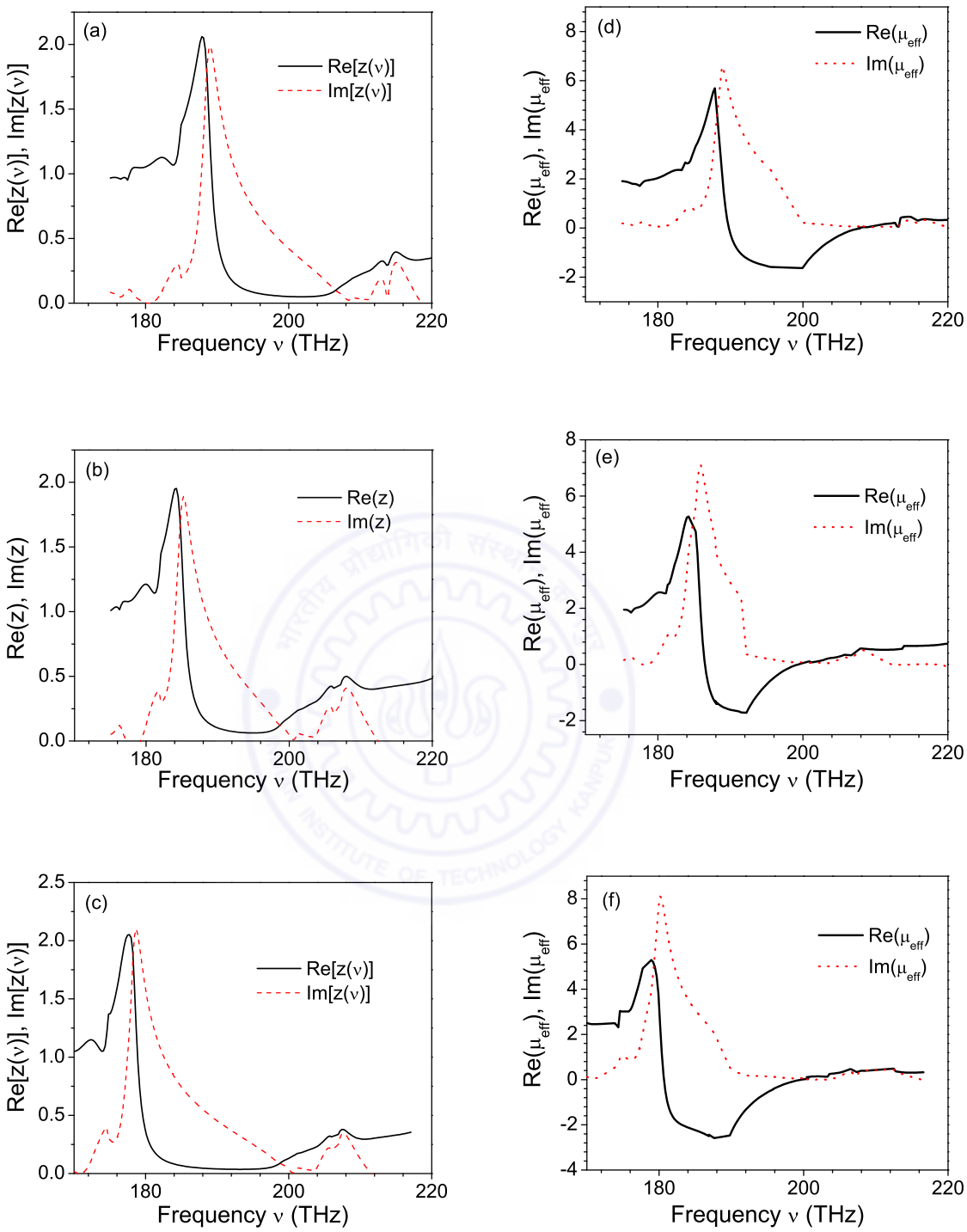

Figure 2.3: (a) - (c): The effective impedance Z for each individual slabs of the SRRs shown in Fig. 2.1 (a) - (c). The peak indicates the location of the magnetic resonance. (d) - (f): The retrieved permeability for corresponding to (a), (b) and (c), respectively. In each case, μ_{eff} takes up negative values but the exact resonance frequencies and the strengths of the resonances are different, even though the three structures are electrically similar.

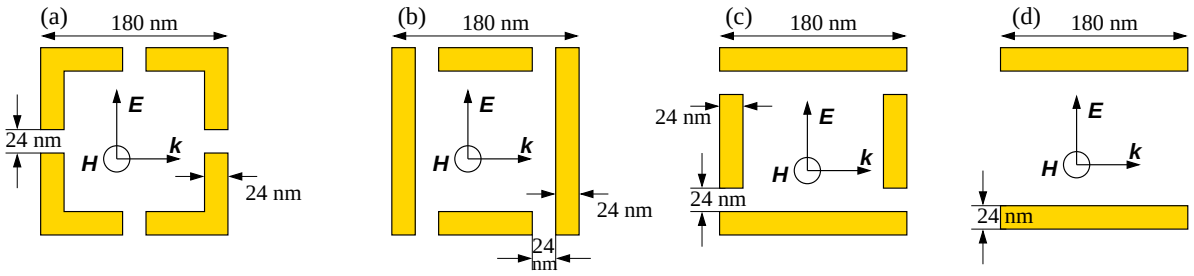

Figure 2.4: Schematic diagram for the SRRs whose electromagnetic response has been investigated in this section. The SRRs are in vacuum and the unit cell in each case is a square whose side is $a = 300$ nm.

here ($a \sim \lambda/6$), the effective medium descriptions of metamaterials show distinct signs of becoming inaccurate.

2.2 The SRR in vacuum

In the preceding section, we have discussed how the effective medium theory shows clear signs of becoming inaccurate at Near-Infra-Red (NIR) frequencies when $\sim \lambda/6$. The interaction of the electric field with the charges on the capacitive gaps of the SRRs leads to the next logical step — of simulating the electromagnetic response of arrays of these SRR after removing the embedding dielectric altogether, thereby increasing the resonance frequency. This was done so that the interaction (if any) of the electric fields with the capacitive gaps manifests itself in a much more dramatic manner. In this case, the unit cell size becomes of the order of $\sim \lambda/3$ at resonance. As before, radiation with the magnetic field oriented normally to plane of the SRR incident on an array of two-dimensional SRR of silver has been considered. The four types of SRR structures that have been investigated have been shown in Fig. 2.4 (a), (b), (c) and (d). For the other state of polarization, when the electric field is axially oriented, the SRR essentially behaves as a diluted metal and is highly reflecting. As before, invariance in the y direction (perpendicular to the plane of the SRR and parallel to the axis of the SRR) has been assumed. Due to similar sizes, except for case (d), the geometric inductance and the capacitance of the structures should be similar as a result of which they are expected to have similar magnetic properties. In fact, structure (c) is identical

to structure (b) but only rotated by $\pi/2$. Similarly, structure (d), the typical plate pairs of [78] is the same as structure (c) but with the shorter legs absent. Fig. 2.5 (a), (b), (c) and (d) illustrate the band structure diagrams in which both the real (solid squares) and imaginary parts (hollow circles) of the wave-vector at normal incidence have been shown. We have used the same colour (black or red) for the real and imaginary parts of a particular eigenvalue. The code computes a pair of eigenvectors for each frequency, one corresponding to a forward-propagating and one corresponding to a backward-propagating wave. These would have a positive and a negative imaginary component of the wave vector corresponding to a wave that decays in the forward direction (the direction in which energy is transported) or a wave that decays in the negative direction. The real parts of the wave vector usually have the same signs as the imaginary parts. The eigenvalues were chosen in such a manner that the solutions in the dissipative medium corresponded to a wave decaying in intensity along the forward direction (along the Poynting vector). Fig. 2.6 (a), (b), (c) and (d) show the transmittivity and the reflectivity for a slab composed of four layers of such SRRs respectively. These simulations were carried out using a refined version of the PHOTON codes based on the Transfer Matrix Method(TMM) [75, 76]. The additional peaks observed in the transmission spectra are the Fabry-Pérot resonances that occur as a result of multiple scattering from the edges of the slab. This indicates that the dissipation in the system is not very large and the wave can scatter multiply between the interfaces thereby interfering to create the Fabry-Pérot resonances. As before, experimentally obtained values for the dielectric permittivty of silver [77] were used in all the calculations.

The band structures of these structures and the corresponding reflectivity and the transmittivity shown in Fig. 2.5 and Fig. 2.6 highlight the completely different behaviour obtained in each of the three cases. Surprisingly, structure (b) and structure (c) (which is just the SRR in (b) reoriented) were found to behave very differently from each other. The most interesting new feature that is observed is that structure (a), structure (c) and structure (d) exhibit a negative refractive index in the second and third bands. This can be seen from the fact that waves with positive real part of the wave number have a

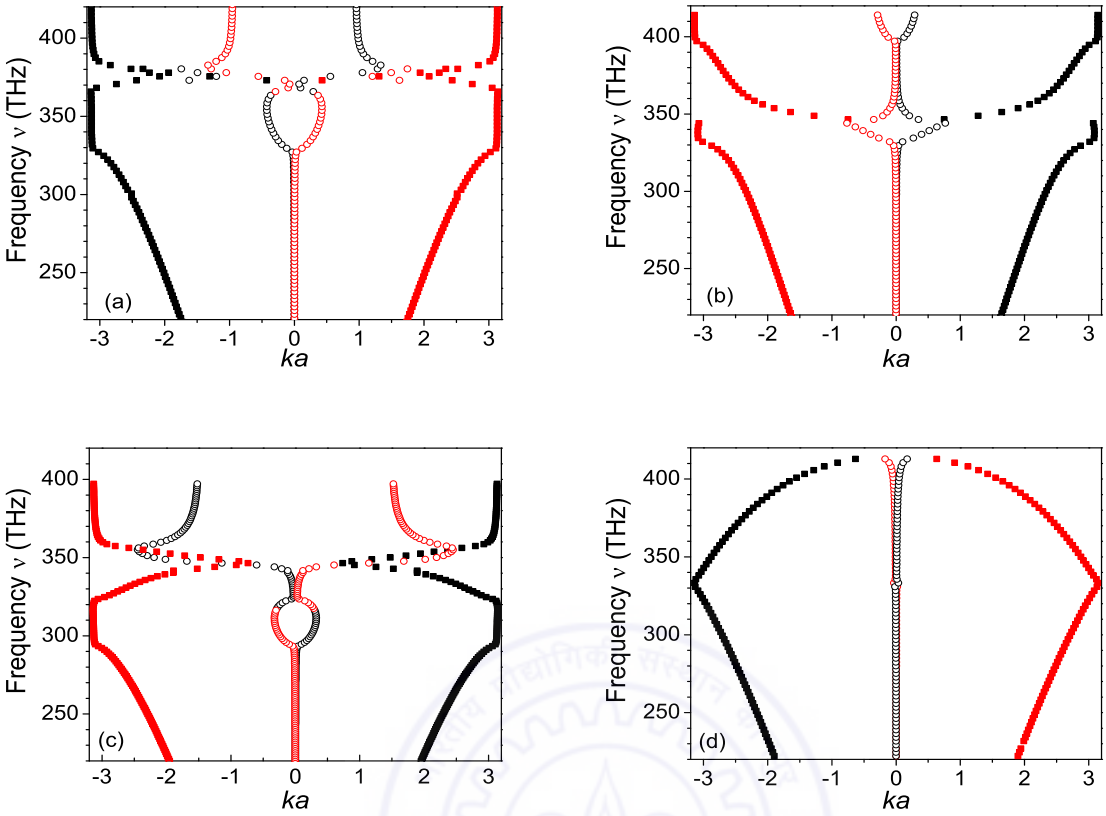

Figure 2.5: The band structures corresponding to the SRR structures shown in Fig. 2.4 (a), (b), (c) and (d), respectively. The striking difference between the response of each of these structures is noteworthy. The solid circles indicate the real parts of the wave vector while the hollow circles denote the imaginary parts. The same colour (red or black) has been used for the real and imaginary parts of the eigenvalues with positive or negative real parts. The opposite signs of the real and imaginary parts indicate negative phase velocity for SRR (a), (c) and (d). The unit cell size is $a = 300$ nm.

negative imaginary part of the wave number. The second band also has negative group velocity which is not separated from the higher positive group velocity band by a band gap. In the case (a), both these bands are very flat and almost dispersionless. In case (b), only a bandgap with an avoided crossing with the next higher band occurs. It is interesting to note that one obtains a nearly gapless dispersion with a negative phase velocity over a large band in case (d). Negative phase velocity bands are obtained in the case of (a), (c) and (d) as the fact that the real and imaginary parts of the wave-vector have opposite signs indicates. Thus, the existence of both the negative phase velocity - negative group velocity as well as negative phase velocity - positive group

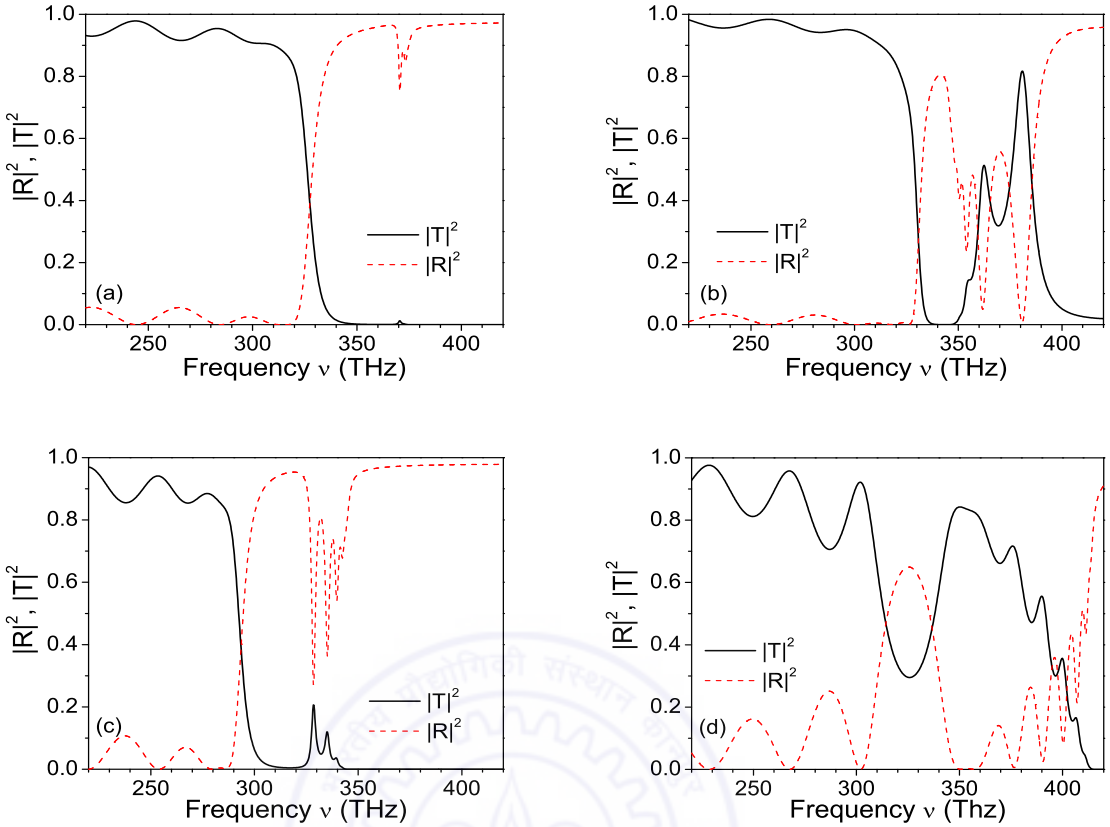

Figure 2.6: The reflectivity and the transmittivity for the for slabs consisting of four layers of the SRRs shown in Fig. 2.4 (a), (b), (c) and (d), respectively. These calculations confirm the result of the band structure calculations for each SRR. The transmission spectra show the additional peaks due to the Fabry-Pérot resonances occuring as a result of multiple reflections from the edges of the slab.

velocity bands that were reported in an experiment on metamaterials [79], is confirmed at the optical frequencies (338 THz $\sim$ 882 nm) considered here. At these frequencies, the free space wavelength of the light is about thrice the size of the unit cell and only one transmitted and reflected beam is obtained from a slab of such SRRs as all other higher-order diffracted beams are evanescent. Interestingly, the band structure for the plate pairs in Fig. 2.4 rotated by $\pi/2$ (shown in Fig. 2.16, in the next section) is again completely different.

The only identifiable difference between first three systems lies in the number of capacitive gaps (and consequently the charge distributions) that the electric field of the incident radiation can interact with. Evidently, the electric field can interact with the

charge distributions formed across two, nil or four capacitive gaps in the SRRs (a), (b) and (c) respectively. The enhanced interaction of the electric field of the incident wave with the SRR is clearly manifested in the response of each of these SRRs. In fact, the band structure of each SRR depends crucially on the number of capacitive gaps across which the electric field can interact with the charge distribution. This was verified by redistributing the gaps in SRR (a) so that the electric field of the incident radiation interacts with the charge distibutions formed across two capacitive gaps in each case as shown in Fig. 2.7. Evidently, the band structures are almost identical in the two cases.

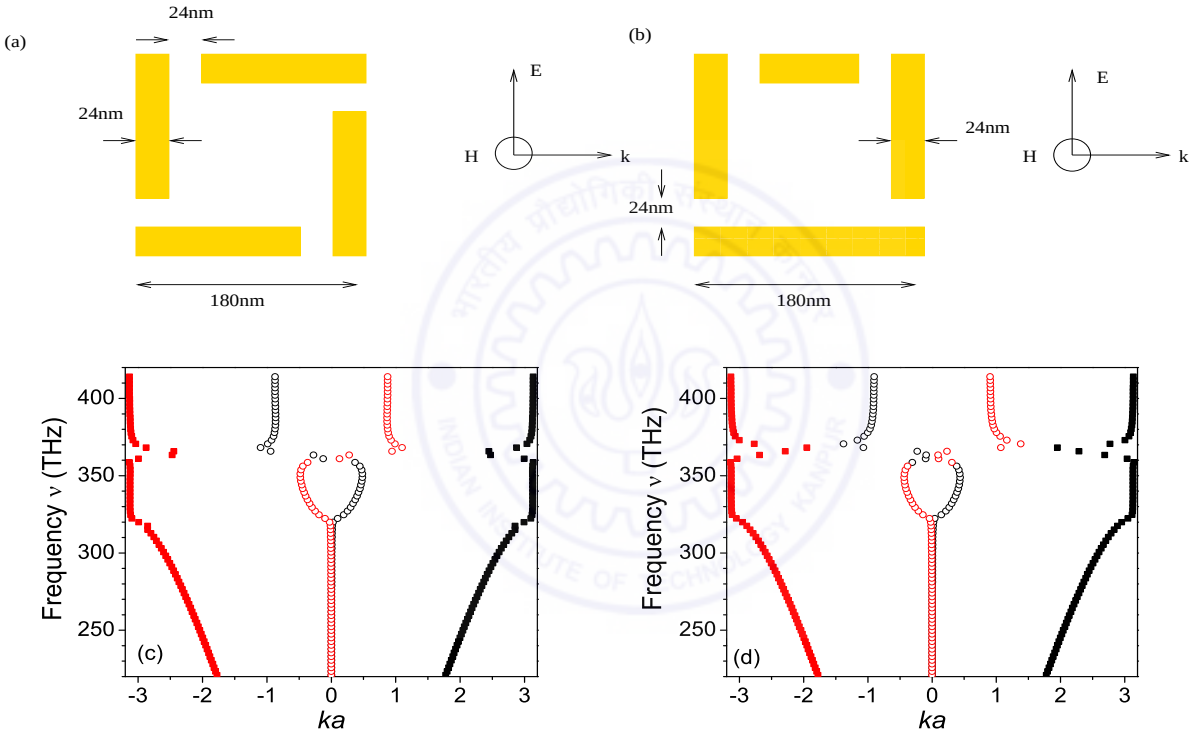

Figure 2.7: Band structures for the SRR(a) in Fig. 2.4 after the gaps have been redistributed. Note that in each case, **E** can interact with the charge distributions formed across two of the gaps, just as in the case of SRR (a). The band structures obtained are identical in every respect. As before, the unit cell size is $a = 300$ nm.

At these high frequencies, the usual SRR mechanism of an equivalent resonant series LC circuit cannot be used to explain the functioning of the SRR [74]. In addition, there exist significant phase differences across a single SRR of either type (b) or type (c), whose size ($\sim \lambda/3$) becomes a significant fraction of the wavelength at the bandgaps. This enables the transient building up of charge densities at various points on the SRR

with which the electric field interacts, due to retardation. The dipoles are not completely screened out. This was corroborated by computing the spectral problem for a small (3 X 4) array of SRR of type (c) using the COMSOL^{TM} FEMLAB software with perfectly matched boundary layers (PML) placed at least more than 1000 nm away. There is a mismatch of about 5 THz between the results obtained from COMSOL^{TM} and those obtained using the Transfer Matrix Method. The COMSOL^{TM} results give a frequency about 5 THz larger than the TMM codes, which could be due to the differences in the discretization methods or the finite array size effects and PML conditons in the COMSOL^{TM} calculations. For typical eigensolutions near 340 THz, the magnetic fields were concentrated inside the SRRs as in the case of the classical SRR, but pointed in opposite directions in adjacent layers (See Fig. 2.8). Similarly, the electric fields were found to be concentrated in the capacitive gaps with large dipole-like fields in the gaps whose signs reversed across the SRR. The displacement fields were found to 'circulate' around the SRR similar to a current. These observations lead one to conclude that the electric field is exciting the anti-symmetric plasmon modes [80] in the vertical legs across the SRR with opposing currents (displacement and real) in the two legs. Such effects have been studied in pairs of nanowires as described below.

The resonant response of wire pairs: The resonances in an isolated nanowire of finite length can be related to the excitation of surface plasmon polariton modes on the metal-vacuum interface. When two nanowires are positioned close to each other, their plasmon modes interact. When the electric field of the incident plane wave is parallel to the wires and the magnetic field is perpendicular to their (common) plane, two different kinds of plasmon polariton waves (differing in symmetry) can be excited [80]. The symmetric combination of the two polariton waves leads to the symmetric excitation of the electric dipole moments in both the wires. Parallel currents are resonantly excited. The antisymmetric combination corresponds to the excitation of antiparallel currents in the wire pair, by the magnetic field of the incident wave. Along with the displacement current in between the wires, it appears as if there is a resonant excitation of the magnetic dipole moment of the system. For the systems under study, the interaction

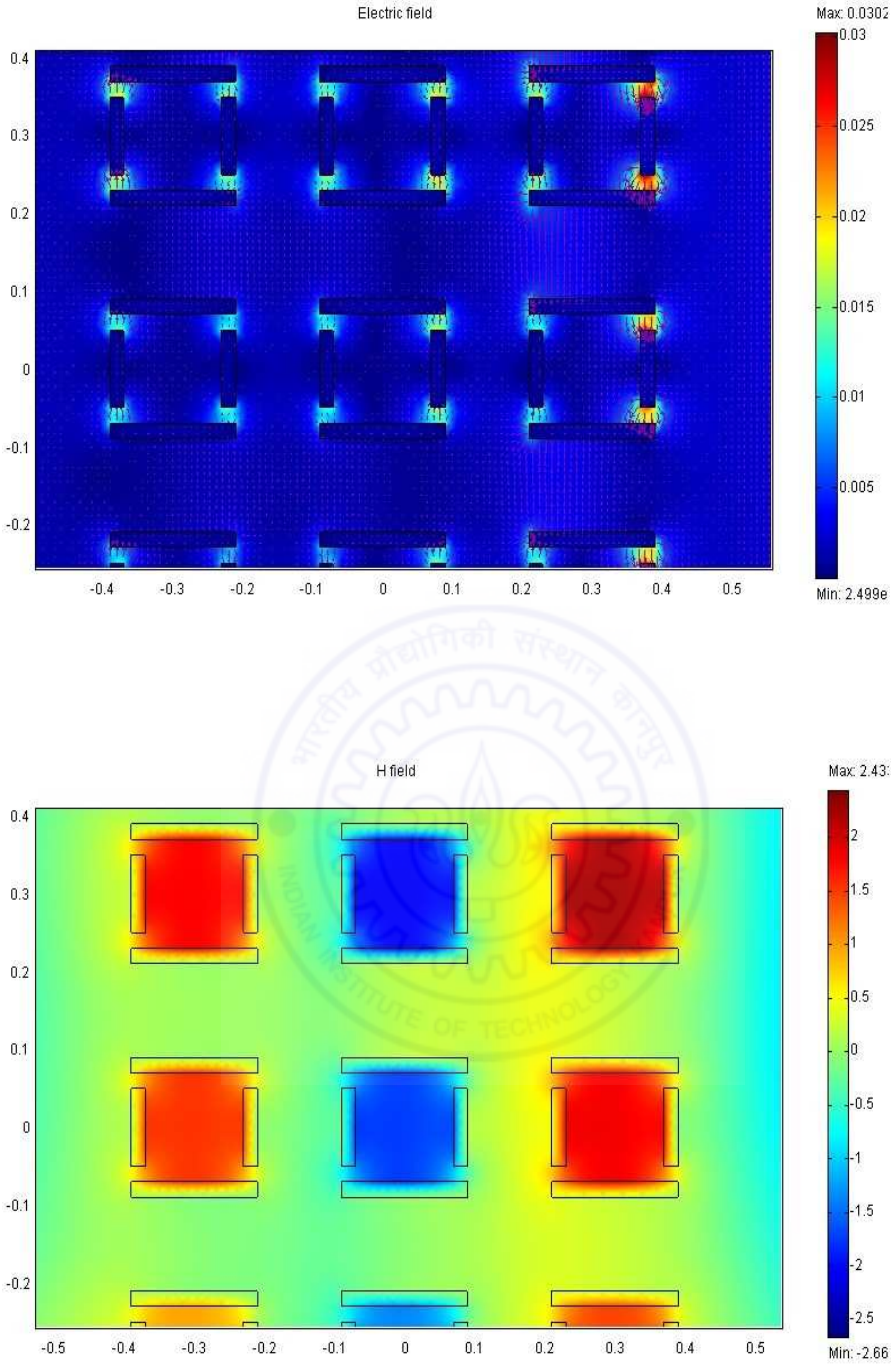

Figure 2.8: The electric (top) and the magnetic (bottom) field maps calculated using FEMLAB for an array of SRRs of the type (c) in Fig. 2.4. The electric fields are concentrated within the capacitive gaps while the magnetic fields are confined within the rings, highlighting the magnetic nature of the resonance.

with the dipoles in the capacitive gaps is crucial for the excitation of the anti-symmetric mode. Thus, under suitable conditions, the electric fields can contribute to reinforcing the effects of the magnetic fields which leads to a large magnetic dipole moment.

2.2.1 Focussing and imaging with slabs of negative phase velocity metamaterials

The focussing of a line source at a frequency of 340 THz by a finite flat slab composed of an array of SRR in the form of a Veselago lens [81], was simulated. This frequency is where the 'light line' ($\omega = kc$) intersects the negative phase and group velocity band for the SRR (c) corresponds to the condition $n = -1$. The orientation of the SRR (b) or (c) turns out to be crucial although an image is formed in both the cases. The field maps for the imaging of a line source by 2-D SRR slabs have been shown in Fig. 2.9 and Fig. 2.10 (left panels). In either case, the Poynting vector streamlines (right panels), depicting the energy flow in the system, converge in the transverse direction to a small region, indicating the position of the image formed. In the case of SRR (b), the slab transmits very little due to the bandgap and a faint image is formed on the other side. In the case of SRR (c), a brighter image is formed as it is located within a transmittive band. While the focussing action of the slab consisting of SRR (b) is due to negative dielectric permittivity, that occuring in the case of the slab of SRR (c) is due to negative phase velocity, suggestive of a negative index of refraction [81].

Therefore, it can be concluded that the behaviour of an array of SRR (b) is similar to a stack of cut-wires (plates), with the electric field of the incident radiation directed along the plates (wires). This medium is known to behave like a plasma and exhibit negative dielectric permittivity [38]. The capacitive gaps within the SRR do not play much of a role in the phenomena observed in this case. This was again verified by closing the capacitive gaps whereby it was found that the weak imaging effect remained essentially unchanged with hollow square cylinders. The band structure calculation for the hollow square cylinders shows a wide band-gap in the frequency range considered

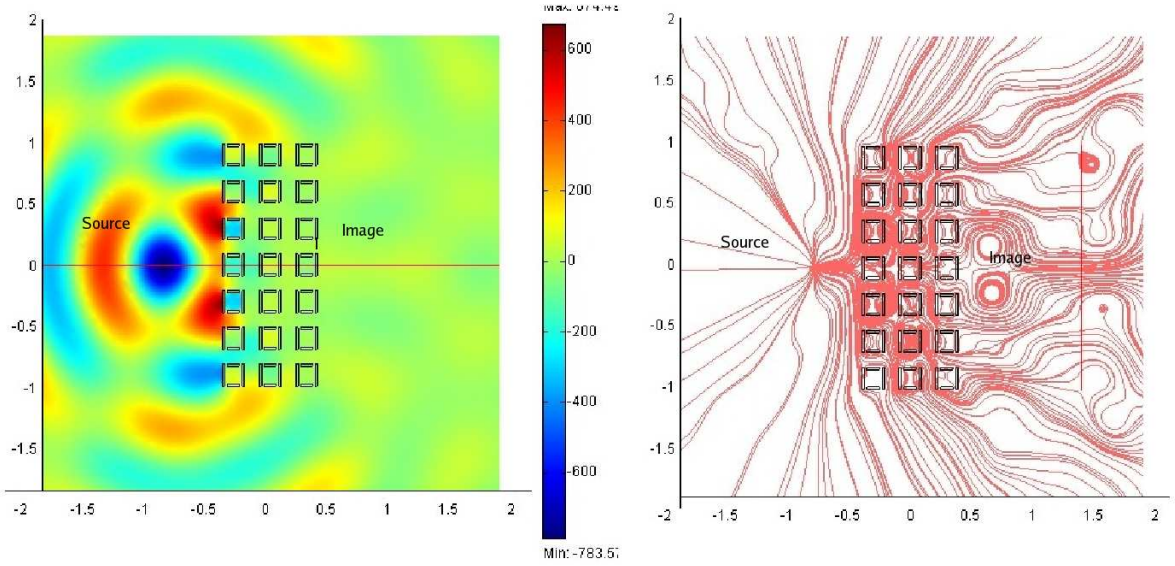

Figure 2.9: Left: The focussing action by an array of SRRs of type (b) (Fig. 2.4) in the form of a Veselago lens. A line source is placed on the left-hand side of the slab. An image is clearly formed on the right-hand side as seen from the field map.
Right: The energy streamlines also converge in the transverse direction indicating the focussing. The transmittivity of the slab is very low due to the band gap and a faint image is formed.

here (See Fig. 2.13). The entire system thus behaves effectively as a diluted metal and the focussing of light is due to a negative dielectric permittivity over a wide range of frequencies [82]. The focussing effect has been verified over a reasonably wide range of frequencies — 338 THz to nearly 355 THz, while the best resolution is obtained at $\sim$ 348 THz. Due to the finite size and numbers of the SRRs used and the dissipation present in the system, no claims about the extent of the sub-wavelength resolution possible here, are made. In the case of SRR (a) as well, a negative phase velocity band and hence, imaging as a Veselago lens, is possible.

Comparison with All-angle Negative Refraction (AANR): All-angle negative refraction is a phenomenon observed in photonic crystals [83]. It does not require a negative index of refraction and a few simple criteria are sufficient to achieve this effect. All-angle negative refraction is a purely band structure-dependent effect, depending only on the convexity of the equifrequency surfaces and a negative effective photonic mass. Luo *et. al.* [83] have identified three key factors which guarantee single beam AANR.

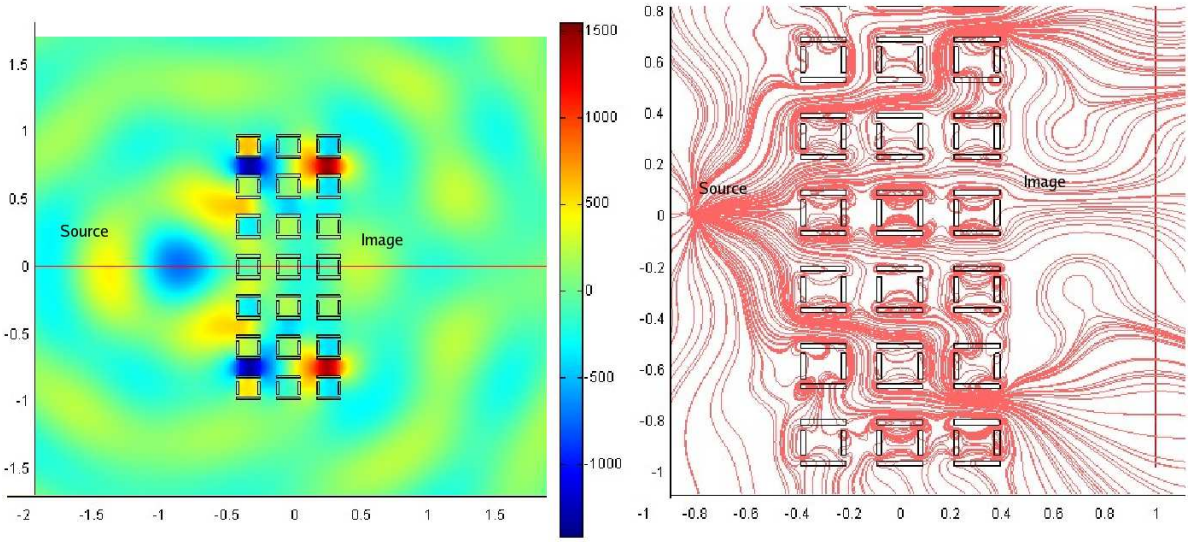

Figure 2.10: Left: The focussing action by an array of SRRs of type (c) (shown in Fig. 2.4) in the form of a Veselago lens.
Right: A line source is placed on the left-hand side of the slab. The image, clearly formed on the right-hand side, can be seen on the field map. The energy streamlines also converge in the transverse direction indicating the focussing. In this case, the transmission by the slab is considerably higher the frequencies lie in a propagating band and the image formed is much brighter.

They are:

(i) The equifrequency contour of the photonic crystal should be convex with a negative effective photonic mass.

(ii) All the incident wave vectors at such frequencies lie within the constant frequency contour of the photonic crystal.

(iii) The frequency must lie below $0.5 \times 2\pi c/a_s$, (where a_s is the surface parallel period) in order to avoid diffraction. In photonic crystals exhibiting negative refraction, the group velocity is never directed opposite to the phase velocity, confirming that one is operating within a regime of positive refractive index.

In comparison, the systems we have studied may exhibit a negative phase velocity when oriented appropriately with respect to the electric field, suggestive of a negative index of refraction, even though the length scales involved do not permit homogenization.

The focussing effect was confirmed by shifting the source around and putting in

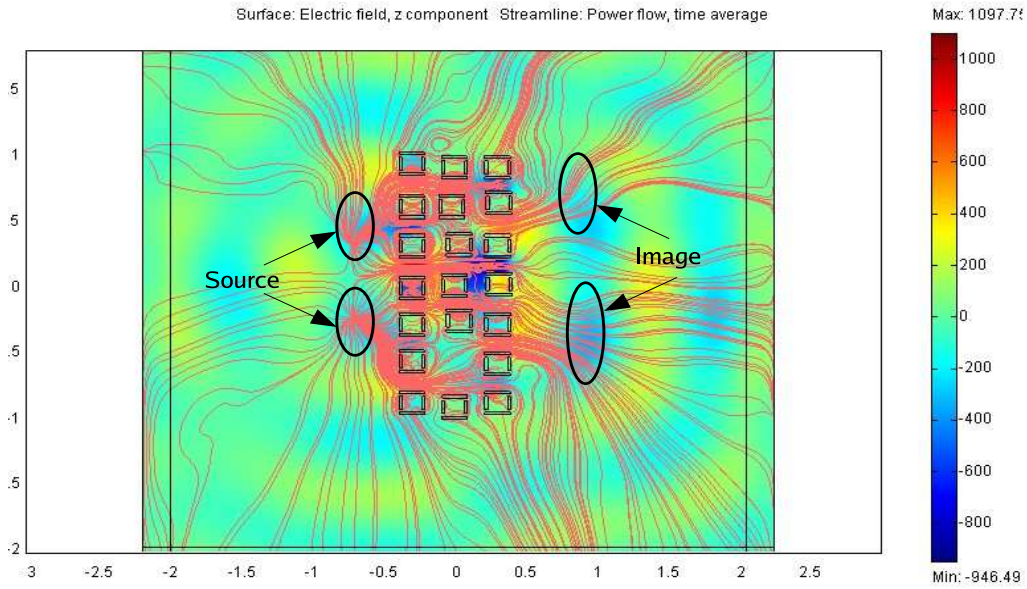

Figure 2.11: Focussing by a disordered, finite-sized array of SRR of type (c) in Fig. 2.4. This figure clearly indicates that imaging effects are not due to band-dispersion effects but rather a consequence of the localized resonances of the system. A single SRR in the array is missing, as shown. The positions of the two sources and their corresponding images have been indicated in the figure. The figure shows the field map for the electric field normal to the plane of the array.

multiple sources. It was also found to remain unaffected if the periodicity of the array was disturbed (Fig. 2.11). Subwavelength focussing effects by evanescent waves were not considered as the wavelength is comparable to the length scales of the structure. The fact that the imaging effects were not a consequence of band-dispersion effects such as the all angle negative refraction (AANR) was verified by disordering the positions of the SRRs to upto 10% of the lattice and also by removing some SRRs in the array. The images survived with some marginal changes in the fields. This confirms the fact that the imaging effects have their origin in the localized resonances of the system and the periodicity of the array is not an essential requirement for the focussing effects.

The occurrence of the negative phase velocity bands can be explained by considering the enhanced interaction of the electric field with the individual inclusions. The large phase shifts for the radiation across a single unit cell implies that the electric dipole moments formed across the capacitive gaps are not screened out effectively. In the case of SRR (c), the electric field can also drive the currents around the loop by interacting

with the dipole moments across the capacitive gaps. This in turn reinforces the inductive effect due to the varying magnetic field. In case (b), the electric dipole response of the finite wires (plates) dominates because the wires (plates) in the adjacent cells along the x-axis can couple through the electric field. In case (c), the longer wires (plates) are along the $z-$direction and the coupling along x is much lesser. Thus, the magnetic action is reinforced in this case, compared to the plasma-like action in the case of SRR (b). It is thus possible explain the negative phase velocity (suggestive of a negative refractive index) in case (c) and the band gap suggestive of a negative dielectric permittivity in case (b) on the basis of these. The system has localized plasmonic resonances of electric and magnetic character respectively, giving rise to the band gaps on either side of the negative phase velocity band. In case (d), the two plasmonic resonances are apparently degenerate, resulting in an almost gapless dispersion.

Defining homogeneous effective medium parameters such as ϵ_{eff} and μ_{eff} does not make sense here as the process of homogenisation itself is questionable when the unit cell size is a significant fraction of the free space wavelength at resonance (in this case, $a \sim \lambda/3$). Hence the discussion here has been confined to the negative phase velocity (suggestive of a negative refractive index) and its possible origin based on the physical aspects of the systems, and no attempt at defining ϵ_{eff} and μ_{eff} for the shown incidences has been made.

2.3 Evolution of the magnetic response

The equivalent circuit model of the SRR shows that the capacitive gaps in the structure are of the greatest importance in determining its resonance frequency. Indeed, at these high frequencies, it is much easier to vary the resonance frequency of the SRR by altering the gap width (and hence, the capacitance), than it is by altering the inductance. The sensitivity of SRRs to varying gap widths and its effect on the effective medium response has been presented here. The electromagnetic response of a variety of metamaterial structures were simulated and the gradual change with geometric structure in their

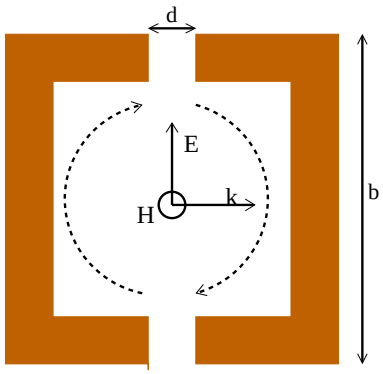

Figure 2.12: Schematic diagram for the SRRs whose electromagnetic response with varying d has been studied in this section. The unit cell is $a = 300$ nm, while the sides of the SRR are 180 nm long.

electromagnetic response was studied. The calculated photonic band structures and the reflectivity and the transmittivity (for slabs consisting of four layers of the unit cells), have been presented here. The responses of these media show a variety of phenomena as one progresses from the effective medium behaviour of the metamaterial, through the weakening and the breakdown of this picture, to the limit of large unit cells where the length scales involved ($a \sim \lambda/2$) lead to the conclusion that Bragg scattering leads to the formation of the band gap. The wave impedance (defined as $Z = \sqrt{\mu/\epsilon}$) calculated for each of these structures, gives an idea of the nature of the response of the medium at frequencies near the band-gap(s). In certain cases, when the wavelength at resonance is large compared to the unit cell size, the metamaterial can be treated as an effectively homogeneous medium near the band gap (resonant) frequency. In such cases, effective material parameters can be assigned to it, uniquely characterizing the origin of its response as electric or magnetic in nature. The conditions under which such a treatment is valid has already been discussed in detail in the preceding sections. If the medium cannot be homogenized, field maps of the electric and magnetic fields at the frequencies of interest (using FEM) may be used to judge the nature of the electromagnetic response of the medium.

Fig. 2.12 shows a schematic representation of the unit cell of the symmetric SRR, with two capacitive gaps, whose electromagnetic response as the gap width d is varied is

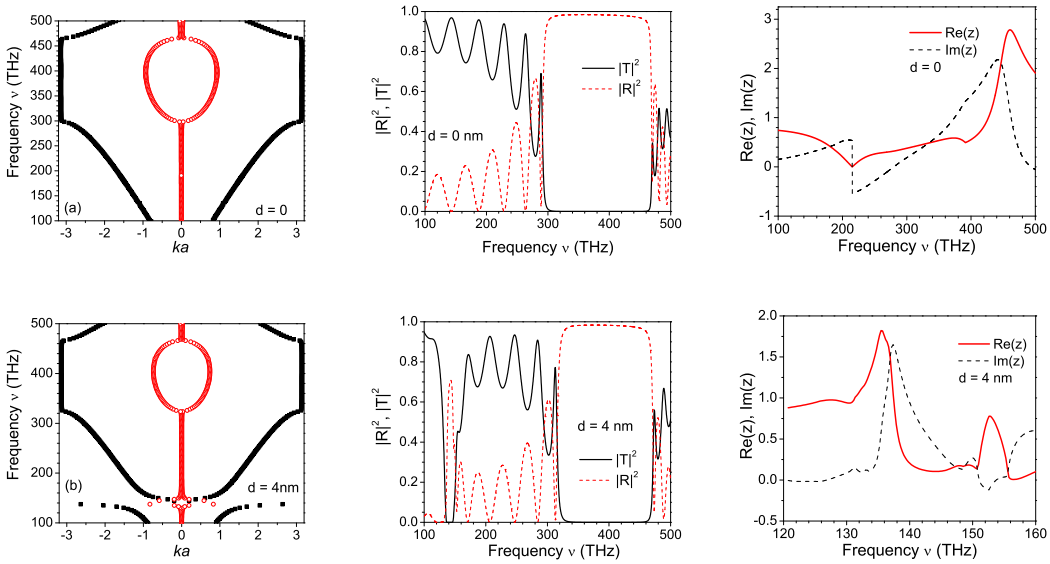

Figure 2.13: Left: Band structures for the SRR shown in Fig. 2.12 as the gap width increases from 0 to 4 nm. A negative permeability band gap due to a magnetic resonance appears when $d = 4$ nm.
Middle: The reflectivity and the transmittivity for a slab consisting of two layers of SRRs, whose capacitive gaps correspond to $d = 0$ nm and $d = 4$ nm, respectively.
Right: The calculated impedance Z for the gap widths of 0 and 4 nm, respectively.

presented in this section. The unit cell considered in our calculations is square with side $a = 300$ nm in each case. The width of each of these SRR structures is 24 nm across. The length of the sides is $b = 180$ nm. Eight different situations have been studied, beginning with hollow square cylindrical structures to plate pairs oriented perpendicular to the electric field of the incident radiation. The evolution of the SRR response with changing capacitance is presented. As before, the response of these systems has been calculated using the PHOTON codes [75, 76]. These calculations are essentially two-dimensional with the magnetic field being aligned along the axis of invariance of the system (the y-axis), normal to the plane of the SRRs.

(i). The first case considered is the response of an array of hollow square cylinders. This system may have a net diamagnetic response with μ_{eff} taking up values which are positive but < 1. This is simply the analogue of the array of cylinders which shows a net diamagnetic response, but with a square rather than a circular cross-section. Although the array exhibits a single large band gap extending from 290 THz to 483THz, this band

gap cannot be attributed to a negative effective permeability. A plot of the spectrum of the reflectivity and the transmittivity of the system (for two layers of unit cells) (Fig. 2.13, top panel) shows that the transmittivity drops to nearly zero from about 80% at approximately 299 THz and remains at this level upto frequencies of 483 THz before rising again to levels of 70%. As expected in the case of multilayered systems, Fabry Pérot resonances occurring as a result of multiple scattering from the edges of the layers, are seen both below and above this band gap. The effective impedance of this structure shows a region of low impedance near the lower band edge, suggesting that the effective permittivity of the medium is high and an associated dielectric resonance for this system. However, since the wavelength at this point is nearly $\lambda/3$, the effective medium approach cannot be applied and we do not attribute an effective permittivity. However, due to the subwavelength size, Bragg scattering is also not expected to dominate. The focussing of p-polarized light by an array of such hollow cylinders (discussed in Sec. 2.2.1) suggests a negative dielectric permittivity for this system. The negative permittivity probably arises due to the coupling of the electric dipoles formed in adjacent unit cells by the electric field, in a behaviour akin to the cut-wire system [35].

(ii). Next, the response of a slab consisting of split ring with two splits opposite each other (where each split is 4 nm wide), is presented (Fig. 2.13, bottom panel). The band structure of this medium shows the occurrence of two band gaps, one around 121 THz and the other at $\sim$ 289 THz. The lower (narrower) gap in this case is easily identified as the negative permeability band gap of the SRR (due to the classical LC resonance in the ring) while the one at higher frequencies is the same as the band gap encountered in case (i). The transmittivity of the slab drops nearly to zero from about 85% near 132 THz and remains nearly zero till 152 THz when it rises, exhibits a series of Fabry-Pérot resonances and then again shows a region of very low transmittivity from 289 THz to 483 THz, just like the one observed in the case of the hollow structure. The first stop band is a region where the impedance of the system is high, as compared to the second stop band where the effective impedance is low. This high impedance is typical of the SRR-based metamaterials, which have a high magnetic permeability at resonance. At the

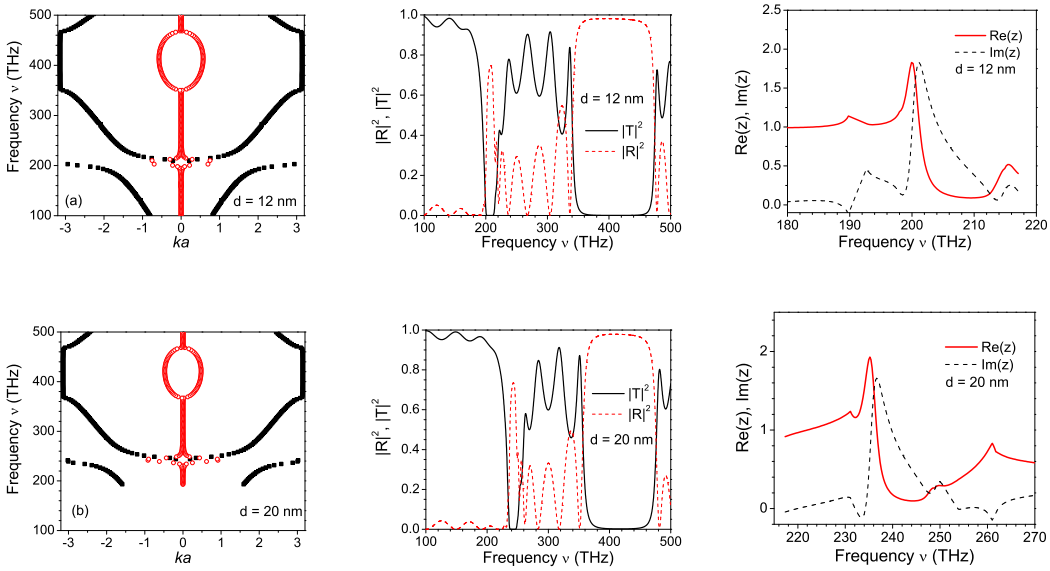

Figure 2.14: Left: Band structures for the SRR shown in Fig. 2.12 as the gap width is increased to 12 nm and 20 nm. The negative permeability band gap moves towards higher frequencies.
Middle: The reflectivity and the transmittivity for a slab consisting of two layers of SRRs, whose capacitive gaps correspond to $d = 12$ nm and $d = 20$ nm, respectively.
Right: The calculated impedance Z for the gap widths of 12 and 20 nm, respectively.

frequency where the first band gap is formed, the medium is homogenizable ($a \sim \lambda/8$) and effective parameters can be extracted. The retrieved permeability shows a negative μ band at the location of the first gap.

(iii). In the third case, the widths of the capacitive gaps of the SRR are increased to $d = 12$ nm. Once again, two band gaps are seen (shown in Fig. 2.14, top panel). The first band gap now occurs at a higher frequency (due to the reduced capacitance of the SRR) while the second band gap too shifts upwards and narrows down as well. The upper edge of the second band gap, however, remains at 483 THz. The lower gap is the narrower of the two. The reflectivity-transmittivity profile of this system is similar to the previous one with two stop bands where the first narrow band is the usual SRR negative μ-band while the second is the same stop band seen in (i) and (ii). The lower edge of the second stop band also shows a slight upward shift. The effective permeability in the first gap (where $a \sim \lambda/7$) is negative, confirming that it arises due to the LC resonance of the SRR.

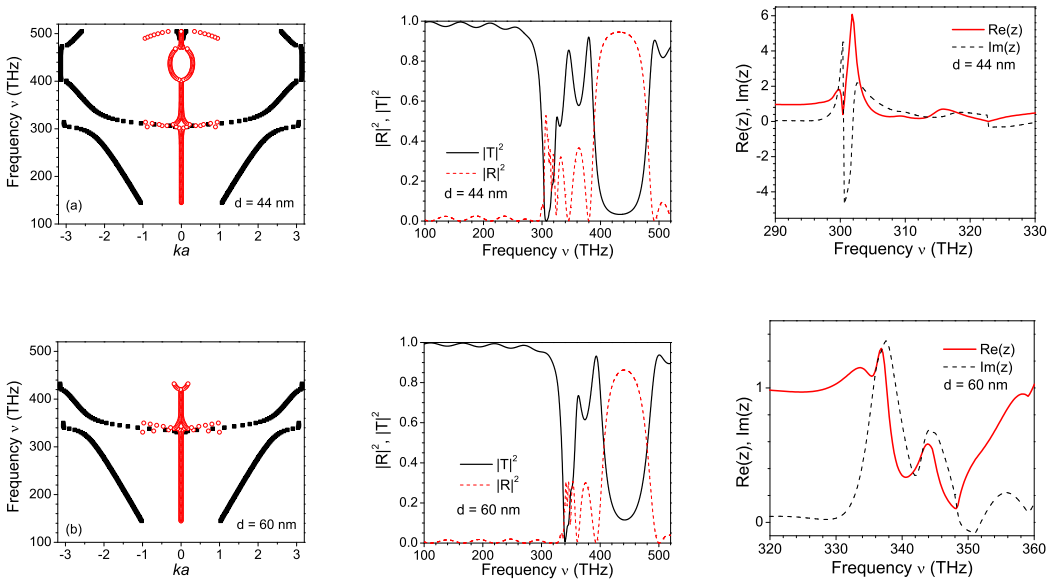

Figure 2.15: Left: Band structures for the SRR shown in Fig. 2.12 as the gap width increases to 44 nm and 60 nm. The negative permeability band narrows and moves upwards with increasing gap width d.
Middle: The reflectivity and the transmittivity for a slab consisting of two layers of SRRs, whose capacitive gaps correspond to $d = 44$ nm and $d = 60$ nm, respectively.
Right: The calculated impedance Z for the gap widths of 44 and 60 nm, respectively.

(iv). In this case, the capacitive gap width of the SRR is increased to 20 nm. The response of an array such SRRs has been shown in Fig. 2.14, bottom panel. The calculated band structure for an array of such SRR shows two bands as before, with the first one progressively having moved upwards in frequency and the band width narrowing in extent. The second one also shifts upward in frequency but its upper edge remains remains unaltered at 483 THz. The reflectivity-transmittivity spectrum for a double layered slab of these SRR is qualitatively similar to those obtained in the case of (ii) and (iii). The negative permeability band is at a higher frequency as the capacitance is lowered again while the second stop band is not much altered. The unit cell is $a \sim \lambda/4$ at the resonance. At these length scales, the interaction of the electric field of the incident radiation with the SRR itself is expected to strongly affect the retrieved parameters, and this is the frequency regime where the effective medium theories weaken considerably.

(v). The fifth case we present consists of SRRs whose capacitive gaps have a width of 44 nm each. In this case, the net capacitance of the structure is reduced substantially

and the first band gap is pushed high up in frequency such that a is only slightly greater than $\lambda/3$ (see Fig. 2.15, top panel). The lower stop band narrows down to the verge of disappearing due to the weakening of the SRR resonance. The large capacitive gap prevents strong capacitive coupling between the two parts of the SRR. Homogenization becomes truly problematic here. The second gap occurring at higher frequencies is still prominent although it, too, narrows down. The plots of the reflectivity and the transmittivity of a double-layer of unit cells still shows the considerably weakened SRR stop-band. In the region of the second stop band, the transmittivity drops to around 30%, as compared to the near zero values obtained in the earlier cases. A comparison of the reflectivity and the transmittivity spectra shows that the behaviour of the system has changed considerably from that seen in (ii), (iii) and (iv).

(vi). In the sixth SRR, the widths of the capacitive gaps, $d = 60$ nm. From the band structure, it is evident that the lower band due to the magnetic resonance and the upper bands nearly intersect (Fig. 2.15, bottom panel) . The second gap also narrows further, leading one to suspect that the physical phenomena responsible for the original gap formation, such as the coupling between adjacent cells, are ceasing to be dominant. This reflectivity and the transmittivity for two layers of unit cells of the SRR show a clearer manifestation of this phenomenon. The first stop band is weaker while the second one changes considerably in character. Instead of another stop-band, we find that both the reflectivity and the transmittivity drop to about 50%. Evidently, the phenomena which influenced the response of the system earlier are now being replaced by another set. The two band frequencies are now close to each other and we are gradually approaching the limit where Bragg scattering begins to dominate (i.e., when $a \sim \lambda/2$).

(vii). In the next stage, the gaps are further increased to 76 nm. Due to the lowered capacitance of the structure, the lower band is pushed further upwards, resulting in the disappearance of the first band gap. The higher band gap narrows as well. The reflectivity-transmittivity profile changes completely, with only one narrow stop band being seen at the point where both the band frequencies overlap (Fig. 2.16, top panel) .

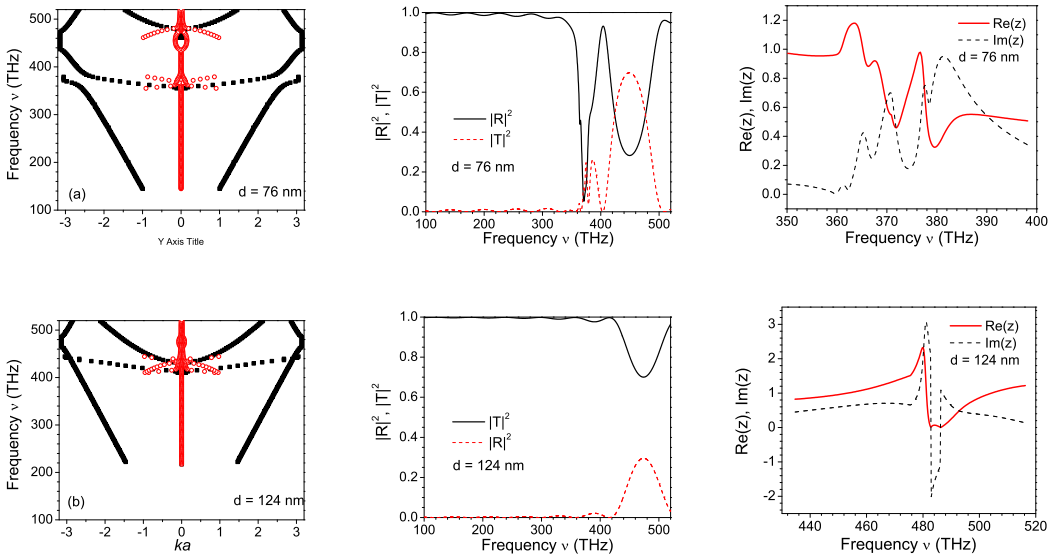

Figure 2.16: Band structures for the SRR shown in Fig. 2.12 as the gap width increases to 76 nm and 124 nm. The negative permeability band gradually disappears with increasing gap width.
Middle: The reflectivity and the transmittivity for a slab consisting of two layers of SRRs, whose capacitive gaps correspond to $d = 76$ nm and $d = 124$ nm, respectively.
Right: The calculated impedance Z for the gap widths of 76 and 124 nm, respectively.

(viii). Finally, the SRR system is reduced to a pair of plates parallel to each other. These plates are 124 nm apart and are aligned parallel to the electric field of the incident radiation. The bands for this structure actually intersect at $\sim$ 459 THz. The plots of the reflectivity and the transmitivity are completely featureless, except for a drop in transmission and an accompanying increase in reflection at $\sim$ 483 THz (Fig. 2.16, bottom panel) . This frequency corresponds to $a \sim \lambda/2$. Here, the only effect expected to dominate is Bragg scattering. All other resonant effects, whether it is the LC resonance seen in SRR systems due to their geometric structure, or those arising from plasmonic effects, are completely wiped out. This band structure is again totally different from that exhibited by the plate pairs in the previous section. The plate pairs shown here are highly transmittive in the frequency range around $\sim$ 435 THz. This is in sharp contrast with the behaviour of the structure shown in Fig. 2.4 (d). Moreover, the plates are aligned parallel to the electric field of the incident radiation which can allow them to behave like the cut wire media described earlier.

The results obtained in this section have been summarized in Table. 2.1.

Table 2.1: The changing nature of the response of the SRR whose structure has been shown in Fig. 2.12 as the gap width d varies.

SRR	Fig. no.	Gap width (nm)	Resonance (1) (THz)	Resonance (2) (THz)	Nature of resonance
i	Fig. 2.13	0	None	300	(1) None (2)Electric
ii	Fig. 2.13	4	138	326	(1)Magnetic, (2)Scattering
iii	Fig. 2.14	12	204	350	(1)Magnetic, (2)Scattering
iv	Fig. 2.14	20	238	370	(1)Magnetic, (2)Scattering
v	Fig. 2.15	44	304	400	(1)Magnetic, (2)Scattering
vi	Fig. 2.15	60	340	420	(1)Magnetic, (2)Scattering
vii	Fig. 2.16	76	370	447	(1)None, (2)Electric
viii	Fig. 2.16	124	None	466	(2)None, (2)Electric

2.4 Conclusion

To summarize, the response of SRR-based metamaterials at high frequencies when the unit cell size becomes a significant fraction of the wavelength and effective medium theories gradually become inaccurate and finally become inapplicable, has been studied. Even in the case of SRRs which can be treated as reasonably effective media and described by means of an effective permeability at telecommunications wavelengths, there are definite signs that the electric field of the applied radiation begins to interact with the capacitive gaps of the SRRs. This leads to small but significant variations in the strength and the width of the magnetic resonance. Further, we have shown that symmetric SRRs in vacuum can have negative phase velocity (negative refractive index) at optical frequencies if oriented such that the electric fields can drive the dipoles formed across the capacitive gaps. In the orthogonal orientation, they behave like cut-wire media with a negative dielectric permittivity band gap. The simple paradigm of a negative μ_{eff} due to a L-C resonance in the SRR driven by the magnetic field alone breaks down and the negative phase velocity (negative refractive index) that arises in the limits when homogenization becomes problematic has its origin in the localized plasmonic resonances of the system. Our theoretical work is a confirmation of the measurements of different combinations of positive and negative group velocity and negative phase velocity reported in Ref. [79]. A slab consisting of these SRRs functions as a Veselago lens, a phenomenon which continues to persist even if the periodic arrangement of SRRs in the slab is disordered to about 10 %. The effect is thus completely different from the all angle negative refraction occurring in photonic crystals. Finally, a systematic study of the evolution of the magnetic response with decreasing capacitance of the SRR has been presented. The appearance of the negative permeability gap and its final disappearance with the dominance of scattering processes and the increased interaction of the fields with the structure as the photonic crystal limit of the structure is approached has been traced out. It has been shown that one can retrieve effective medium parameters only up to a certain limit for decreasing capacitance of the same structure. Beyond it, the L-C resonance paradigm of the SRR breaks down and finally the band gap narrows

down to the point of disappearance. Along with this, scattering processes gradually gain importance until the limiting case of $a \sim \lambda/2$, where it is expected to be the dominant effect. In this case, however, the metamaterial can also behave like the cut-wire media. As far as the length scales of the system at the frequencies of interest are concerned, it is to be noted that here $a \sim \lambda/2$, the regime where Bragg scattering can play a dominant role in a periodic system. Therefore, in this case, the system can no longer be termed as a 'metamaterial' and certainly cannot be described by effective medium theories.

भारतीय प्रौद्योगिकी संस्थान कानपुर
INDIAN INSTITUTE OF TECHNOLOGY KANPUR

Chapter 3

Coherently Controlled Metamaterials at Optical Frequencies

Metamaterials have undoubtedly altered our perception of the interaction of electromagnetic waves with matter within the framework of Maxwell's equations. A couple of decades ago, the ideas of coherent control [54] of quantum systems via quantum interference [84] revolutionized light-matter interaction, exemplified by the demonstration of phenomena like Electromagnetically Induced Transparency (EIT) [59, 60], subluminal (slow light) [62] and superluminal propagation of light [61], lasing without inversion [85, 86] etc. Metamaterials, on the other hand, hold out the possibility of negative refraction [12, 2], perfect lenses [11], invisibility cloaks [87, 88], etc, at frequencies determined solely by their underlying geometric structure. The design and the fabrication metamaterials of that operate at optical frequencies is a difficult, although not an impossible task [89]. This is due to the breakdown of effective medium theories and the deviation of metals from perfect conductor-like behaviour at high frequencies.

Metamaterials need to be *controllable*, *low-loss* and possibly even *reconfigurable* for future applications. A few methods for the control of their response, both passive [90, 91] as well as dynamical, have already been demonstrated. Dynamical methods of control

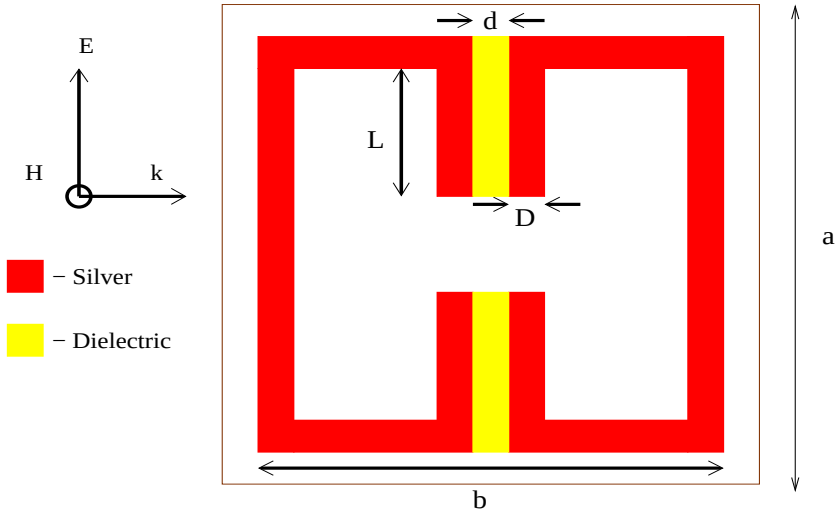

Figure 3.1: Schematic diagram for the SRR used for studying the effect of a frequency-dispersive permittivity on the magnetic response. The dimensions of the SRR are as follows: a = 600 nm, b = 312 nm, L = 144 nm, D = 24 nm, d = 24 nm. The dark (red) area indicates the metallic region while the lighter (yellow) region represents the capacitive gaps where an appropriate medium can be embedded. A slab of SRR such as this is truly homogenizable ($\sim \lambda/10$) at the frequencies of interest.

include using photoconductive semiconductor inclusions [92, 93], liquid crystal inclusions [94], magnetostrictive effects [95], Kerr nonlinearities [74], adding fixed quantities silicon-nanosphere/ethanol solution [96] and optical gain [97] in the metamaterial structures. In this chapter, schemes for manipulating and switching the response of SRR-based metamaterials that show resonant magnetic effects, using coherent optical phenomena like EIT have been demonstrated. This is achieved by actively tuning the capacitance of the structures via an appropriate resonant, frequency-dispersive dielectric background. The proposed scheme involves the interaction of the narrow atomic/molecular resonance with the broader structural resonance of the metamaterial. We use a quantum mechanical phenomenon to parametrically control the purely classical metamaterial resonance.

3.1 Analytical description

In this section we study the magnetic response of SRR-based metamaterials when they are embedded in a frequency-dispersive dielectric background. We consider a metamaterial consisting of arrays of symmetric SRR (usually of metals such as gold or silver), as shown in Fig. 3.1. These arrays lie in the horizontal plane and are stacked up vertically. The size of the individual inclusions ($\sim \lambda/10$) makes it possible to describe the array as an effective medium at the frequencies of interest. Metamaterials composed of such SRR have been shown to possess a resonant magnetic response for **H** threading the loop of the SRR and the effective permeability, μ_{bare} of the SRR array, is given by [44]:

$$\mu_{\text{bare}}(\omega) = 1 + \frac{f_m \omega^2}{\omega_m^2 - \omega^2 - i\Gamma_m \omega}, \tag{3.1}$$

as has also been discussed in Sec. 1.3.2. Here, the magnetic resonance frequency $\omega_m = \frac{1}{\sqrt{LC}}$, where L and C are the total inductance and the total capacitance of the structure [44], f_m is the filling fraction while the factor Γ_m, which governs the effective dissipation present in the SRR medium, is related to the intrinsic dissipation in the metal defined according to the Drude model for the dielectric permittivity. A medium of such SRRs has already been shown to exhibit a negative permeability that gives rise to a band gap in a frequency range above ω_m if Γ_m is small enough.

An array of such SRRs is embedded in a medium having a frequency-dispersive dielectric permittivity. This may either be a resonant Lorentz-type dispersion, or EIT-like under the application of a pair of coherent control and probe fields. As already discussed, in the first case, the relative permittivity of the medium is given by the expression

$$\epsilon(\omega) = 1 + \frac{f_e^2}{\omega_e^2 - \omega^2 - i\gamma_e \omega}, \tag{3.2}$$

where $f_e^2 = Ne^2/m\epsilon_0$ (N is the number density of (atomic) oscillators, ϵ_0 is the permittivity of free space while e and m are the electronic charge and mass, respectively), ω_e

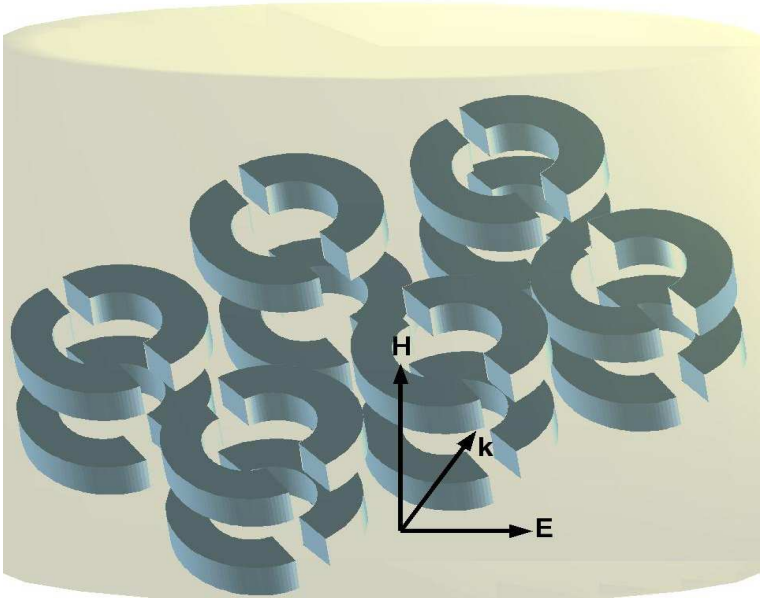

Figure 3.2: A section through a SRR-based metamaterial showing the periodic arrangement of the SRRs, embedded in a host medium with a dispersive permittivity, indicated by the grey region in the figure.

is the dielectric resonance frequency and γ_e is the dissipation factor. Such a dispersion can be realized by using for example, resonant quantum dots or choosing a Raman transition [98] with a strong pump field ensuring that the resonant Raman probe frequency is close to the magnetic resonance frequency of the metamaterial, ω_m. The dependence of the level spacing in quantum dots upon their size and their tunability makes them suitable for this purpose.

In the second case, when the medium exhibits EIT, the permittivity for the probe field is given by [69]

$$\epsilon_{\rm EIT}(\omega) = 1 + \frac{\kappa(\omega_1 - \omega)}{(\omega_1 - \omega)^2 - \frac{\Omega_c^2}{4} - i\gamma_{13}(\omega_1 - \omega)}. \tag{3.3}$$

Here $\omega_1 = \frac{E_1 - E_3}{\hbar}$ (as shown in Fig. 1.13), Ω_c is the Rabi frequency of the control field defined as $\Omega_c = \frac{\vec{d}_{12}\cdot\vec{E}}{\hbar}$, $\kappa = (N_a|\langle d_{13}\rangle|^2)/(\epsilon_0\hbar)$ is the strength of the transition, N_a is the atomic density, γ_{13} and d_{13} represent the decay rate and the dipole moment, respectively, between the atomic levels $|1\rangle$ and $|3\rangle$ while d_{12} represents the dipole moment between levels $|1\rangle$ and $|2\rangle$ (see Fig. 1.13). It should be noted that in the absence of the control

field, the dispersion obtained is the same as in the case of the Lorentz permittivity.

In the presence of the embedding medium, the capacitance per unit length of individual SRR units becomes strongly frequency-dependent as

$$C_{\text{eff}}(\omega) = \frac{\epsilon(\omega)L}{d}. \tag{3.4}$$

This makes the resonance frequency of the composite medium (ω_{eff}) appear frequency dispersive as $\omega_{\text{eff}} = \frac{\omega_m}{\sqrt{\epsilon(\omega)}}$. Thus, the effective permeability of the composite metamaterial now formally becomes:

$$\mu_{\text{eff}}(\omega) = 1 + \frac{f_m\omega^2}{\omega_{\text{eff}}^2 - \omega^2 - i\Gamma_m\omega}. \tag{3.5}$$

The sharply resonant nature of $\epsilon(\omega)$ results in the SRR medium showing a resonant magnetic response at multiple frequencies. These predominantly occur above and below ω_m, depending on whether the frequency of the incident wave is greater than or lesser than ω_e, respectively. The proximity of the two resonances to each other determines the extent of the modulation produced in μ_{eff}. It is to be noted that the frequency-dispersive resonance frequency (ω_{eff}) is a complex quantity. The new resonance frequencies are the solutions of the transcendental equation

$$\text{Re}\left[\omega_m^2/\epsilon(\omega)\right] - \omega^2 = 0, \tag{3.6}$$

while $\text{Im}[\omega_m^2/\epsilon(\omega)]$ quantifies the dissipation in the effective medium. Essentially, the presence of the dispersive dielectric permittivity of the embedding medium turns the SRR into a resonantly driven, *actively tuned* LC-circuit. The capacitance of the LC-circuit becomes frequency dependent, allowing the satisfaction of the resonance conditions Eq. (3.6) at multiple frequencies. The corresponding negative-μ band gap of the 'bare' SRR splits into two or more band gaps.

In the presence of $\epsilon(\omega)$, the filling fraction f_{eff} and the dissipation parameter of the composite metamaterial can be viewed as effective frequency dependent quantities

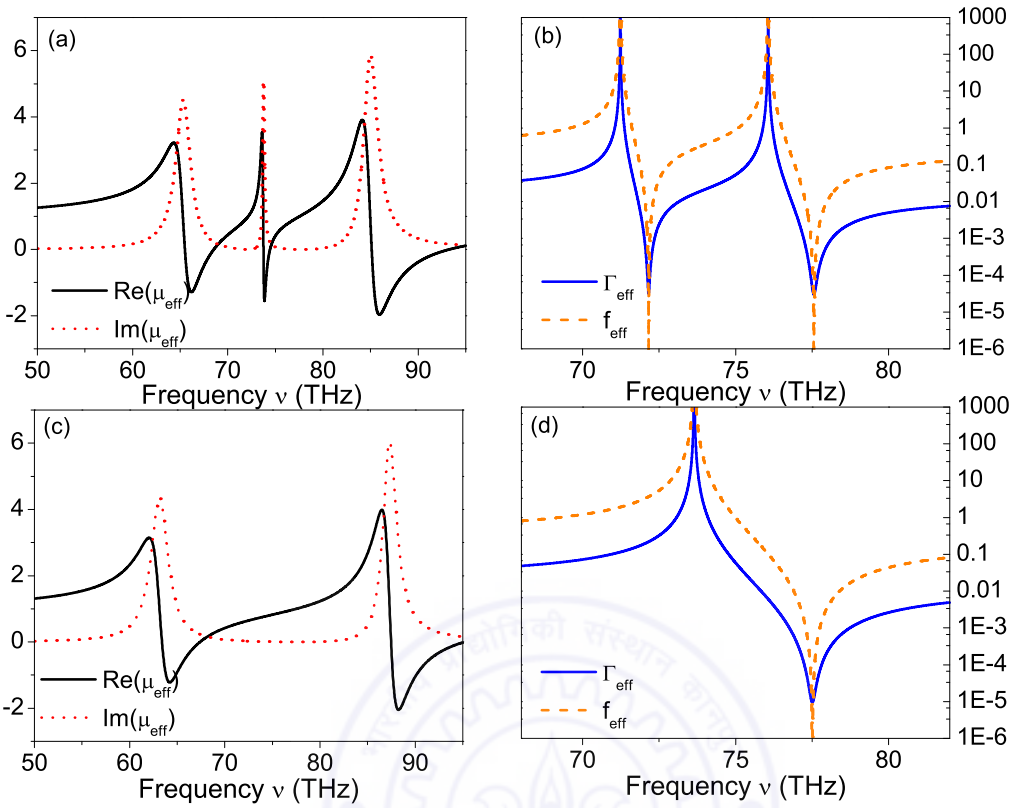

Figure 3.3: (a): The frequency dependent μ_{eff} and (b): Γ_{eff} and filling fraction f_{eff} (obtained analytically) for the SRR metamaterial in the presence of a embedding dielectric medium displaying EIT.
(c) and (d): The same quantities for the SRR metamaterial embedded in a medium which has a resonant Lorentz permittivity. In this case, the magnetic resonance occurs at 74.9 THz and the dielectric resonance is at 73.6 THz

whose behaviours are completely transformed by the resonant background. The effective filling fraction f_{eff} and the effective dissipation parameter Γ_{eff} have the following generic forms in the presence of a frequency-dispersive background:

$$f_{\text{eff}}(\omega) = f_m \left[\{\text{Re}\left[\epsilon(\omega)\right]\}^2 + \{\text{Im}\left[\epsilon(\omega)\right]\}^2\right], \tag{3.7}$$

$$\Gamma_{\text{eff}}(\omega) = \omega_m^2 \frac{\text{Im}\left[\epsilon(\omega)\right]}{\omega} + \Gamma_m \{\text{Re}\left[\epsilon(\omega)\right]\}^2 + \Gamma_m \{\text{Im}\left[\epsilon(\omega)\right]\}^2. \tag{3.8}$$

A detailed analysis of properties of a composite metamaterial where the embedded dielectric has a Lorentz or EIT dispersion is now presented. If the background dielectric

medium has a Lorentz-type dispersion, the following expressions for f_{eff} and Γ_{eff} are obtained:

$$f_{\text{eff}} = f_m \left[1 + \frac{f_e^2(2(\omega_e^2 - \omega^2) + f_e^2)}{(\omega_e^2 - \omega^2)^2 + (\gamma_e\omega)^2}\right], \tag{3.9}$$

$$\Gamma_{\text{eff}} = \Gamma_m + \frac{\Gamma_m f_e^2(2(\omega_e^2 - \omega^2) + f_e^2) + \omega_m^2 f_e^2 \gamma_e}{(\omega_e^2 - \omega^2)^2 + (\gamma_e\omega)^2}. \tag{3.10}$$

Along with the two new magnetic resonance frequencies and a split in the negative μ-band, a region with significantly reduced absorption is observed between the two resonances (Fig. 3.3). In fact, the $\text{Im}[\mu_{\text{eff}}]$ is observed to pass through a minimum at the resonant frequency of the bare SRR if $\omega_m = \omega_e$ (Fig. 3.3 (c)). There is also a significant change in the nature of f_{eff} and Γ_{eff} around the frequency ω_e (Fig. 3.3 (d)). The large values of f_{eff} at ω_e is due to the resonant enhancement of the cross-section of the SRR structural unit: the SRR appear much larger to radiation at resonance than they actually are. The reduction in absorption at ω_e is due to the vanishing of the currents in the SRR. This results from an interplay of two currents giving rise to different charge densities. The first of these is due to the current induced in the SRR unit by the magnetic field of the incident radiation. The second arises due to the fluctuating electric polarization of the embedding dielectric background by the electric field of the incident light. At resonance, the two are out of phase with each other leading to the freezing of currents in the SRR. The proximity of ω_e to ω_m determines the extent of modulation of the μ_{eff} response. In other words, the interaction between the electric and magnetic resonances is the strongest when ω_e lies in the vicinity of ω_m, $(\omega_m \pm \Gamma_m)$. Otherwise, the two resonances are virtually uncoupled.

The magnetic response of the composite metamaterial embedded in an EIT medium exhibits multiple magnetic resonances as seen in Fig. 3.3 (a). This is again accompanied by substantially reduced absorption within two frequency bands. The strength and the detuning of the control field can both be used to shift the positions, widths, slopes and dissipation associated with the various resonances in μ_{eff}. In fact, this scheme is more amenable to control as compared to the one described earlier because the detunings of

the probe and the control beams (both positive and negative) can be used to shift the EIT line centre and hence, the frequencies at which the absorption in the metamaterial is reduced. Again, the effective filling fraction and the modified dissipation parameter are given by

$$f_{\text{eff}} = f_m \left[1 + \frac{\kappa\Delta(2(\Delta^2 - \Omega_c^2/4) + \kappa\Delta)}{(\Delta^2 - \Omega_c^2/4)^2 + (\gamma_{12}\Delta)^2}\right], \tag{3.11}$$

$$\Gamma_{\text{eff}} = \Gamma_m + \frac{\Gamma_m\kappa\Delta(2(\Delta^2 - \Omega_c^2/4) + \kappa\Delta) + \omega_m^2/\omega\kappa\Delta^2\gamma_{12}}{(\Delta^2 - \Omega_c^2/4)^2 + (\gamma_{12}\Delta)^2}, \tag{3.12}$$

where $\Delta = \omega_1 - \omega$.

From the preceding expressions, we find that the new filling fraction f_{eff} increases close to the resonant frequency while Γ_{eff} exhibits sub-classical ($\Gamma_{\text{eff}} \ll \Gamma_m$) values around the atomic resonances (Fig. 3.3 (b)). At the EIT line centre frequency (ω_1), f_{eff} and Γ_{eff} are found to have the same values as the bare SRR medium. Thus, when $\Delta_c = 0$ (Δ_c is the detuning of the control field) and the separation between the dressed states (See Chap. 1, Sec. 1.5.2) is the separation between the Autler-Townes doublet, namely $\Delta = \pm\frac{\Omega_c}{2}$ [99], $\Gamma_{\text{eff}} = \Gamma_m$. As noted before, the reduction in absorption is a manifestation of the vanishing currents in the SRR loops. It is interesting to note that the losses are reduced significantly only for the regions where $\text{Re}\,[\mu_{\text{eff}}] > 0$, (see Fig. 3.3), in agreement with the speculations of Stockman that a non-dissipative negative parameter regime does not manifest for any metamaterial [100].

If the metamaterial has been designed to exhibit a resonant response at the frequency of the EIT line centre in the absence of medium, the resonant magnetic response of the composite metamaterial is found to be such that $\text{Re}\,[\mu_{\text{eff}}] \to 1$ (with an associated imaginary part) exactly at the EIT line centre. However, if $\omega_m \neq \omega_1$, the response of the composite at the EIT line centre is simply the value of μ_{bare} at the frequency ω_1. It should be emphasized that since we are dealing with a resonant system with a highly dispersive lineshape, changes of the control parameter (ϵ_{L} or ϵ_{EIT}) can lead to large-scale changes in response (μ_{eff}) at a given frequency, due to the shift in the effective resonance frequency. All these theoretical deductions have been confirmed by

the numerical studies on these systems that have been presented in the next section.

3.2 Numerical Simulation of the SRR metamaterial at mid-IR frequencies

Numerical simulations using the PHOTON codes based on the Transfer Matrix Method (TMM) [75, 76] were carried out to verify our theoretical predictions. We present two examples, the first being the canonical example of subwavelength-sized SRR made of silver at mid-infrared (mid-IR) frequencies. The structures were modelled as being embedded in a resonant background. The second example we present is that of silver SRR at near-infrared frequencies infused with metastable helium gas. We have used experimentally obtained parameters for silver [77] in our calculations. All metallic inclusions investigated in this chapter, as well as in subsequent chapters, are considered to be made of silver.

As mentioned earlier, the metamaterial shows magnetic activity for applied radiation polarized with the magnetic field along the (out of plane) SRR axis. The cross-section of the (cylindrical) SRR that we considered in this case is shown in Fig. 3.1. Seventy-five grid points along each direction were used for computing the band structure as well as the reflection and the transmission coefficients. This number is found to be optimum for the unit cell sizes considered as far as the convergence of the results and the restrictions on the number of grid points imposed by the code [101] itself are concerned.

Invariance along the cylindrical axis is assumed. The bare SRR in this case has a magnetic resonance frequency of 74.9 THz. This metamaterial containing a Lorentz-type dielectric within its capacitive gaps is modelled using the following parameters: $f_e = 24.1$ THz, $\omega_e = 74.9$ THz and $\gamma_e = 2.4$THz.

As predicted in the preceding section, it is seen that the negative μ band splits in the presence of the embedding dielectric medium. The frequencies at which the new band gaps are formed are consistent with the predicted values. The mismatch

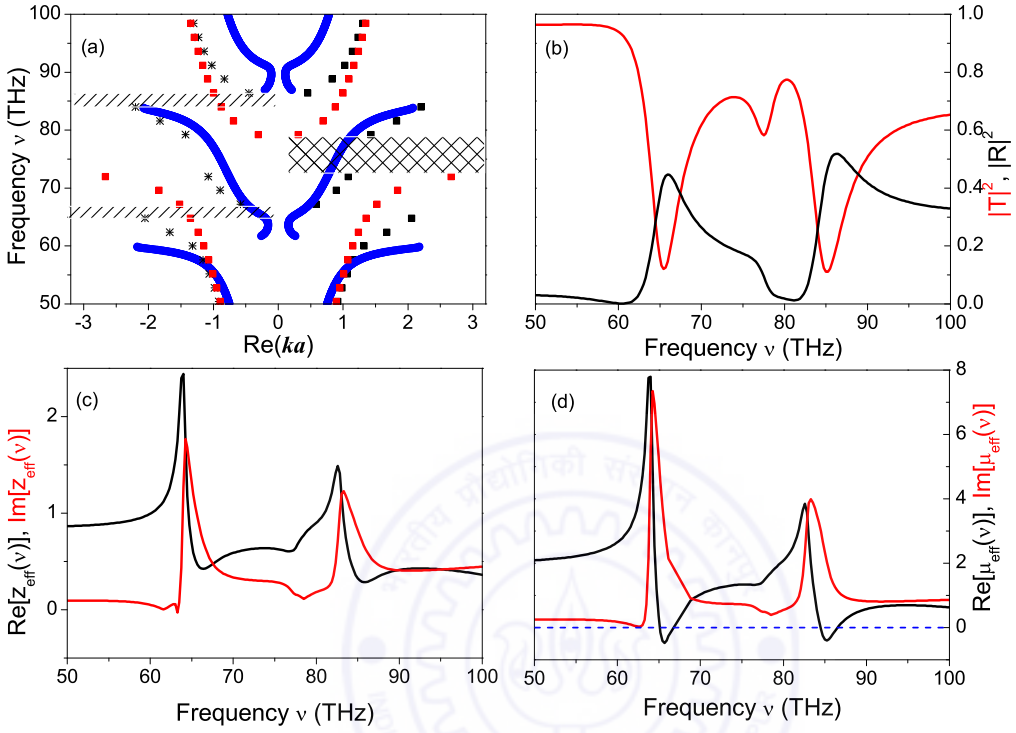

Figure 3.4: (a): The computed band structures for the bare SRR (red circles) and the composite metamaterial embedded in a Raman medium (black squares) under the condition $\omega_e = \omega_m$. The blue lines represent the dispersion predicted by the analytic formula. The band gaps due to $\mu_{\text{eff}} < 0$ are indicated by the cross-hatched region on the right (for the bare SRR whose $\omega_m = 74.9$THz) and the the two hatched regions on the the left (for the band gaps resulting from the inclusion of the resonant Raman medium).
(b): The reflectivity and the transmittivity for a calculated for a slab consisting of a single layer of SRR. Note the presence of two stop bands (low $|T|^2$) corresponding to the band gap frequencies in (a) and the new transmittive band that develops within the original band gap.
(c): The effective impedance $Z(\nu)$ of the composite metamaterial showing the presence of two resonances.
(d): The μ_{eff}, for a slab of the SRR metamaterial with an embedded resonant medium, retrieved using the computed reflection and the transmission coefficients. Note the existence of two frequency ranges where $\mu_{\text{eff}} < 0$. The grey dotted line represents the zero level.

between the results of the TMM calculation and the analytic formula can be attributed to the presence of parasitic capacitances in the SRR. These capacitances, which were neglected in the theoretical model used to describe the functioning of the SRR [44], are automatically taken into account in the TMM simulation.

The results of the band structure calculation and the reflectivity and the transmittivity of the composite medium were compared with the same quantities calculated for a slab consisting of a single layer of the SRR. A new propagating band (further confirmed by a peak in the transmittivity) is found to occur within the stop band region of the bare SRR medium. The frequency intervals corresponding to the new band gaps (regions of high reflectivity and low transmittivity) were found to be consistent with the band structure calculations. To illustrate the splitting of the negative permeability band, the effective material parameters for a slab consisting of four unit cell layers of the SRR-dielectric composite were determined using a retrieval procedure that utilizes the complex reflection and transmission coefficients [34]. Since these SRR are well subwavelength ($a \sim \lambda/10$) at these frequencies, the SRR medium can be thought to constitute an effective medium and it is expected that the metamaterial can be homogenized. The splitting of the negative permeability band is made evident by the large reflectivity at frequencies in the band gap between these bands. This splitting of the negative μ band is found to be consistent with the values predicted by the analytic model (Fig. 3.4 (d)) and also with the simulated band structure as well as the reflectivity and the transmittivity plots. In addition, Fig. 3.4 (c) shows the effective impedance Z(ν) of the metamaterial, with two resonances at the same frequencies as the negative permeability bands, in contrast with the single peak in Z(ν) observed for the bare SRR medium [44] .

Fig. 3.5 illustrates the response of the metamaterial when the dielectric and the magnetic resonances do not coincide, i.e., $\omega_e \neq \omega_m$. The negative permeability band splits as before, but the new resonances are either red-shifted or blue-shifted (with respect to those obtained when $\omega_e = \omega_m$), depending on whether $\omega_e < \omega_m$ or $\omega_e > \omega_m$. A study of the reflection and transmission coefficients for a slab consisting of four unit

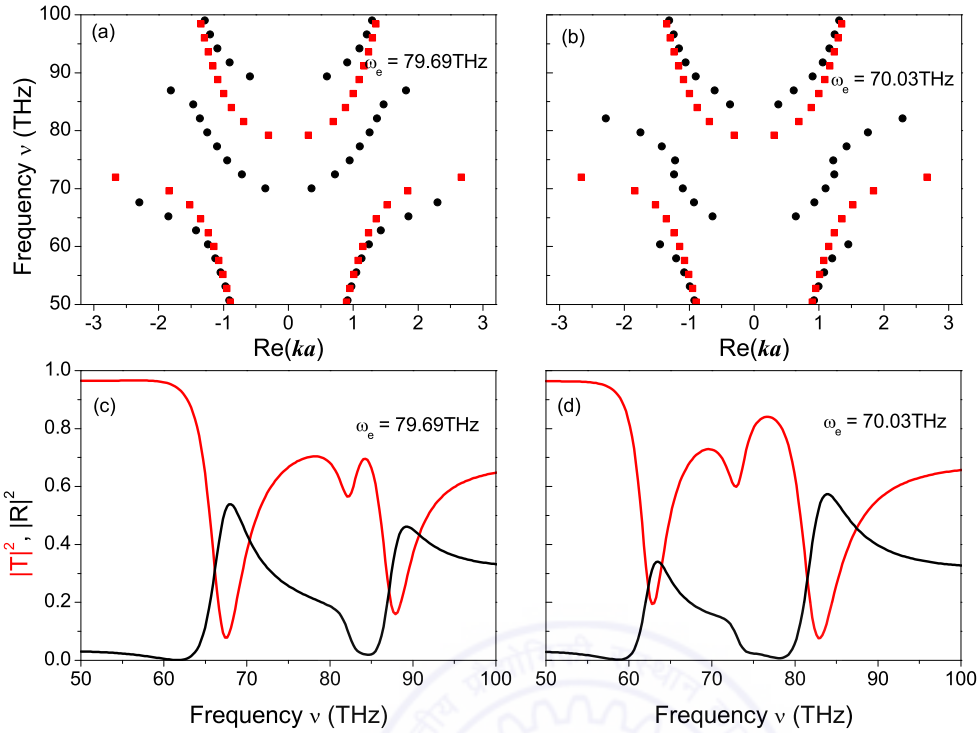

Figure 3.5: The band structures and ($|T|^2$, $|R|^2$) for the composite metamaterial when $\omega_m \neq \omega_e$. (a): Band structure of the composite metamaterial when $\omega_e = 79.69$ THz. The resulting gaps are blue-shifted with respect to those obtained when $\omega_e = \omega_m$.
(b): Band structure of the composite metamaterial when $\omega_e = 70.03$ THz. In this case, the resulting gaps are red-shifted with respect to those obtained when $\omega_e = \omega_m$.
(c) & (d): Reflectivity and transmittivity calculated for a slab consisting of four layers of unit cells. The minima in $|T|^2$ correspond to the new band gaps.

cell layers of the SRR further confirms this behaviour. As seen in the case when $\omega_m = \omega_e$, two regions of enhanced reflectivity (corresponding to the band gaps) separated by a transmittive region (corresponding to the additional propagating band that develops) are observed. For multiple layers, additional peaks due to Fabry-Pérot resonances (arising as a result of multiple scattering) are observed. In each case, the calculated effective impedance ($Z(\nu)$) of the structure (shown in Fig. 3.6) reveals the presence of two peaks, signifying the occurrence of two magnetic resonances. However, the effect of the resonant Lorentz medium weakens considerably when the two resonances are far apart.

In the next section, we describe how appropriately designed metamaterials with SRR structures, embedded in resonant atomic media, can be shown to behave in a similar

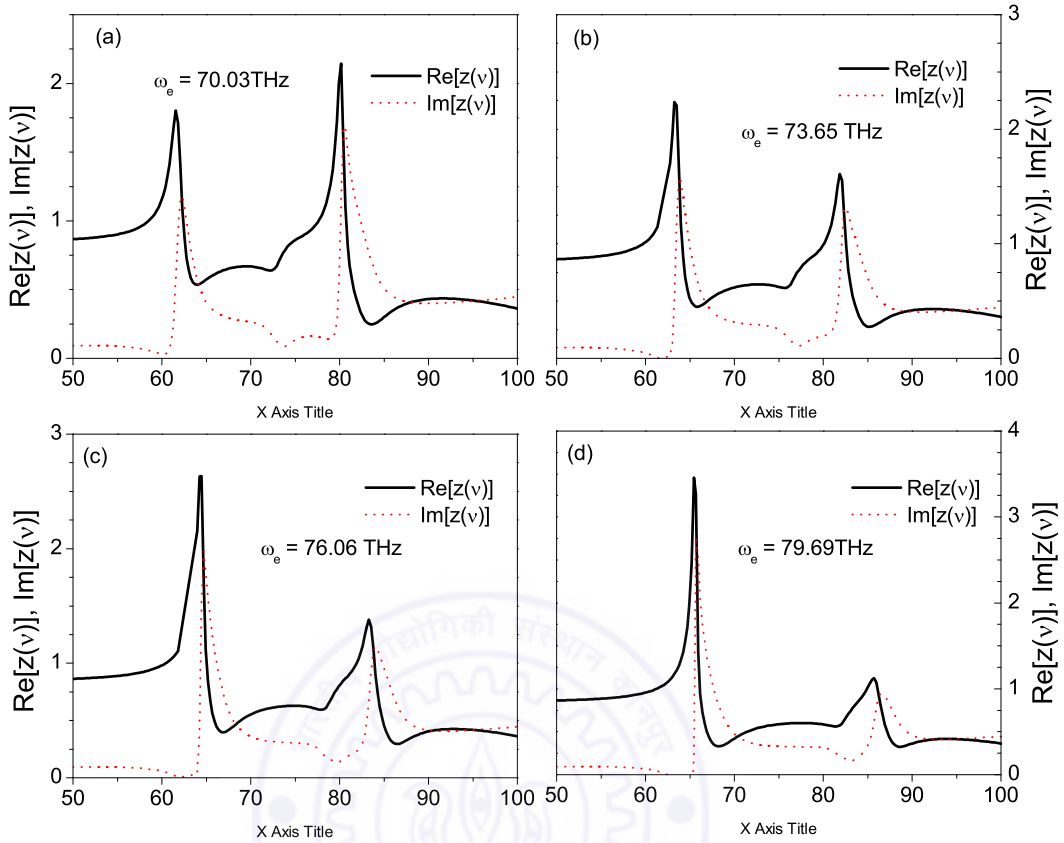

Figure 3.6: (a)-(d) The effective impedance (Z) of the composite metamaterial when the magnetic resonance frequency and the resonance frequency of the dielectric medium are different. The plots of $Z(\nu)$ for the dielectric resonances at 70.03 THz, 73.65 THz, 76.06 THz and 79.69 THz respectively (away from ω_m at 74.9 THz), shows the presence of two peaks, signifying the occurrence of two magnetic resonances.

manner at NIR/optical frequencies [102].

3.3 Simulation of the optical SRR metamaterial

In this section, we demonstrate numerically the coherent control of SRR-based metamaterials at optical (NIR) frequencies. The dimensions and cross-section of the SRR are shown in the right panel of Fig. 3.7. These simulations were also carried out using the PHOTON codes. This SRR metamaterial has a resonant frequency of about 272 THz and a band-gap of about 1.5 THz, corresponding to $\mu < 0$, is obtained above the reso-

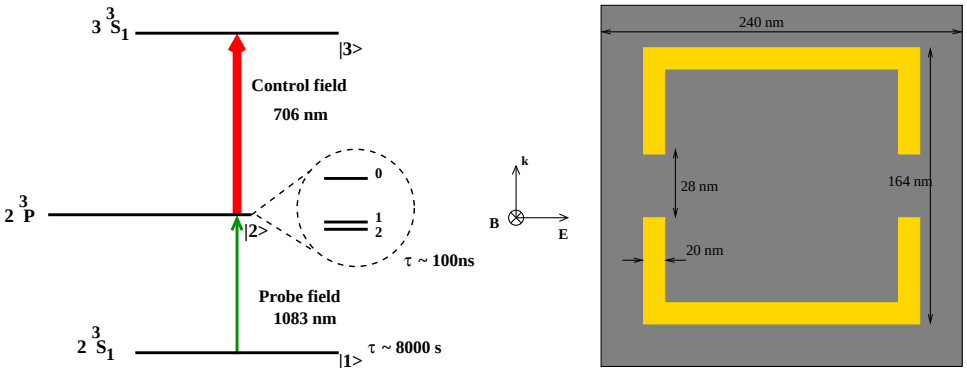

Figure 3.7: Left: The level structure diagram of the relevant levels involved in EIT for metastable helium.
Right: The cross-section and dimensions of the SRR used to demonstrate coherent control of SRR-based metamaterials at NIR and optical frequencies.

nance frequency. A dielectric medium, resonant at frequencies close to this, can now be introduced into this metamaterial in order to investigate how its response is modified. For example, metastable helium has an EIT transition at 276.97 THz, (or $\lambda = 1083$ nm) [103] with the control field applied at 424.75 THz (706 nm) lying in a (higher) pass band. The level structure of the system has been shown in Fig. 3.7. Metastable helium can be produced in an electric discharge and has a long lifetime of about 8000 seconds [104]. After excitation in a discharge it can be introduced into the metamaterial structure by infusing it into an evacuated chamber in which the metamaterial structure has been placed. Paraffin coatings may be utilized to prevent collisional de-excitation of the metastable helium.

Fig. 3.8 (a) and (b) show the modified band structure of this metamaterial. As before, invariance along the SRR (cylindrical) axis is assumed and the calculation is essentially two dimensional. Infusion of metastable helium gas into the metamaterial results in a resonant response and the resultant formation of a band gap as it is equivalent to introducing a Lorentzian resonance at 1083 nm. The band structure of the metamaterial shows the development of additional propagating bands within the bandgap of the bare SRR medium after the infusion of the helium gas into it. In the absence of the control field, there are two broad propagating bands, with a bandgap between 276.958 THz and 276.996 THz, that arise due to the absorptive resonance of the metastable helium. An

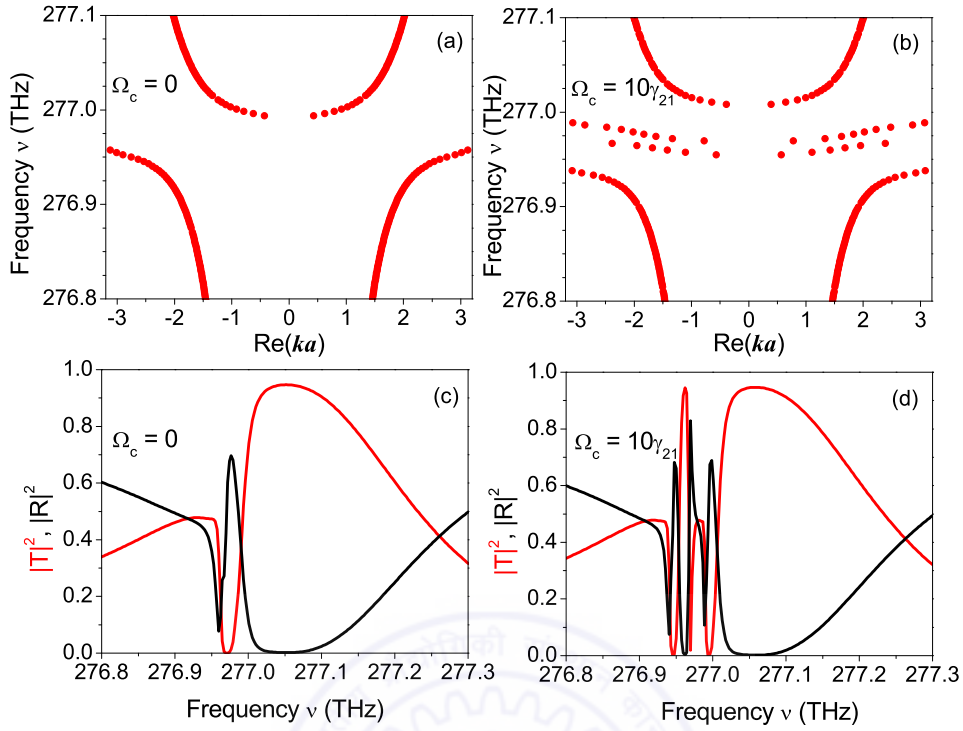

Figure 3.8: Band structure of the SRR metamaterial(unit cell shown) when it is immersed in He gas (a) with the control field switched off and (b) under the action of a control field $\Omega_c = 10\gamma_{21}$.
(c) and (d) represent the reflectivity and the transmittivity of a single-layered slab of the metamaterial under the conditions in (a) and (b) respectively.

additional bandgap arises in the vicinity of the region where $\mathrm{Re}(\varepsilon) \sim 1$ for the embedded material. The application of the control field further splits these bands. Additional flat bands near the EIT line centre are found to develop due to EIT in the embedding medium. Calculations of the reflection and the transmission of the composite media confirm this behaviour (see Fig. 3.8 (c) and (d)).

It is interesting to note that the bandwidths of the band gaps formed and the dispersion of the newly formed formed propagating bands can be controlled by varying the amplitude and the frequency of the control radiation. Thus, blue-shifting the control laser would require a corresponding red-shift in the probe laser in order to satisfy the two-photon resonance condition, $\Delta_1 - \Delta_2 = 0$, where Δ_1 and Δ_2 represent the detunings

of the probe and the control fields, respectively (See Fig. 1.13). This ensures the possibility of aligning the EIT resonance at a desired frequency in/around the band gaps. In Fig 3.8 (c) and (d), we show the reflectivity and the transmittivity of light incident on a slab of SRR medium composed of a single unit cell layer, with and without the EIT control field. Sharp switching of the reflectivity and the transmittivity at specific frequencies that are entirely governed by the control field parameters, are observed. In particular, around 277 THz, the transmittivity drops dramatically from nearly 95% to a few percent within a bandwidth of ∼10 GHz indicating its potential for use as a narrow-band spectral filter.

We note that *non-resonant* rescaling of the capacitance resulting in the tuning of the resonance frequency by upto 20% has been recently demonstrated at about 1THz [92]. However, there are differences between their approach and the present proposal, even though both schemes involve external optical control over the metamaterial response. In their paper, Padilla *et. al* have demonstrated the tuning of the *effective permittivity* of split ring resonators [40, 105, 106] via their resonance frequency by incorporating semiconductors into critical regions of the SRR. Using capacitor plates made out of semiconducting materials, they were able to control the conductivity response and hence, the resonance frequency by means of photoexcitation of charge carriers. Compared to the approach adopted in [93, 107, 108], the capacitance is not shorted out, but results only in a monotonic lowering of the resonance frequency. A tuning range of ~ 20 % was observed. Similarly if the inductance of the SRRs is increased, the resonance frequency increases by around 15% to 40% [92].

In Fig. 3.9, we show the reflectivity and transmittivity for a thicker stack of four layers of SRR metamaterial in the absence and the presence of the control field, in the case of normal incidence. In the absence of the control field, the dispersion of the medium reduces to the Lorentz-type. We remark that the control field parameters used in all these simulations are $\Omega_c = 10\ \gamma_{21} = 24$ GHz (typically experiments use $\Omega_c = \gamma_{21}$ to $\Omega_c = 3\gamma_{21}$). For example, Pavone [103] shows the occurrence of complete transparency at 1083 nm for the $2^3S_1 \rightarrow 2^3P_0$ component, with He pressure 80 mTorr,

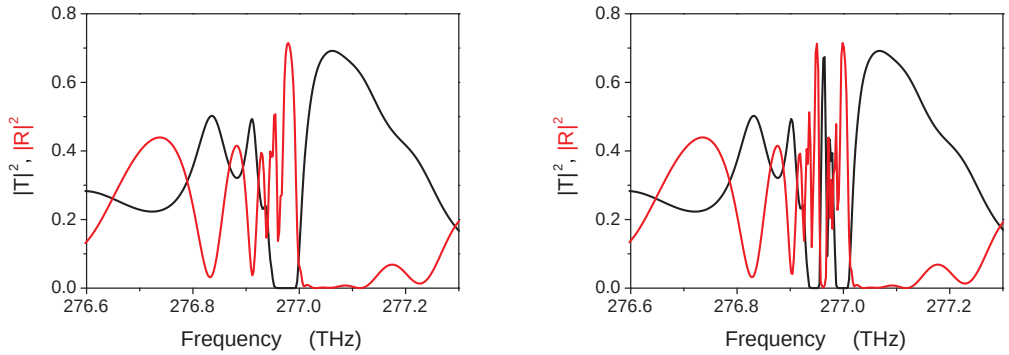

Figure 3.9: The reflectance (Red) and transmittance (black) across four layers of unit cells of SRR metamaterials immersed in metastable helium gas with: (left) zero control field and (right) control field corresponding to $\Omega_c = 10\gamma_{21}$.

discharge current 150 mA, and dressing laser power 350 mW focused with a 400μm beam diameter. In the case of the SRR, due to the large electromagnetic local field enhancements that are possible in the capacitive gaps, this is a very representative value of the control field. The presence of the control field causes narrow transmission resonances to crop up within the bandgap between the two propagating bands. We note that the location and width of the transmission peaks can be shifted in frequency by changing Ω_c via the amplitude or the detuning of the control laser field. Thus, the control field can enable switching the transmission from literally zero to a large value of about 80% at any desired frequency within the bandgap. When multiple layers of unit cells are considered, (four in this case), one can additionally see fine features in the behaviour of the transmission and the reflection. These arise from the Fabry-Pérot resonances of the slab, due to multiple scattering. These coupled with the control via EIT can lead to extremely narrow transmission peaks that suggests the use of such materials as candidates for switchable narrow band filters and cavity tuners in the optics of metamaterials.

Once again, we would like to emphasize that the band-widths of the gaps and the dispersion of the propagating bands formed can all be controlled dynamically by changing the amplitude and the frequency of the control radiation and it is possible to position the EIT line centre at *any* desired location in/near the band gap, as long as the

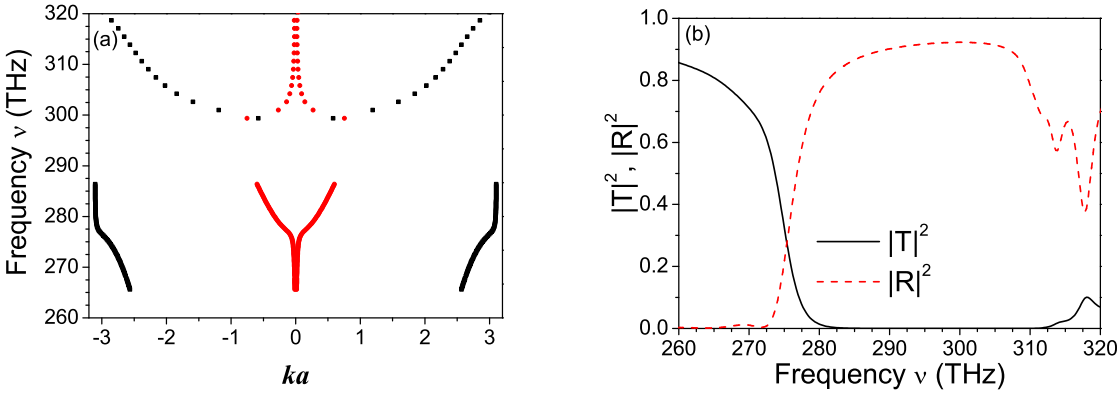

Figure 3.10: (a): The band structure for a metamaterial composed of SRR with similar structural dimensions but with four capacitive gaps. The band gap due to the negative permeability band at 287 THz can be clearly identified.
(b): The reflectance (red) and transmittance (black) across four layers of unit cells of the SRR medium.

two-photon resonance condition is met. However, the effect is more pronounced (wider band-widths are obtained) when the EIT line centre coincides/nearly coincides with the resonance frequency of the bare SRR. Additional calculations carried out with SRR having a magnetic resonance closer to the EIT line center confirm this (Fig. 3.11).

As the EIT resonance approaches the resonance frequency of the bare SRR, the effect of the embedding medium is manifested by the formation of wider band gaps. In Fig. 3.11, we present the band structure and the reflection and transmission coeffcients calculated for a SRR of similar structural parameters with four splits, embedded in a substrate whose $\epsilon_b = 1.6$. In this case, each gap of the SRR is 24nm wide and it has a magnetic resonance at ~ 276.73 THz with a wide band gap of nearly 35 THz (Fig. 3.10). We find that owing to the proximity to the EIT line centre to the magnetic resonance, wider band gaps are obtained both when $\Omega_c = 0$ and when $\Omega_c \neq 0$. This has been shown in Fig. 3.11. In addition, the extra gaps arising near $\mathrm{Re}[\epsilon(\omega)] \sim 1$ are also minimized.

In either situation, the sharp switching of the reflectance and the transmittance occur at specific frequencies that are determined by the parameters of the control field. For example in Fig. 3.8, we find that around 277 THz, there is a dramatic reduction in transmittance from almost 95% to a few percent over a frequency range of approximately

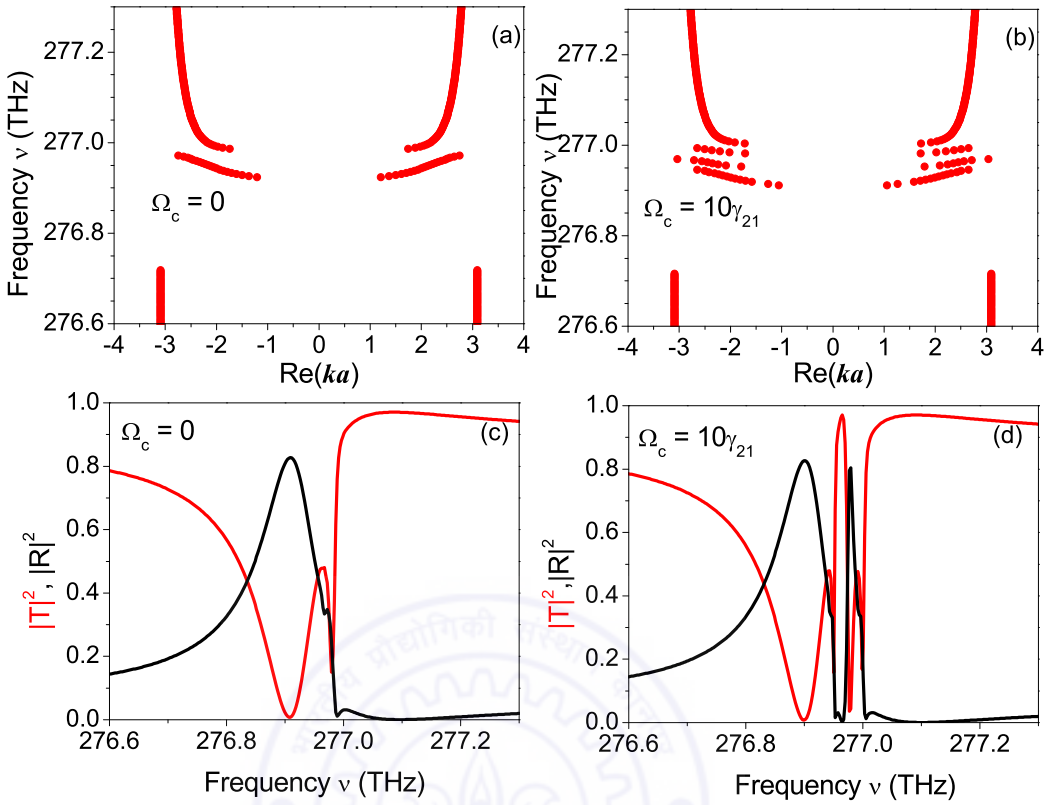

Figure 3.11: Band structure of a metamaterial consisting of SRR having four splits when it is immersed in He gas (a) with the control field switched off and (b) under the action of a control field $\Omega_c = 10\gamma_{21}$. (c) and (d) represent the reflectivity and the transmittivity of a single-layered slab of the metamaterial under the conditions specified in (a) and (b) respectively.

10 GHz. Such dramatic changes in the transmission properties highlight its potential for extremely narrow-band switching applications.

The following points are to be noted. First of all, we have assumed that the EIT effect is itself not hampered by the metamaterial. This assumption is justified as we have chosen the EIT control field to lie within a propagating band and well within the first Brillouin zone, hence the control field would be expected to be uniform across the medium. It is also expected that the introduction of the metastable atomic gas within the metamaterial structure will not affect the atomic decay rates significantly. Second, we have not attempted to homogenize this structure since it is only slightly less

than a quarter of the free space wavelength. At length scales such as this, the effective medium parameters are considerably influenced by the electric field of the incident radiation. Thus, in view of this, only the photonic bandstructure and transmission/reflection properties of this metamaterial (such as those presented in Fig. 3.8 and elsewhere) have been used to characterize the nature of their electromagnetic response. However, it is to be noted that the impedance ($Z(\nu)$) calculated (but not shown here) for this composite metamaterial continues to have a multiple-peaked nature characteristic of the splitting of the magnetic resonance.

3.4 Robustness of the control scheme

Although it is often seen that light interacting with mesoscopic metallic structures experience much higher dissipation than the bulk metal itself, we have found that our results remain unaffected even if the intrinsic dissipation of the metal (silver, in this case) is increased. This was verified by calculating the response of the composite metamaterial after artificially increasing the dissipation in the metal by two, two and a half and three times. In each case, the response of the system did not change significantly, as illustrated by Fig. 3.12.

There is another aspect of these structures that needs to be taken into account. The resonance frequency of these metamaterials depends crucially on the accuracy with which they can be fabricated. Thus, in practice, each metamaterial unit will be different from the rest due to the inevitable inaccuracies that come up during fabrication, leading to a distribution of resonance frequencies rather than a single resonance frequency. It is possible that the consequent broadening of the magnetic resonance could wipe out the narrow band effects predicted. Fortunately, the switching and control effects were found to be rather robust against such inhomogeneous broadening.

The effects of disorder were modelled by taking into consideration the different resonance frequencies of the SRRs arising from imperfections in fabrication. Typically, this would result in a random distribution of resonance frequencies. We consider the

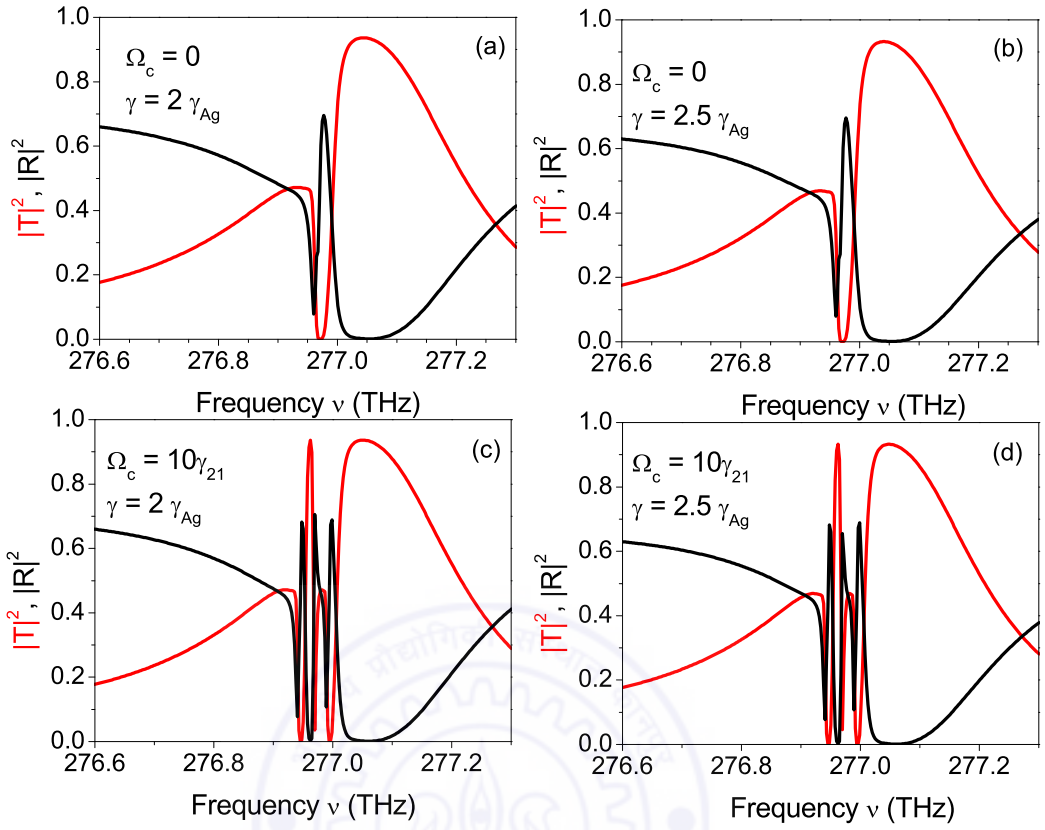

Figure 3.12: The reflectivity and the transmittivity for the composite medium when the dissipation in the silver SRR is increased: (a) and (c): two times, (b) and (d): two and a half times.

distribution of magnetic resonance frequencies arising due to structural imperfections to be normally distributed (Gaussian) about the mean frequency ω_m. For example, the effect of broadening on the response of a metamaterial consisting of 'bare' SRRs will be given by

$$\mu_{\text{bare}}(\omega) = \frac{1}{\sqrt{\pi\sigma^2}} \int_{-\infty}^{\infty} \mu_{\text{bare}}(\omega', \omega) \exp - \left(\frac{\omega' - \omega_m}{\sigma} \right)^2 d\omega', \tag{3.13}$$

where ω' is the magnetic resonance frequency of individual SRRs (which may assume all possible values) and ω_m is the desired magnetic resonance frequency. The width of this distribution (σ) is indicative of the extent of the imperfect structuring. Thus, the effective permeability of the medium is found to broaden, as shown in Fig. 3.13

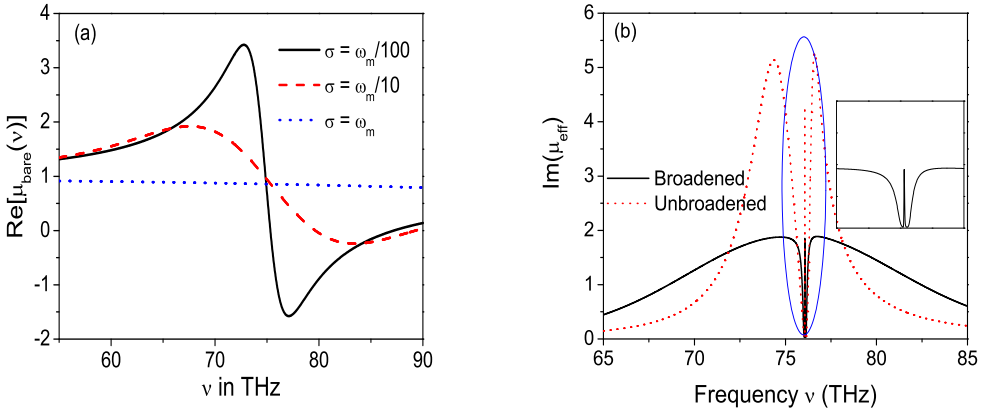

Figure 3.13: (a): The effective permeability of the metamaterial for different widths of the distribution of the magnetic resonance frequency. The resonant $\mu_{\rm eff}$ is washed out when the imperfections lead to $\sigma \sim \omega_m$.
(b): The broadened Im($\mu_{\rm eff}$) of the metamaterial in the presence of a background medium which exhibits EIT, for $\sigma = \omega_m/100$. The inset shows the details of the central part of the figure where the narrow features are seen to survive inspite of the broadening of the overall response.

(a). Adopting a similar procedure for the other quantities and averaging over this distribution, the following expressions were obtained:

$$\langle \omega_{\rm eff}^2 \rangle = \omega_{\rm eff}^2 + \frac{\epsilon_R \sigma^2}{\epsilon_R^2 + \epsilon_I^2} \tag{3.14}$$

$$\langle \Gamma_{\rm eff} \rangle = \Gamma_{\rm eff} + \frac{\epsilon_I \sigma^2}{\epsilon_R^2 + \epsilon_I^2} \tag{3.15}$$

$$\langle f_{\rm eff} \rangle = f_{\rm eff} \tag{3.16}$$

The effective filling fraction ($f_{\rm eff}$) remains unaltered as it is independent of ω_m.

For values of $\sigma \sim \Gamma_m$, we find that the narrow band effects arising due to the presence of $\epsilon(\omega)$ survive (See Fig. 3.13 (b)). While the strength of the resonance decreases on the whole due to the larger $\Gamma_{\rm eff}$, the regions of reduced absorption between the resonances remain nearly unaltered. The 'increased' filling fraction that remains unaffected by the inhomogeneous broadening compensates for the effect of the imperfections. In other words, the few resonant SRR units exhibit a large enough absorption cross-section such that the reduced number of participating SRRs due to the inhomogeneous broadening does not adversely affect the response on an average. Although accuracy in fabrication

still remains an important issue, we note that the controllable effects discussed here are robust and generic to many metamaterials that depend upon resonances for their electromagnetic properties.

Similar schemes for controlling the response of wire-like metamaterials that rely on plasmonic resonances for their dielectric or magnetic response is also possible. This has been discussed at length in the next chapter (Chap. 4). Collections of silver or gold nanorods can be accurately fabricated with little size dispersion and consequently such metamaterials will be less prone to the effects of inhomogeneous broadening.

3.5 Conclusion

Thus, we have demonstrated here a new paradigm for the parametric control of metamaterials. The metamaterial response is completely transformed by incorporating coherently controllable resonant media into the design. This is marked by the occurrence of multiple magnetic resonances and the consequent splitting of the negative permeability band, accompanied by a redefinition of the filling fraction and the dissipation in the SRR medium. The presence of the resonant dielectric background converts both these parameters into frequency-dispersive quantities whose behaviours closely follow the resonant nature of the dielectric. This results in a sharp increase in the effective filling fraction near resonance of the dielectric. This has been attributed to the large cross-section of the SRR at the resonance (of the order of the incident wavelength itself). Γ_{eff} may also assume sub-classical values around the same frequencies, owing to the 'freezing' of currents in the SRR, even though the original SRR medium, as well as the embedding dielectric are both dissipative. These effects have been studied for a variety of background media such as dielectric media that have a Lorentz permittivity as well as media that display Electromagnetically Induced Transparency. Our results provide a new mechanism for reducing the dissipation inherent to metamaterials, which has been the main hindrance thus far in developing applications.

The splitting of the negative-μ band of the SRR medium was verified by numerical

simulations at mid-IR and NIR frequencies. The numerical simulations of homogenizable SRR media in the presence of a dispersive Lorentz permittivty at mid-IR frequencies yields negative permeability bands over two frequency ranges, confirming the occurrence of two magnetic resonances in place of the earlier single magnetic resonance. Similar calculations at NIR frequencies with the SRR medium infused with metastable He gas, in which EIT occurs close to the resonance frequency of the bare SRR medium, reveals the occurrence of multiple transmission bands within the frequency regime spanned by the original band gap. The frequencies and the widths of these bands may be controlled via the strength of the EIT control field, highlighting the possibility of utilizing of such metamaterials for developing switchable filters. The control scheme presented here is also quite robust, both against the enhanced levels of dissipation associated with mesoscopic metallic structures, as well the inhomogeneous broadening of the magnetic resonance due to structural imperfections. Both these effects have the potential have the potential to wipe out the narrow band effects predicted. However, our calculations show that the narrow band effects survive, largely due to the increased f_{eff} at resonance that nullifies the effects of structural defects of the SRRs.

Despite the control scheme being inherently dispersive, it results in a completely tunable metamaterial that can be used effectively for a variety of narrow band applications. The robustness of this scheme towards structural imperfections and the fact that the modified response obtained is generic to all resonant metamaterials only increases its usefulness. It also highlights the possibility of developing controllable *and* reconfigurable metamaterials, the reconfigurability in this case being implemented by choosing a slightly different resonance frequency for the (gaseous) background medium. Therefore, our results bring together two powerful, yet very different ideas of metamaterials and coherent control phenomena to manipulate the electromagnetic response of such composite materials.

Chapter 4

Coherently Controlling Plasmonic Metamaterials at Optical Frequencies

The magnetic response of metamaterials, particularly the (SRR-based) metamaterials, has been theoretically studied extensively at low frequencies (long wavelengths) when effective medium theories are valid. At these frequencies, the medium can be described in terms of the effective material parameters ϵ_{eff} and μ_{eff} as noted earlier in Chap. 1. Experimentally, many of the metamaterials realized are not truly homogenizable with the unit cell sizes ranging from $\lambda/20$ to $\lambda/4$ [109], even at terahertz and mid-IR frequencies.

At higher frequencies, notably from the near-IR upwards, even designing metamaterials that behave as true effective media becomes a challenging proposition. It is indeed a very difficult task to design metamaterials that have resonances at optical freqencies, but it is nevertheless possible [110]. The possibility of inducing magnetic activity in optical metamaterials has led to vigorous activity by researchers in this field. Several approaches to this end have been proposed. These include metal nanoclusters [111, 112, 113, 114], high permittivity inclusions [115], pairs of plasmonic particles [116, 117, 78], fishnet structures [118, 119], etc. However, these metamaterials can have their own drawbacks, such as significant losses as well as having anisotropic and polarization sensitive re-

sponses owing to asymmetries in their geometric structure. Further, the size of many of these structures can be a significant fraction of the operating wavelength, which affects the purity of their magnetic response owing to quadrupolar electric contributions as well as photonic band structure effects.

Another approach towards generating an effective magnetic response at optical frequencies using sub-wavelength inclusions is based on the idea of the collective resonance of an array of plasmonic nanoparticles arranged to form a single, subwavelength loop inclusion [120, 121]. Unlike the SRR, where the conduction currents give rise to the magnetic dipole moment, the origin of the effective magnetic response of the plasmonic loop is somewhat different. In this case, instead, the plasmonic resonance of individual particles plays a dominant role by effectively inducing a circulating 'displacement' current around the loop. Unlike conventional metallic loops or the SRR, the size of the loop inclusion does not have a great impact upon the resonance frequency of the induced magnetic dipole moment. The plasmonic resonance frequency of the nanoparticles plays a decisive role in the occurrence of the magnetic response. Plasmonic metamaterials exhibiting a magnetic response can possess certain advantages over the conventional SRR. First of all, they may be fabricated with greater ease using-self assembly methods. Second, they can be designed to operate resonantly at optical frequencies while still remaining fairly subwavelength in size. The usual SRR-based magnetic metamaterials are severely limited by the breakdown of effective medium theories at higher frequencies, particularly optical frequencies, as shown in Chap. 2.

4.1 The magnetic response of plasmonic metamaterials: theory

The nature and the origin of the plasmonic resonances of small particles has been discussed in Section 1.4.2. The schematic diagram of the plasmonic metamaterial with a net magnetic response [120] has been shown in Fig. 4.1. N number of plasmonic nanopar-

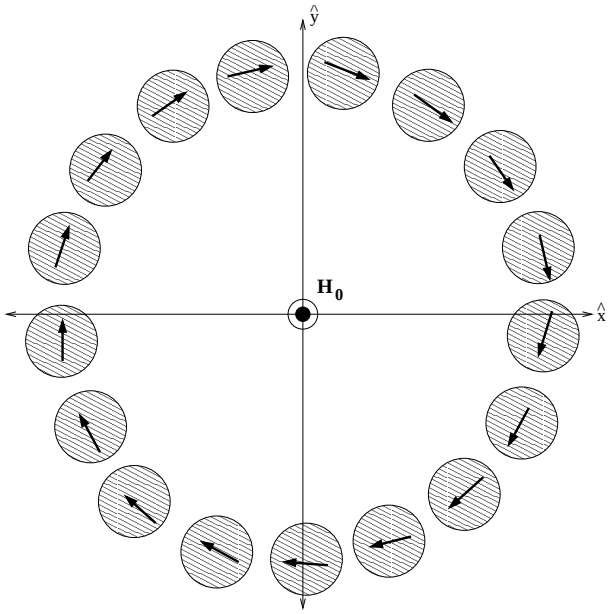

Figure 4.1: Schematic representation of the plasmonic metamaterial proposed by Engheta *et. al.* in *Opt. Exp.*, **14**, 1557 (2006). The shaded circles represent the nanospheres and the black arrows indicate the electric dipole moment induced on each particle. A circulating 'displacement' current is generated leading to a magnetic resonance.

ticles (embedded in a background dielectric whose permittivity is ϵ_b) are arranged on the circumference of a circular loop of radius R. Here we consider spherical nanoparticles which have an isotropic response due to their symmetry, but in principle particles of arbitrary shape will have a similar response, albeit with a different resonance frequency, and may be used for this analysis. The loop is well subwavelength, i.e., $R \ll \lambda_b$, where λ_b is the wavelength of radiation in the background medium. The centre of the loop is assumed to be the origin of a Cartesian system of co-ordinates. Evidently, the position of the particles may be defined by the vectors

$$\mathbf{r_j} \equiv [R\cos(2\pi j/N), R\sin(2\pi j/N), 0], \qquad (j = 1, \cdots N). \tag{4.1}$$

This plasmonic metamaterial is assumed to be excited by a monochromatic and harmonic wave whose magnetic field is oriented along the normal to the loop (z) as shown in Fig. 4.1. Under the influence of the exciting magnetic field, circulating dipole moments are induced on each particle as a consequence of Faraday's law. Owing to the symmetry of the system and the excitation, the electric dipoles induced over the par-

ticles are directed along $\hat{\phi}$, as indicated by the black arrows in the figure. A detailed analysis [121] leads to the following results. First, any configuration with three or more identical nanoparticles displaced symmetrically around the origin shows a net zero electric dipole moment in response to a uniform magnetic excitation. A pair of metal plates has also been shown to have a zero electric dipole moment and a net magnetic moment. However, the electric quadrupole moment is non-negligible and is of the same order as the magnetic dipole moment. The higher the number of particles, the greater the number of electric multipoles cancelled. Thus, its response is 'impure' as compared to the response of this metamaterial. Next, the magnetic dipole moment associated with the loop is

$$\mathbf{m_H} = \frac{-i\omega pNR}{2}\hat{z}, \tag{4.2}$$

for each plasmonic particle represented by an effective dipole moment $\mathbf{p} = p\hat{\phi}$ and a current density $\mathbf{J} = -i\omega p \sum_{j=0}^{N-1} \hat{\phi}(\mathbf{r_j})\delta(\mathbf{r} - \mathbf{r_j})$. Thus, as the number of particles in the loop becomes large, the magnitude of the electric multipoles become negligible and for a sufficiently small loop, the magnetic dipole moment alone dominates the electromagnetic response. The effective relative magnetic permeability of the metamaterial consisting of such plasmonic loop units is given by the expression [121]

$$\mu_{\text{eff}} = 1 + \frac{1}{N_d^{-1}\left[\alpha_m^{-1} + i(k_b^3/6\pi) - 1/3\right]}, \tag{4.3}$$

where N_d is the number density of loop inclusions, α_m is the magnetic polarizability (as defined in Ref. [121]) and k_b is the wave vector in the background dielectric medium. The magnetic resonance occurs when the condition

$$\text{Re}\left[\alpha_m^{-1}\right] = 0 \tag{4.4}$$

is satisfied. This itself depends on the electric polarizability and occurs near the resonance frequency of each nanoparticle, but is slightly shifted due to the coupling between them. It is important to note that the permeability includes a radiation loss factor [122],

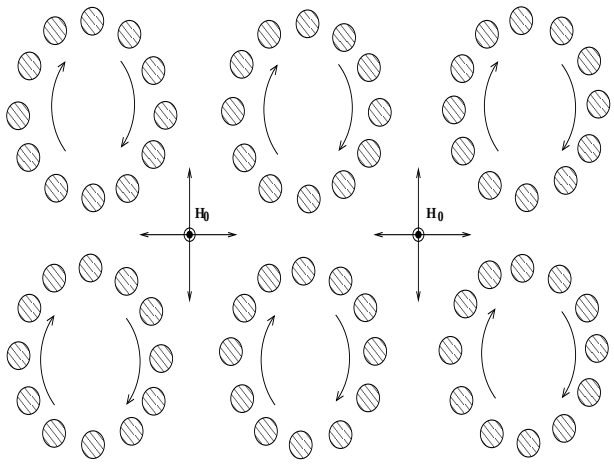

Figure 4.2: Schematic diagram of a metamaterial consisting of an array of plasmonic loop inclusions. Such an array may also be embedded in a host dielectric medium. The direction of the induced currents has been indicated by curved arrows.

even if the particles themselves are lossless. As long as the loop radius satisfies $R \ll \lambda$, many such loops may be embedded in a host medium (Fig. 4.2) to produce a homogeneous metamaterial with resonant magnetic properties at optical frequencies. In addition, the effect of the Ohmic losses of each particle on the effective loss in the loop can be shown to be reduced by a factor of N [121].

This approach can be applied to various types of plasmonic particles. The plasmonic resonances of metallic nanoparticles (of gold and silver) lie in the visible region of the electromagnetic spectrum and they have been used for *ornamental* purposes (such as in stained-glass windows) for hundreds of years. Metallic nanoparticles are thus ideal candidates which may be incorporated into the scheme just described for generating a magnetic response at optical frequencies. In the next section, we describe the magnetic response at optical frequencies of a metamaterial consisting of plasmonic loops of silver nanorods and control schemes for manipulating it.

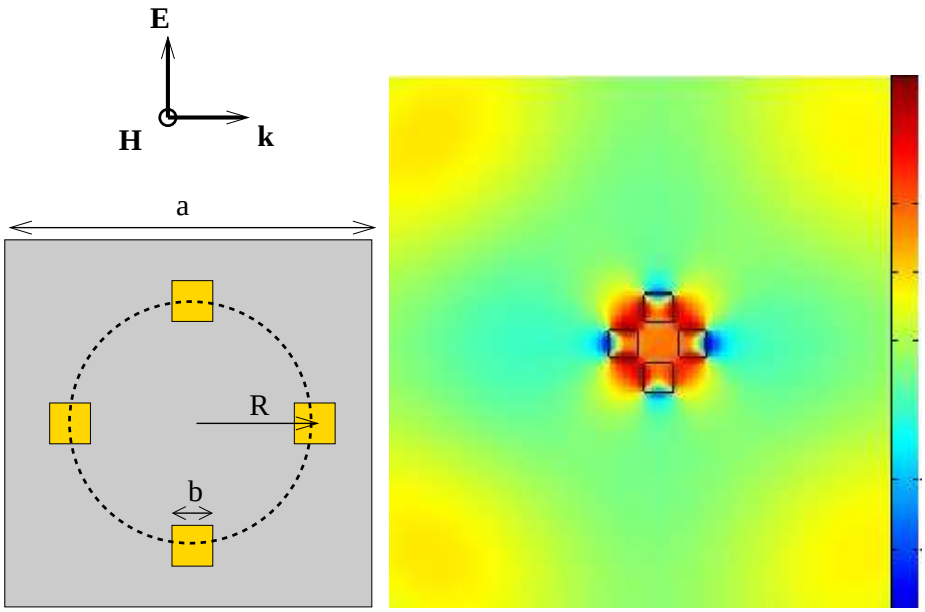

Figure 4.3: (a): A cross-sectional view of a typical unit cell of the plasmonic loop metamaterial, showing the nanorods placed on the circumference of a circle. In the figure, $a = 120$ nm, $b = 25$ nm and $R = 26$ nm.
(b): The magnetic response of an isolated loop inclusion illustrating the concentration of the magnetic field inside the loop at resonance, when excited by means of a line source. The magnetic resonance of this single, isolated loop inclusion was found to occur at 652 THz.

4.2 Numerical calculations of the response of a plasmonic nanorod metamaterial

In this section, we discuss the response and the control of a metamaterial consisting of loop inclusions composed of plasmonic nanorods. Arrays of small resonant plasmonic spheres arranged on subwavelength-sized loops have been shown to exhibit a magnetic response in Ref. [120]. Plasmonic resonances of inclusions of metallic (silver) nanorods arranged on the circumference of a circle (Fig. 4.3 (a)) are considered here. The magnetic field of the incident radiation is assumed to be oriented along the axis of the rods and the problem becomes essentially two-dimensional. As discussed earlier, the loop exhibits a magnetic resonance that stems from an interaction driven by the individual plasmonic resonance of each nanorod. Each resonant nanoparticle induces a circulating *displacement* current around this loop and the electric dipole moments (perpendicular to the axis) align along the circumference of the ring when driven at the plasmon resonance

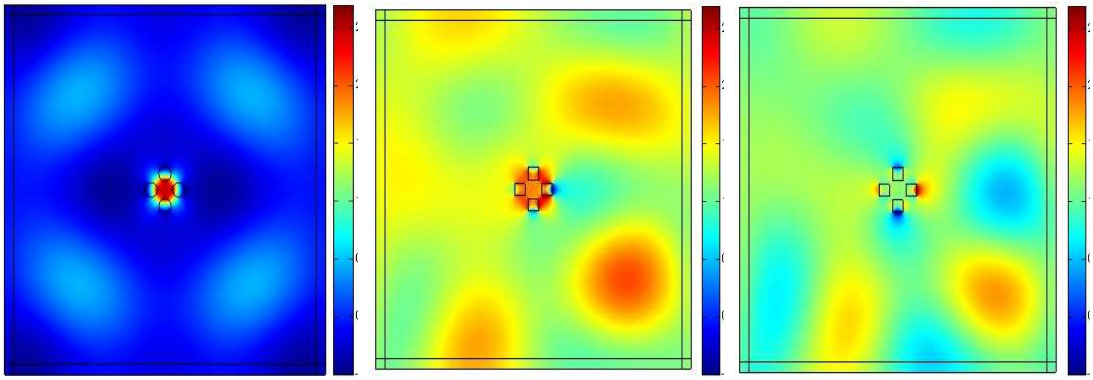

Figure 4.4: Left: A single plasmonic loop inclusion consisting of circular nanorods at its magnetic resonance, showing the magnetic field strongly concentrated inside the loop. Four point sources are located at four corners around the loop inclusion. The radius of the loop is $R = 26$ nm, the diameter of the circular nanorod is 25 nm and each side of the unit cell is $a = 120$ nm. The magnetic resonance occurs at 650 THz.
Middle: A single plasmonic loop inclusion made up of square nanorods at its magnetic resonance frequency (652 THz) with a single point source placed outside at the lower right-hand corner. The magnetic field is confined within the loop.
Right: The single plasmonic loop inclusion at a frequency of 667 THz (above its magnetic resonance frequency). A single point source is placed outside the loop at the lower right-hand corner. No confinement of the magnetic field inside the loop can be observed. The dimensions of the loop, the nanorods and the unit cell in the middle and the right panels are the same as those in Fig. 4.3.

frequency. This is confirmed by our COMSOL^{TM} finite elements numerical simulations (Fig. 4.3 (b)) where an enormous confined magnetic field appears in the interior of the loop at resonance, when a single loop inclusion is driven by an external source. Although plasmonic resonances of nanoparticles are usually strongly shape-dependent, in this case making the cross-section of the nanorods square does not seem to affect the nature of the magnetic resonance greatly. This was confirmed by COMSOL^{TM} simulations for nanorods of square and circular cross-sections, whereby similar resonance frequencies were obtained as long as the side of the square (b) was roughly equal to the diameter of the nanorods. Fig. 4.4 illustrates the behaviour of a single isolated loop inclusion. The left panel shows the strongly confined magnetic field within a loop inclusion consisting of nanorods with a circular cross-section, while the middle and the right panels illustrate the response of a loop inclusion of square nanorods, at and above its resonance frequency respectively. From the right panel, it is evident that no confinement of the magnetic field within the loop occurs away from the resonance frequency.

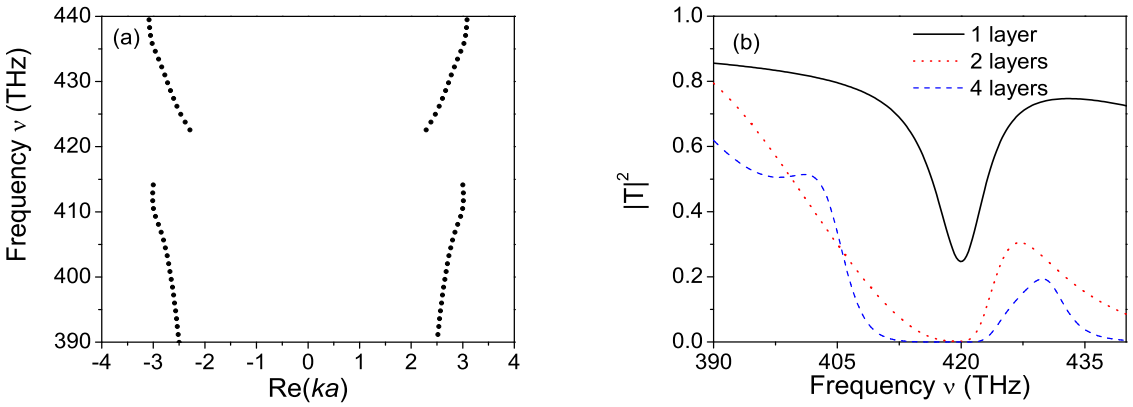

Figure 4.5: (a) The band structure and (b), the transmittivity for four layers of unit cells of the plasmonic metamaterial. The additional peaks are the Fabry-Pérot resonances occuring due to multiple scattering between the interface of the medium and vacuum.

As expected, it was found that the size of the loop does not strongly influence the frequency of the individual magnetic resonance and the plasmonic resonance frequency of each nanoparticle primarily determines the resonant behaviour of the loop. However, the number of plasmonic particles on the loop determines the strength of the resonance, as expected [120]. At resonance, the size of each unit cell is ($a \sim \lambda/5$). Further, each loop inclusion is much smaller compared to the wavelength of the incident light ($R \sim \lambda/28$). Thus, Bragg scattering will not play a dominant role in the observed phenomenon and the system can be homogenized.

The photonic band structure of an array of such plasmonic loops of long silver nanorods was calculated using the PHOTON codes. The calculations become essentially two dimensional with the cylindrical axis being the axis of invariance. To avoid staircasing effects with a square numerical grid, we considered rods with square cross-sections rather than circular ones. The unit cell is a square with side $a = 150$ nm (See Fig. 4.3 (a)). Within each unit cell of the metamaterial, four silver nanorods (of square cross-section and side $b = 25$ nm), embedded in a background dielectric medium with $\epsilon_b = 2.65$, are symmetrically arranged on the circumference of a circle of radius R = 26 nm. The metamaterial exhibits a distinctly identifiable magnetic resonance at $\sim$ 415 THz (722 nm), with a negative magnetic permeability band gap up to $\sim$ 421 THz (712 nm) as shown in Fig. 4.5 (a). This behaviour is also confirmed by the transmittivity for

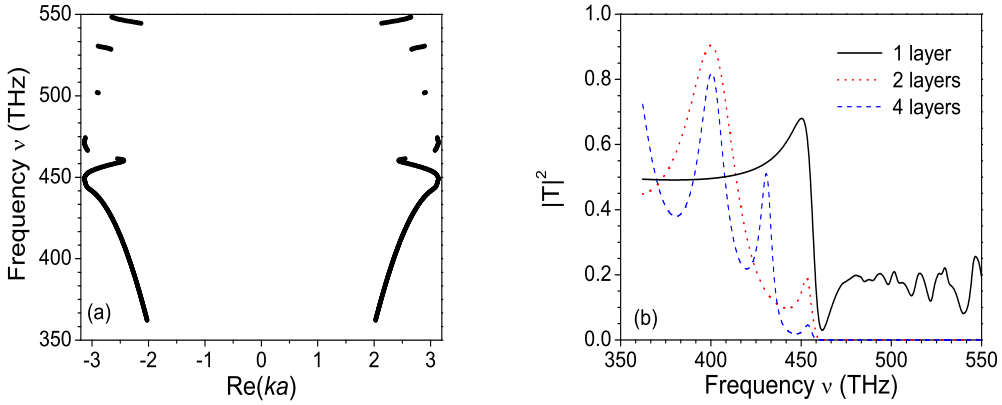

Figure 4.6: (a) The band structure and (b), the transmittivity for four layers of unit cells of the plasmonic metamaterial when the unit cell size is reduced and the loop radius increased, keeping the cross-sectional size of the nanorods constant . As before, the additional peaks are the Fabry-Pérot resonances occuring due to multiple scattering between the interface of the medium and vacuum.

a slab composed of four layers of unit cells (loops) (Fig. 4.5 (b)), where a region of low transmittivity and high reflectivity is observed between the same frequencies.

It is observed that the resonance frequency of the metamaterial differs from that for individual loop inclusions due to coupling between the nanoparticles making up the different loops. For smaller unit cell sizes and larger loop radii, the coupling of the fields between neighbouring plasmonic loops leads to the hybridization of resonances. Many weak resonances are found to occur close together and identification of the magnetic resonance leading to the negative permeability band gap, is extremely difficult. For example, reducing the unit cell size to 120 nm and increasing R of the loop to 30 nm (keeping b constant) results in the formation of a very large region interspersed with numerous small flat bands (Fig. 4.6), very different from Fig. 4.5, even though the underlying structure of the metamaterial is not changed drastically. The difference between the response of the two systems is further highlighted by their reflectivity and the transmittivity for different layer thicknesses. A comparison with Fig. 4.5 (b) shows the stark differences between the two. In Fig. 4.6, the identification of the negative permeability band gap is difficult. The transmittivity drops from nearly 70% to a few percent around ~ 450 THz and does not rise significantly thereafter. A number of smaller bands

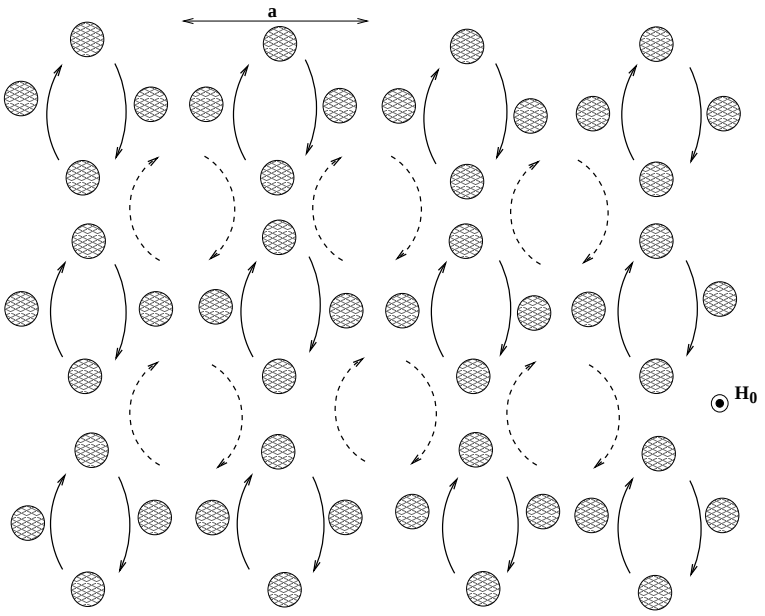

Figure 4.7: Schematic representation of the plasmonic metamaterial consisting of four rods per unit cell showing the alternative pathways by means of which plasmonic loops may be formed. Such loops may support weaker secondary magnetic resonances leading to difficulties in identifying the primary magnetic resonance due to the rods in the unit cell.

where the transmittivity does not exceed 20% are formed (Fig. 4.6 (b)). This behaviour may be compared with the magneto-inductive (MI) waves described by Shamonina and Solymar [123, 124]. They investigated the waves supported by capacitively loaded loops using a circuit model in which each loop is coupled magnetically to a number of other loops. The coupling between the loops may lead to the occurrence of a large number of resonances in an infinite (axially coupled) linear array. If all the loops lie on the same horizontal array, much of the results obtained by Shamonina *et. al.* for the axial array hold true. The loops are still mutually coupled, but the mutual inductance is negative. The dispersion curve for such a system shows backward waves in which the phase and the group velocities are oppositely directed.

Here, we have a similar phenomenon. Each plasmonic loop can be described in terms of the capacitances between nanoparticles and their inductance. However, if the loop inclusions are close together, nanoparticles of one loop may couple capacitively with nanoparticles in adjacent loops (see Fig. 4.7) and form alternate pathways for supporting a magnetic resonance. In addition, adjacent loops may be coupled leading

to the formation of multiple resonances.

4.3 Control scheme for the plasmonic metamaterial

The plasmonic resonance of a metallic nanoparticle is highly sensitive to the dielectric permittivity of the surrounding media (ϵ_b). In the case of a cylindrical nanoparticle, the localized surface plasmon resonance occurs when the condition

$$\mathrm{Re}[\epsilon_b + \epsilon_m] = 0, \tag{4.5}$$

is satisfied [52]. Using a Drude form for the permittivity of the metal (ϵ_m), the plasmon resonance frequency of a metallic cylinder may be written as:

$$\omega_r = \omega_p \left[\frac{1}{\epsilon_b + \epsilon_\infty} - \frac{\gamma^2}{\omega_p^2} \right]^{1/2} \tag{4.6}$$

where ω_r is the plasmon resonance frequency for the nanoparticle, ω_p and γ define the bulk plasma frequency and the bulk dissipation of the metal, while ϵ_∞ is its 'static' permittivity. Hence, even a small change in ϵ_b can shift the plasmon resonance frequency of the nanorod and by extension, the magnetic loop resonance frequency arising out of the circulating displacement current around the loop. For example, if $\epsilon_b \rightarrow \epsilon_b + \delta$, leading to a shift in the resonance frequency from $\omega_r \rightarrow \omega_r^{'}$, we have

$$\omega_r^2 - \omega_r^{'2} = \frac{\omega_p^2 \delta^2}{\epsilon_b + \epsilon_\infty}. \tag{4.7}$$

A subtle difference between the SRR and the plasmonic metamaterial that may affect the efficiency with which their magnetic response is manipulated is to be noted. In the case of the SRR, the electric fields and the displacement currents are highly confined to the region within the capacitive gaps of the SRR. In this case of the plasmonic particle loops, however, the displacement current is between adjacent nanoparticles, and is more spatially delocalized. A more closely packed loop would, in principle, enable a higher

degree of localization of the fields and the currents and make possible a stronger resonant response.

It is proposed to effect control over the magnetic resonance via the Inverse Raman Effect in CS_2, which gives rise to a permittivity having an absorptive Lorentz lineshape. As already described in Sec. 1.5.4, the Inverse Raman Effect in CS_2 refers to the absorption of a probe field at an anti-Stokes ($\nu_0 + \nu_R$) frequency when a strong pump laser at a frequency ν_0 is applied. The energy difference between the ground and the excited levels in CS_2 is 656cm^{-1} or 19.68 THz, and the probe beam is strongly attenuated at a correspondingly higher frequency. Other substances like a-Si, which also exhibit the Inverse Raman Effect [125] can also be used for such purposes. However, a liquid like CS_2, can be easily infiltrated into the metamaterial, while incorporating a solid medium like a-Si into the loop inclusions would need to be carried out at the stage of fabrication itself.

4.3.1 Controlling the magnetic response

Control of ϵ_b by an applied electromagnetic radiation is the key to the present scheme for controllling composite metamaterial itself. In order to demonstrate parametric control over the magnetic resonance, an atomic/molecular system exhibiting a resonance in the neighbourhood of the band gap frequency is essential. Raman transitions that provide such resonances can be effectively used in a very flexible manner because the Raman resonance frequency can be easily tuned by the choice of the pump laser frequency. We present the calculated results for such a stimulated Raman absorption process (Fig. 1.16) at 416.54 THz in CS_2 with ground state vibrational level spacing of 656 cm^{-1} (19.68 THz). Experimentally obtained values for the parameters of CS_2 [126] were used, corresponding to the non-resonant $\chi^{(3)}$ response. We use peak pump powers of the order of 100 GW/cm^2 and a typical linewidth of 0.5 cm^{-1} (15 GHz). Our estimates for the nonlinearity are overtly conservative as the resonant Raman process would be expected to enhance the $\chi^{(3)}$ response. The inverse Raman absorption of about -15dB has been reported in amorphous silicon with much lower pump powers of about 10 GW/cm^2 [125].

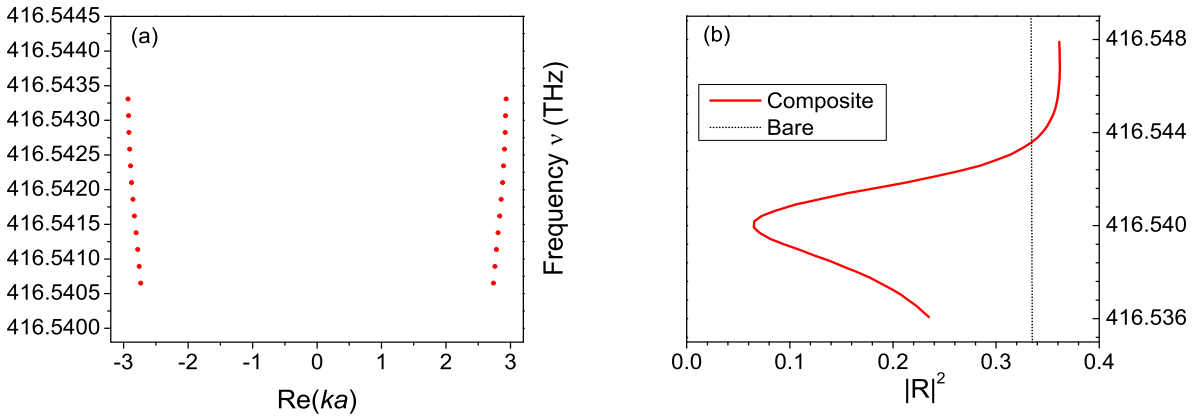

Figure 4.8: (a) & (b) The new band formed and the modified reflectivity of the plasmonic metamaterial in the neighbourhood of a Raman transition in CS_2 at 416.54 THz. The band gap of the original metamaterial occurred between $\sim$ 415 THz and 420 THz, as seen in Fig. 4.5.

Our calculations were performed assuming a pump laser field at 396.86 THz which lies within the propagating band of the metamaterial (Fig. 4.5(a)).

A new propagating band develops within the band gap region seen in Fig. 4.5, The region where this new propagating band is formed has been expanded in Fig. 4.8. The formation of a (dissipative) propagating band is manifested by a sharp drop of ($\sim$ 20%) in the reflectivity of the medium. The transmittivity of the composite metamaterial is reasonable when compared to that for the 'bare' metamaterial, but is completely overshadowed by the large change in the reflectivity. The new band formed is quite dissipative and this prevents a large change in the transmittivity in comparison with the change in reflectivity. While it is possible to numerically demonstrate dramatic enhancement of the transmittivity by several orders of magnitude by using higher pump intensities, a resonantly enhanced nonlinear coefficient will significantly improve the response of the composite metamaterial. Thus, the effect of the introduction of the resonant Raman medium results in a sharp reduction in the reflectivity of the composite metamaterial over a narrow frequency band ($\sim$ 5 GHz). The linewidth of the Raman pump laser dictates the linewidth of the induced absorption, which in turn determines the change in the reflectivity. The number of propagating bands that are formed are also strongly dependent on the resonant nature of the background medium. For example,

in the case of EIT, the permittivity of the medium is resonant at frequencies $\omega_1 \pm \Omega_c/2$ about the EIT line center ω_1 under the influence of the control field Ω_c. Thus, by incorporating a dielectric material that can be rendered transparent electromagnetically into the metamaterial, the effective permittivity can be driven to positive values over *two* frequency ranges. Thus, additional propagating bands will be formed in the transmittivity spectrum of the composite metamaterial under the action of the control field (when EIT is observed) as compared to those formed when the control field is turned off (Lorentz dispersion). In the case of EIT-based control, the additional bands formed in the presence of a control field Ω_c [102] switch rapidly between states of high and low transmission and this behaviour may be controlled by varying Ω_c.

4.4 Dilute plasma-like behaviour

In this section, the response of a periodic array of parallel metallic nanorods with sub-wavelength periodicity is considered when the electric field of the radiation is parallel to the nanorods. This state of polarization of light is orthogonal to that considered in the previous section. The medium effectively behaves like a plasma at optical and near infra-red (NIR) frequencies for the radiation with the electric field aligned along the rods as shown in Fig. 4.9. When embedded in an appropriate resonant medium, the plasma-like response of this metamaterial can be switched and a transmission band opens up below the cut-off (plasma) frequency. Resonant processes such as EIT may be used to further tailor the properties of this transmission band.

The use of sparse, conducting sub-wavelength thin wire meshes for generating a low frequency anisotropic plasma-like response was first proposed by Pendry *et. al.* [38]. Such a response arises due to (i) a lowered effective electron density (N_{eff}) as the conducting medium is sparse, and (ii) an enhanced effective electronic mass (m_{eff}) due to the large inductance of the thin wires. The resulting effective plasma frequency $\omega_p^2 = (N_{eff}e^2)/(\epsilon_0 m_{eff})$ can range from a few gigahertz to a hundred terahertz depending on the geometry. The use of such metallic wire meshes as effective anisotropic

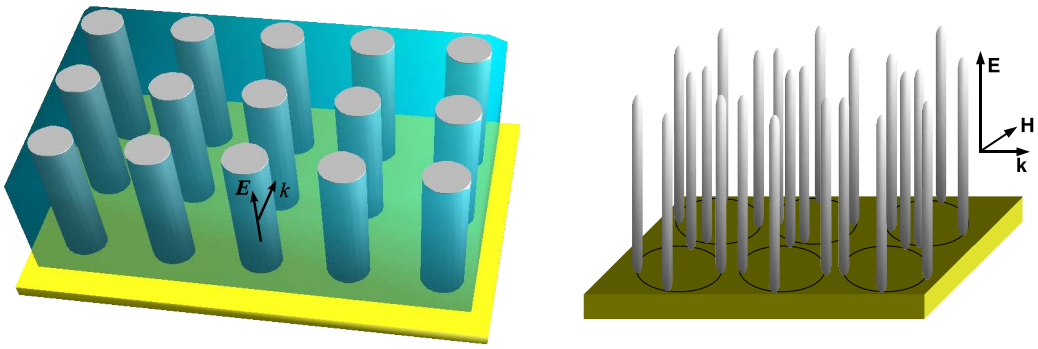

Figure 4.9: Schematic pictures of an aligned nanorod array with subwavelength periodicity and grown vertically on a substrate that behaves as a plasma for linearly polarized radiation with the electric field along the wire axes. Left: The nanorods are arranged regularly in rows.
Right: The nanorods lie on the circumference of a circular loop, just like the plasmonic metamaterial described earlier in this chapter, except that they respond to the electric field of the incident radiation.

low-frequency plasma has been experimentally demonstrated for light at normal incidence [12]. At optical and NIR frequencies, however, most bulk metals behave dominantly as plasmas rather than as Ohmic conductors. As the electromagnetic fields penetrate well into the metal wires, any effects arising due to the enhanced effective mass become less pronounced and the plasma frequency begins to depend only on the volume fraction occupied by the metal (defined as the filling fraction, f, in this section). This behaviour as a dilute metal is confirmed by the band structures shown in Fig. 4.10 (a) for an array of silver nanorods such as the ones shown in Fig. 4.9. A higher metallic filling fraction results in a larger plasma frequency ($\mathrm{Re}(\epsilon_{\mathrm{eff}}) > 0$ for $\omega > \omega_p$ in Fig. 4.10 (a)).

Arrays of metal nanorods comprise one of the simplest optical metamaterials that display plasma-like behaviour and there exist several techniques for their manufacture. Large scale ordered and aligned silver nanowire arrays can be obtained, for example, by pulsed electrodeposition in porous alumina [127]. Alternatively, vertically aligned columnar silver nanorods as schematically suggested in Fig. 4.9, have been grown on substrates using glancing angle e-beam deposition [128].

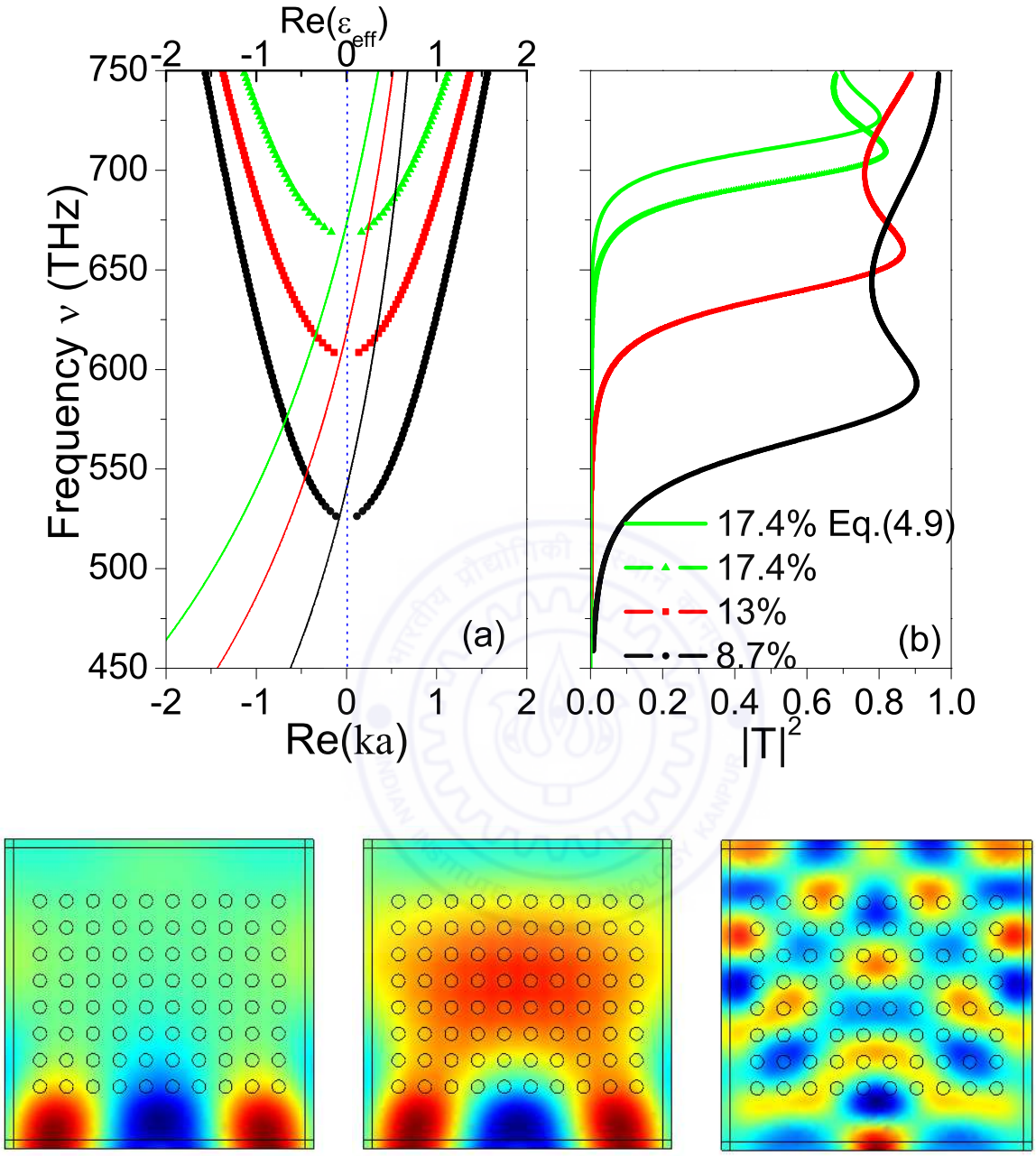

Figure 4.10: Top panels: (a) Band structure of the silver nanorod metamaterial and (b) Transmittance from an array containing four layers of nanorods, for various filling fractions of silver calculated using the transfer matrix method. The $\mathrm{Re}(\epsilon_{\mathrm{eff}})$ and transmittance calculated for a homogeneous slab of effective medium as given by Eq. (4.9) are also shown by thin lines in (a) and (b) respectively.
Bottom panels: The electric fields (in arbitrary units) within the rod array for a plane wave incident from the bottom. Left: $\omega < \omega_p$, Middle: $\omega = \omega_p$, Right: $\omega > \omega_p$ The radiation does not penetrate for frequencies below the plasma frequency ($\omega_p = 650$ THz) while it propagates across for higher frequencies. Each nanorod has a diameter of 25 nm and the unit cell size is 120 nm.

For a 'homogeneous' metamaterial, the waves propagating within the medium defined by an effective permittivity can be represented as a set of plane electromagnetic waves. Averaging over a macroscopically small, but microscopically large region of space, the averaged electric displacement can be expressed in terms of the averaged electric fields as:

$$\langle D_\alpha \rangle = \epsilon^{\text{eff}}_{\alpha\beta} \langle E_\beta \rangle, \tag{4.8}$$

where the Greek indices correspond to the Cartesian components [129]. Since ϵ_m and ϵ_b are both isotropic quantities, the permittivity tensor is diagonal, $\epsilon^{\text{eff}}_{\alpha\beta} = \delta_{\alpha\beta}\epsilon^{\text{eff}}_{\beta\beta}$. The effective dielectric permittivity of the *dilute metal*, for radiation with the electric field along the nanorods (z direction), is given by

$$\epsilon^{\text{eff}}_{zz} = f\epsilon_{\text{m}} + (1-f)\epsilon_{\text{b}} \tag{4.9}$$

Here, the filling fraction $f = \pi r^2/a^2$, where r is the radius of the circular rods and a is the periodicity of the square lattice, ϵ_{m} and ϵ_{b} are the dielectric permittivities of the metal and the nonconducting background medium, respectively. The effective plasma frequency (ω_p) of the metamaterial is obtained by the condition $\epsilon_{\text{eff}} = 0$. It is seen in Fig. 4.10 (a) that propagating modes arise only when $\text{Re}(\epsilon_{\text{eff}}) > 0$, and in Fig. 4.10 (b) that $\text{Re}(\epsilon_{\text{eff}})$ given by Eq. 4.9 reproduces the transmittance through a slab of two layers of silver nanorods with reasonable accuracy.

This agreement assumes significance in view of the ongoing debate on the nature and applicability of homogenization theories to such thin-wire metamaterials at optical frequencies [130, 131, 132]. Lakhtakia and Mackay have argued that the Maxwell-Garnet and the Bruggeman formalisms yield physically plausible results only if the real parts of the permittivities of the constituent materials have the same sign. In their opinion, if the real parts of the permittivities are of opposite signs, there are considerable differences between the two. Using the system studied by Bratkovsky *et. al.*, they have numerically shown that for metallic filling fractions ~ 6 %, there are significant differences between the results of the two formalisms. The results presented here using the Eq. 4.9 based

on the Maxwell-Garnet theory as well the full-wave calculations using the TMM are consistent, for much higher filling fractions ($\sim$ 17%). Thus, inspite of the real parts of the constituent materials (silver and a background dielectric) have permittivities of opposite signs, the simple theory has been shown to describe the system quite effectively. The explanation presented here contradicts the conclusions reached in [130] that the high reflectivity is a consequence of the skin effect. The results show conclusively that the medium behaves like an effective plasma below a certain plasma frequency determined by the filling fraction of the metal, where it reflects most of the incident radiation, while above the plasma frequency it is highly transmittive. The field maps calculated by the COMSOL^{TM} software based on the finite elements method with perfectly matched boundary layers confirm the plasma-like behaviour where there is very little penetration within the rod arrays below ω_p, while the fields are transmitted across the nanorod array above ω_p (see Fig. 4.10, bottom panels). It is to be noted however, that Eq. (4.9) appears to indicate a filling fraction which is somewhat higher than that estimated by the simulations. This can be understood if one realizes that the full-wave solutions properly take into account the incomplete penetration of the electric fields into the metal, and hence, would equivalently imply a lowered filling fraction. (The waves decay into the bulk of the metal.)

Limits upto which TMM results match Eq. 4.9: We have used a very simple model to describe the effective permittivity of the dilute plasma. While no significant differences are expected between the metamaterial response predicted by Eq. 4.9 and the TMM calculations at low f, the scenario is likely to change as f increases. We find that the mismatch in the effective plasma frequency between Eq. 4.9 and the TMM calculations persist for even higher filling fractions. Both the TMM calculations as well as the equation continue to predict higher plasma frequencies as f is increased. This is found to continue for filling fractions upto 50% of the unit cell. However, the mismatch increases at filling fractions of about $\sim$ 25 % and worsens thereafter. Evidently, at such concentrations, the formula fails as the exact field distributions in the metamaterial becomes progressively more and more complex. This also matches with the fact that

the MG effective medium approach is consistent for $f \sim 0.3 - 0.5$, as already mentioned in Chap. 1.

4.5 Switching a dilute plasma-like metamaterial

Usually $\mathrm{Re}(\epsilon_\mathrm{m})$ is a negative number with a large magnitude at optical and NIR frequencies. A small filling fraction of the metal is therefore sufficient to render $\epsilon_\mathrm{eff} < 0$, as can be deduced from Eq. 4.9. If the embedding medium, however, had a resonance below the effective plasma frequency, the resonant enhancement of the $\mathrm{Re}(\epsilon_\mathrm{b})$ in the positive regime could offset the negative contribution of the metal. The metamaterial as a whole would then act as a positive dielectric medium and display a transmission band at frequencies within the width of the resonance below the resonance frequency. This new transmission band occurs below the plasma frequency of the bare plasma metamaterial. It is, indeed, counter-intuitive that introduction of a lossy resonance can induce the medium to be more transmittive.

Resonant enhancement of the positive permittivity of the background material can be achieved by various means including Raman transitions, simple resonant absorption and coherent processes like EIT. We consider here a specific and realistic case of silver nanorods submerged in a background of atomic sodium gas that is readily accomplished by placing the nanorod array within a vacuum cell infused with sodium vapor. For the frequencies of the $\mathrm{D}_1 - \mathrm{D}_2$ lines of sodium, we construct a *dilute metal* (nanorod array) with a plasma frequency $\omega_p > \omega_{D1,\ D2}$. A filling fraction of $f = 0.174$ is used, for which we consider a metamaterial with four square silver nanorods (side $b = 25$ nm) in a square unit cell of $a = 120$ nm (to avoid staircasing effects of circular rods on a square computational grid). It is estimated that one can achieve a maximum of $\epsilon_\mathrm{b} \sim 2.2$ near the resonance for pressure broadened sodium with a number density of $\sim 1 \times 10^{17}\mathrm{cm}^{-3}$ [133]. Using such a background medium, our formula predicts a maximum of $\epsilon_\mathrm{eff} \sim 0.86$, leading to a positive dielectric permittivity band below ω_p.

Alternative proposals for the creation of a transmission band below the plasma fre-

quency, but for homogeneous plasmas exist in the literature. These include proposals by Harris [134] and Agarwal and Boyd [133]. Harris has proposed the use of processes analogous to EIT in atoms for driving longitudinal plasma oscillations in an ideal plasma, leading to a pass band below the plasma cut-off. Two electromagnetic fields whose frequency difference is close to the plasma frequency are used to drive a longitudinal plasma oscillation. The plasma opposes the current density produced by each field when it acts by itself. However, when the two fields are applied together, a passband may be created below cut-off. The process uses the collective excitation of the medium to establish transparency, rather than atomic processes.

Agarwal and Boyd have proposed the elimination of the negative dielectric band gap in a resonant homogeneous optical medium by EIT effects with a strong control field. However, their proposal differs from the usual EIT in the sense that they seek to eliminate the region of negative permittivity in $\mathrm{Re}(\epsilon(\omega))$ where the associated $\mathrm{Im}(\epsilon)(\omega)$ is small. Their approach takes into account the local field effects such as the dipole-dipole interactions in the medium and they have shown that the negative permittivity band gap in alkali metal vapours can be removed by a strong control field using the example of sodium vapour. However, it may be noted that alkali metal vapours are not the ideal media for observing this effect due to self-broadening effects [133]. Our proposal, however, uses a metamaterial whose underlying structure is inhomogeneous.

We now present numerical solutions obtained using the Transfer Matrix Method [75] for a plasma metamaterial consisting of silver nanorods immersed in a background vapour of sodium. The calculations are essentially two-dimensional within the plane perpendicular to the axes of the cylinders. We have used experimentally determined values for the dielectric permittivity of silver [77] and the sodium vapour [135] in our calculations. In Fig. 4.11, new propagating bands which develop below the effective plasma frequency ($\sim$ 650 THz), in the presence of the resonant sodium vapour, are shown. Fig. 4.11 (a) and (c) show the band structure for the composite plasma metamaterial while Fig. 4.11 (b) and (d) show the transmittivity and the reflectivity from a slab of four layers of this metamaterial. Narrow transmission bands are found to develop

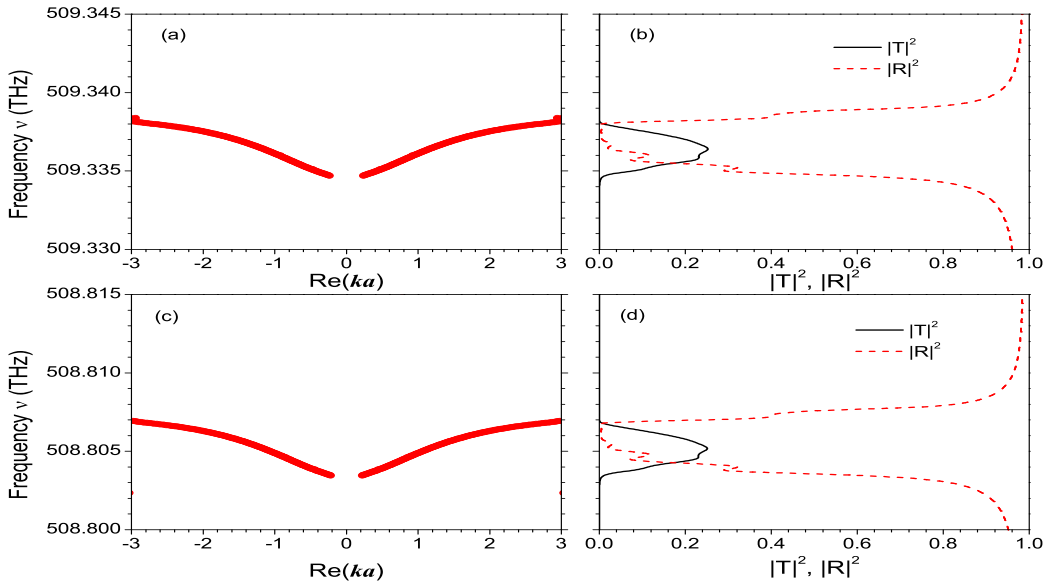

Figure 4.11: (a) and (c): Band structure for s-polarized light with the metamaterial immersed in atomic sodium showing the new transmission band that develops below ω_p, for the D_1 and D_2 lines respectively.
(b) and (d): The transmittivity corresponding to the band structure in (a) and (c) respectively.

at $\sim$ 508.805 THz and 509.335 THz corresponding to the frequencies of the D_1 and D_2 lines of sodium respectively.

The application of another control radiation field can dramatically transform the dielectric response and the dispersion of the sodium lines through the occurrence of coherent processes like EIT. The control field for EIT, that either propagates along the nanorod axis or co-propagates with the probe field but with the magnetic field oriented along the nanorod axis, can be readily applied in the scheme Fig. 4.9. The application of an appropriate control field with a Rabi frequency $\Omega_c = 10\gamma$ is shown to tune and switch the transmittive bands of the D_1 or the D_2 lines in Fig. 4.12 (a) and Fig. 4.12 (b).

A similar effect can be demonstrated by introducing atomic barium vapour (which exhibits EIT) into the array. The results of this numerical simulation have been presented in Fig. 4.13. New propagating bands are formed below the effective plasma

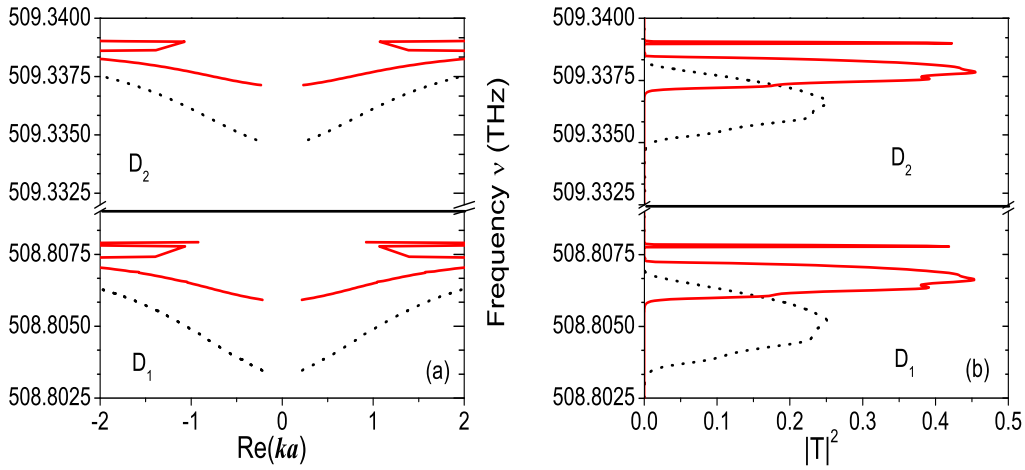

Figure 4.12: (a): Band structure for s-polarized light with the metamaterial immersed in atomic sodium showing the new transmission band that develops below ω_p, for the D_1 and D_2 lines respectively. An additional switchable band develops under the action of a control field.
(b): The transmittivity corresponding to the band structure in (a).

frequency, as before and the strength of the EIT control field may be used as a parameter for switching the transmittive bands. The intensity of the control field is used as a control parameter to switch the transmission. For example, the additional propagating band may be 'turned off' by reducing the control field strength to zero. We find that the observed effects are reasonably independent of the exact location and distribution of the nanorods in the unit cell, as long as the filling fraction remains unaltered. We also note that plasma-like metallic metamaterials with even larger filling fractions can be also switched using a coherently enhanced refractive index for the background atomic gas [65]. The refractive index of a metallic vapour (for example, rubidium [136]) may be enhanced, with very low dissipation, by means of quantum coherence effects. Finally and crucially, we also would point out that the present proposal for switching the plasma metamaterial depends on making the effective permittivity positive through a bulk volume averaging process. The effectiveness of this method depends on whether the positive permittivity of the resonantly enhanced background is able to counteract the negative permittivity of the metallic part. Thus, for higher metallic filling fractions, considerable resonant enhancement of the permittivity of the background dielectric medium

will be necessary to generate an overall positive permittivity over frequency ranges lying below the effective plasma frequency of the metamaterial. This is very different from the previous work [102] on parametrically transforming the resonances of the metamaterial units via coherent processes. The difference lies in the fact that in the former case, the resonant magnetic response of the metamaterial is itself transformed by the effect of a resonant background dielectric, along with a modified metallic filling fraction and dissipation of the metamaterial. The results presented in this section, on the other hand, do not involve any metamaterial resonances.

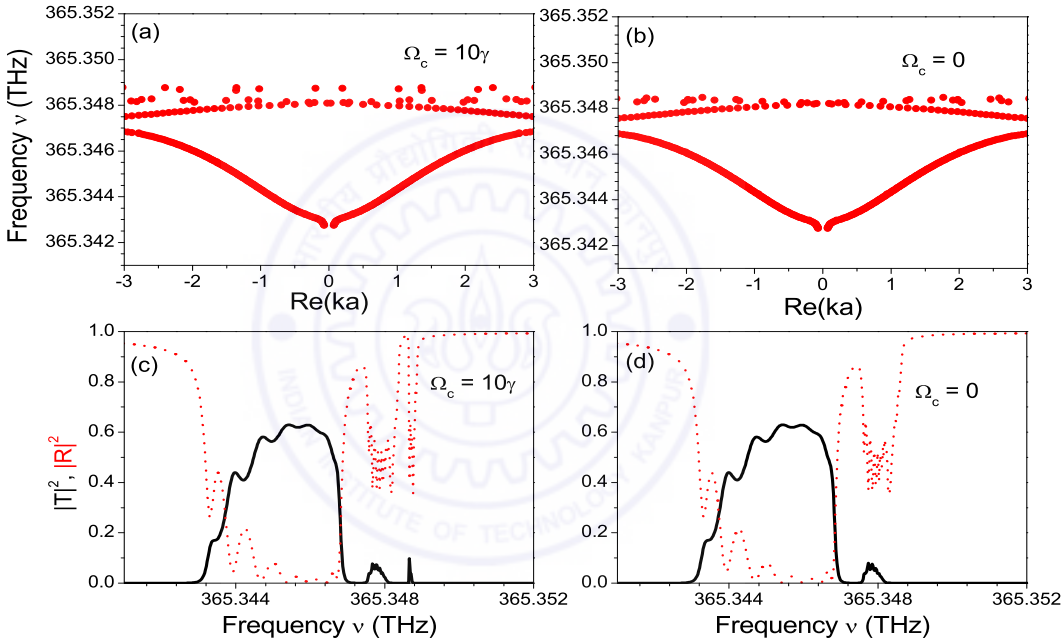

Figure 4.13: (a) and (b): Band structure for s-polarized light with the metamaterial immersed in barium vapour showing the new transmission band that develops below ω_p, for the in the presence and in the absence of the control field, respectively.
(c) and (d): The transmittivity and the reflectivity corresponding to the band structures shown in (a) and (b) respectively.

4.6 Conclusion

To summarize, we have studied the response of an array of silver nanorods when exposed to both light of both the states of polarizations: first, when the magnetic field is per-

pendicular to the plane of incidence and second, when the electric field is perpendicular to the plane of incidence. We have shown that one may obtain a magnetic resonance for loop inclusions consisting of these nanorods in the case of light whose magnetic field is perpendicular to the plane of incidence and oriented along the rod axes. We also note the possibility of hybridization of the magnetic resonance due to the interaction between adjacent loops. The magnetic resonance may be manipulated by embedding the loops in a suitable resonant background dielectric medium via Raman processes or EIT. One observes the resultant splitting of the magnetic resonance and the formation of (dissipative) bands within the region of the former negative permeability band gap. For light of the other state of polarization, when the electric field is aligned along the rod axes, the metamaterial behaves like an anisotropic effective plasma whose plasma frequency is determined by the filling fraction of metal within the unit cell. This response is independent of the arrangement of the nanorods within the unit cell for a particular filling fraction, as illustrated by the band structures in Fig. 4.14. It is possible to make the effective plasma transmit radiation at frequencies that lie below its effective plasma frequency by means of the resonantly enhanced permittivity of suitable dielectric media. The resonant response of the positive permittivity of such a background medium can be sufficient to cancel out the negative permittivity of the dilute plasma leading to a net positive effective medium permittivity. In this chapter, we have numerically demonstrated the possibility of introducing a propagating band below the plasma frequency by coherent optical processes such as EIT in the composite metallic nanorod array with a resonant atomic background. Other quantum interference-based mechanisms for generating a low loss enhanced refractive index, as proposed by Scully, may also be used, specially for nanorod metamaterials with larger filling fractions.

The effects which have been numerically demonstrated in this chapter may also be possible using nanorod-quantum dot composite metamaterials. In particular, quantum dots with gain (rather than absorption) may be used to compensate for the losses in the metamaterial. Bratkovsky *et. al.* [131] have numerically demonstrated the feasibility of compensating the loss in negative permittivity metamaterials using this approach.

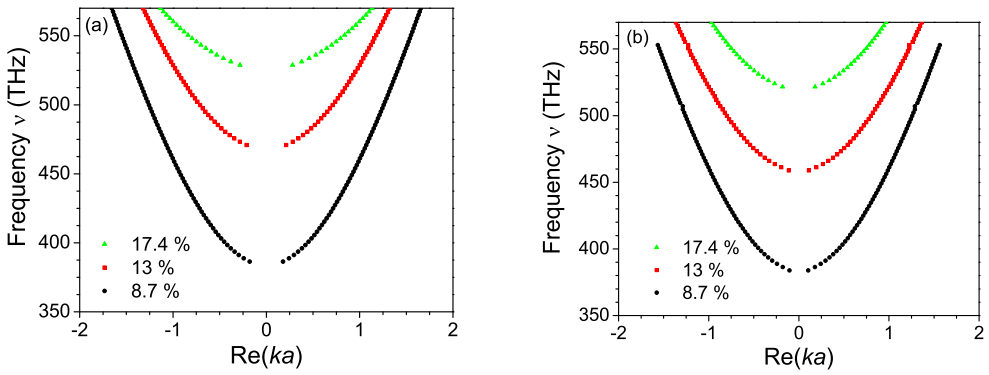

Figure 4.14: The band structure for an array of nanorods arranged (a): at the corners of a square and (b): symmetrically about the cirumference of a circular loop for filling fractions 8.7 %, 13 % and 17.4 %. In each case, the effective plasma frequency remains the same.

However, since the dielectric permittivity of quantum dots is given by

$$\epsilon_{QD} = \epsilon_B + \frac{a}{\omega - \omega_0 + i\gamma}, \tag{4.10}$$

(where ϵ_B is the background dielectric constant, γ is the broadening parameter and a is a constant which involves the oscillator strength), they exhibit a resonant permittivity. This can be used to generate a propagating band below the effective plasma frequency. Since the size of the quantum dots determines the frequency at which they respond maximally, they can be manufactured according to the frequency at which a propagating band is required, below the plasma frequency, thereby increasing the flexibility of this scheme. The nanorods needed to successfully implement this scheme can also be manufactured to a high degree of accuracy. For example, highly ordered monocrystalline silver nanowire arrays have been prepared using pulsed electrodeposition in self-ordered porous alumina templates by Sauer *et. al.* [127], as mentioned earlier in this chapter. In this technique, homogeneous filling of all the pores of the alumina template is achieved, overcoming the difficulties arising due to the instabilities during growth of the nanowires. Arrays of aligned single crystalline silver nanorods were grown on planar Si substrates using the glancing angle deposition (GLAD) technique, at substrate temperatures lower than the room temperature [128]. The major factors influencing the growth morphology

in this case are the direction of the depositing beam flux, the temperature and the movement of the substrate and the deposition rate. Well-separated, aligned silver nanorods $\sim$ 800 nm long and 20 - 30 nm in diameter have been grown using this technique [128]. Thus, the use of such composite metamaterials for switching the dilute plasma appears to be feasible experimentally. The success of the scheme for controlling the magnetic response of loop inclusions consisting of silver nanorods will depend largely upon the growth of such rods to form loop inclusions, the dispersive background medium used remaining the same. It is worth noting that while the loop inclusion has an effective magnetic response when the magnetic field of the incident radiation is axially oriented, it behaves like an effective plasma when the electric field is axially oriented. Thus, in principle, the same metamaterial can be used to generate an effective magnetic or electric response depending upon the polarization of the impinging radiation.

Chapter 5

Checkerboards of Dissipative Negative Refractive Index Media

In this chapter, a study of the electromagnetic properties of checkerboard structures of negative and positive refractive index has been presented. It is shown that such structures have novel and sometimes counterintuitive properties. The negative refractive index media can be generated by a suitable metamaterial: for example, a composite structure of appropriately sized and oriented metallic split ring resonators and thin wires can produce negative magnetic permeability and negative dielectric permittivity in a required range of frequencies (See the discussion in Sec. 1.3). It is found that checkerboard structures of positive and negative refractive index media have very singular properties resulting in very large local field enhancements and large local density of modes, both of which, in principle, can diverge for an infinite checkerboard lattice made up with dissipationless media. As a consequence, it is very difficult to accurately numerically simulate the properties of these systems. In this chapter, a study of checkerboard structures from the viewpoint of the complementarity theorem proposed by Pendry and Ramakrishna [22], has been presented. This chapter is organized as follows: First, the ideas of complementary media and the generalized lens theorem [22] have been described. The ideas of complementary media are useful for understanding the behaviour of checkerboards of positive and negative refractive index media. Next, a transfer ma-

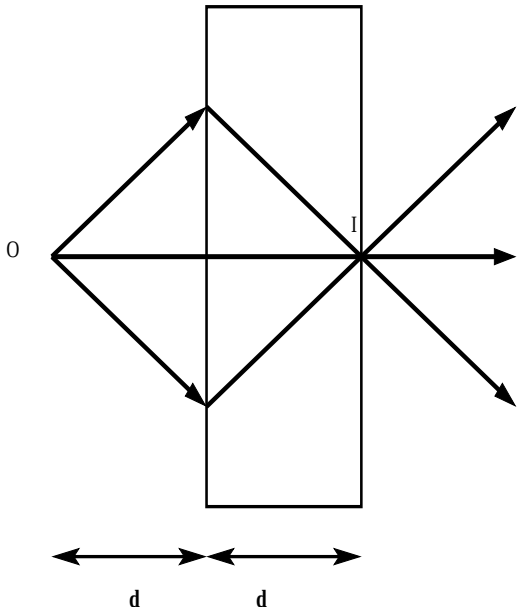

Figure 5.1: The perfect lens (consisting of a slab of negatively refracting medium with $n = -1$) proposed by Pendry in *Phys. Rev. Lett.*, **85**, 3966 (2000), and an equal thickness of vacuum (with $n = 1$) is the complementary medium of the negatively refracting slab with $n = -1$.

trix method-based approach for calculating the properties of lossy to almost loss-free to ideal, lossless checkerboards has been presented, detailing the computational challenges for this class of problems. The properties of dissipative checkerboards have also been simulated using the transfer matrix method. The imaging properties of finite-sized slabs of checkerboards have also been investigated using finite element methods. A brief look has also been taken at the electromagnetic behaviour of off-resonant checkerboards, both dissipative and non-dissipative. Finally, a short account of the electromagnetic response of checkerboards in which media having refractive indices of opposite signs are embedded has been presented.

5.1 Complementary Media and the Generalized Lens Theorem

The idea of the perfect lens [11] has since been extended to include *complementary systems of media* and a *generalized lens theorem* [22]. The perfect lens can be envisaged

to behave akin to 'optical antimatter' for light in the sense that the effects suffered by radiation in traversing a certain thickness of positive index medium are cancelled out when the radiation subsequently traverses an equal thickness of negative index medium. To an observer on the right-hand side in Fig. 5.1, it is as if the entire thickness $2d$ never existed. However, in general, it is not necessary that the negatively refracting medium be homogeneous for focussing. Any set of *complementary media* whose thicknesses are equal and satisfying the condition [22]

$$\epsilon_1 = +\epsilon(x,y), \mu_1 = +\mu(x,y), \ \forall 0 < z < d, \tag{5.1}$$

$$\epsilon_1 = -\epsilon(x,y), \mu_1 = -\mu(x,y), \ \forall d < z < 2d \tag{5.2}$$

where $\epsilon(x,y), \mu(x,y)$ may have arbitrary forms, will focus in a manner similar to the perfect lens. Further, any region that is mirror-antisymmetric about a given plane (z = constant) has an optical sum equal to zero and sets of complementary media can be eliminated from a system in a pairwise fashion [22]. Complementary media are characterized by the following properties:

$$T = 1, \tag{5.3}$$

$$R = 0 \tag{5.4}$$

$$\tag{5.5}$$

where T and R are the complex transmission and reflection coefficients. This is true for all wave-vectors, viz., $k_x/k_0 < 1$ (propagating waves) and $k_x/k_0 > 1$ (evanescent waves). However, there are small deviations when $k_x/k_0 \approx 1$. As mentioned earlier, this can be proved for any functional form of $\epsilon(x,y)$ and $\mu(x,y)$ and was numerically demonstrated by simulations carried out by means of the Transfer Matrix Method-based PHOTON codes [75, 76, 137] in Ref. [22].

It was further shown that a corner lens constructed out of NRM could be mapped (using a co-ordinate transformation [23]) into a stack of slabs where every fourth slab in the stack is complementary to the other three [22] (see Fig. 5.2). Notomi [26] showed

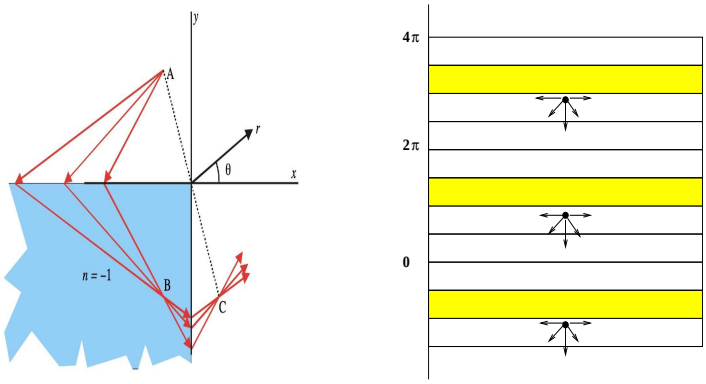

Figure 5.2: A corner reflector (left) can be mapped into a series of slabs where every fourth slab in the series is complementary to the other three (right). The point source is included in every fourth layer so that the entire system is periodic in the direction.

that two negative corners bend light around a loop and return the rays to exactly the same state from which they started. An exact realization of the condition $n = -1$ would ensure that the light would circulate for ever. In this case, the system can be mapped into a stack of slabs with sources in alternate layers where every slab is complementary to the next. The system is seen to exhibit perfect lensing. However, the fields inside are extremely singular, literally infinite in the limit of zero absorption [138]. In the electrostatic limit, Apell *et. al.* [139] have proved a theorem for surface plasmons. For a plasma with a plasma frequency ω_p,

$$\omega_{sp1}^2 + \omega_{sp2}^2 = \omega_p^2. \tag{5.6}$$

Here, ω_{sp1} are the surface of a given system and ω_{sp2} are the modes of a second system in which the regions of plasma and dielectric are exchanged. This can be used to define the plasma modes. For systems that map onto themselves, one has

$$\omega_{sp1} = \omega_{sp2}. \tag{5.7}$$

Thus, in the electrostatic limit, all the plasma modes of the system are degenerate at

$$\omega_{sp} = \frac{\omega_p}{\sqrt{2}}. \tag{5.8}$$

At this frequency, the density of states becomes infinite. Thus, the local density of states near any of the surfaces becomes extremely high, particularly at the corners of the system.

5.2 Limitations of real materials and imperfect NRMs

For a perfect lens made of real metamaterials, the inherent large momentum cut-off set by the underlying structures of the metamaterial makes infinite resolution impossible. In addition to this, several other factors are expected to limit the performance of a perfect lens. Smith *et. al.* [140] studied the sensitivity of subwavength resolution on the slab properties and periodicity and its link with the surface plasmon modes. They concluded that the resolution of a LHM depends logarithmically on the deviation of ϵ and μ from -1, and inversely on the width of the slab. Deviations in either Re(ϵ) or Re(μ) affect the image in the same way, depending upon the polarization of the incident radiation. Thus, p-polarized radiation will be more severely affected by deviations in ϵ from -1, while s-polarized light is affected by the deviation of μ from the ideal conditions. However, deviations in μ from -1 also sets a limit for the maximum resolution possible with p-polarized light, even if ϵ has the ideal theoretical values and is non-dissipative. The periodicity of the metamaterial may limit the resolution by affecting the recovery of non-propagating components with a large wave number. Merlin [141] also concluded that the resolution of a slab of lossless LHM (whose $n = -\sqrt{(}1 - \sigma))$ depends logarithmically on $|\sigma|$, where σ is the deviation of the LHM from the perfect lens condition. The FDTD calculations of Ziolkowsky and Heyman [142] suggested that the perfect lens effect could only be observed under the exact restrictive condition $\epsilon = -1, \mu = -1$, and is not realizable with any realistic metamaterial. This has since been explained in [143]. It has been pointed out [143] that the resonant surface plasmon modes at the interfaces for $n = -1$ are always excited by any causal incident wave or pulse with finite bandwidth. In a FDTD calculation, these resonances remain active indefinitely. Thus, some amount of dissipation in the material parameters has to be introduced

to enable the calculations to reach a steady state within a reasonable period of time. FDTD simulations thus effectively never reach a steady state with any lossless NRM. For a slab with a finite transverse extent, though some propagating waves at large angles may be lost, there is no loss of evanescent components and hence, all the near field information is preserved [144]. However, plasmons on the slab surface can form standing waves and significantly distort the image. These effects are limited in the presence of absorption. In Ref. [138], the spatial oscillations of plasmons at interfaces were shown to have a logarithmic dependence on the absorption. As mentioned earlier, the imaging properties of perfect lenses and hence, checkerboards depend upon the amount of dissipation, dispersion and imperfections in the metamaterial. In fact, it is well known that dissipation affects the sub-wavelength resolution badly and the singular density of modes at the corners are expected to worsen it.

5.2.1 Limitations of FDTD analysis for a perfect lens imaging system

As mentioned earlier, FDTD techniques were unsuccessful during prior attempts at solving the checkerboard problem. The reasons behind this can be analysed as follows. Owing to the frequency-dispersive nature of the medium and the time discretization, there exists an inherent mismatch between the constitutive parameters of the slab and its surrounding medium. This mismatch in the real part of ϵ and μ is found to be of the same order of magnitude as the losses typically used in numerical calculations. Thus, when the LHM slab is lossless, this mismatch contributes the most to the loss of resolution of the image [145]. This is because the resolution of a subwavelength imaging system is critically dependent on the reconstruction of evanescent waves by the LHM slab. The reconstruction again depends on the constitutive parameters of the slab and even a slight mismatch ($\sim 0.03\%$) in $\mathrm{Re}(\epsilon)$ or $\mathrm{Re}(\mu)$ significantly affects the imaging properties of the LHM slab. This small perturbation in $\mathrm{Re}(\epsilon)$ or $\mathrm{Re}(\mu)$ are often overlooked and imaginary parts with a value in the same order are typically considered to be the main factor for limiting the image resolution.

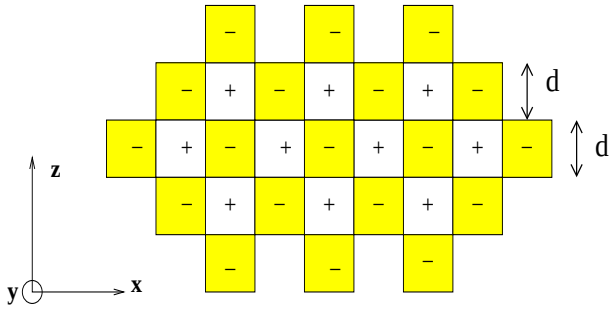

Figure 5.3: Schematic representation of an infinite checkerboard consisting of alternating cells of positive and negative index media. A source of radiation placed in one cell of such an infinite checkerboard will form an image in every other cell.

The checkerboard systems studied in this chapter have a finite transverse extent and have finite levels of dissipation associated with them as well. Their imaging properties may be hindered by the loss of propagating waves at large angles or the distortion of the image by the standing waves formed by the plasmons on the slab surface. The resolution of a perfect lens is also known to be dependent (logarithmically) on the absorption in the medium [141, 140]. Thus, it important to investigate the effect of the finiteness of the system and the levels of dissipation in it on its transmission and imaging properties, in the light of the fact that an experimental study of checkerboards will involve finite sizes and finite dissipation.

5.3 Checkerboard systems

In this section, the electromagnetic response of checkerboard systems in which every cell is complementary to the other in the $x-y$ (horizontal) plane, has been investigated. The system is invariant along the z direction. An infinite checkerboard consisting of optically complementary cells produces an image of the source in every other cell of the lattice [146] (Fig. 5.3). This is true for both homogeneous isotropic checkerboards as well as inhomogeneous anisotropic ones as long as they are mirror antisymmetric along the principal axes of the system. The local density of states becomes infinite at the corners for the limiting case of infinitely large-sized lattices of non-dissipative checkerboards. For finite-sized checkerboards, only leaky modes are present in the system, irrespective

of whether the medium is dissipative or non-dissipative.

The singularity of the system and the diverging density of modes at the corners makes it extremely difficult to predict the physical behaviour of checkerboard systems. These systems are highly susceptible to showing numerical artifacts if numerical modelling is not done carefully. Consequently, numerical calculations are carried out in a manner such that the results remain consistent with the complementarity theorem, which is the only analytical result which is available for predicting the behaviour of these systems. This can be used to differentiate between numerical artifacts, such as spurious resonances and the actual physical behaviour of these systems. In addition, accurate numerical modelling of these systems necessitates the use of a fine numerical grid.

The behaviour of this system (as dictated by the generalized lens theorem)is quite counterintuitive. As shown in Fig. 5.4, a ray analysis shows that the incident rays can either be transmitted or retro-reflected. However, the wave analysis predicts full transmission. The ray analysis which is essentially an approximation, is highly inadequate for checkerboard systems due to the large localized fields at the corners which it cannot describe. This is automatically taken care of in a full-wave calculation, which consequently provides the correct picture for the transmission of electromagnetic waves across such singular systems. A similar phenomenon was demonstrated in Ref. [147] for triangular checkerboards.

5.3.1 Transfer matrix analysis of transmission properties of ideal and complementary checkerboard layers

The numerical solution of the problem of ideal checkerboards is non-trivial. Initial attempts to solve the problem using FDTD methods did not succeed due to the divergences arising in the calculations which were later traced to finite differencing effects [148, 149, 8, 145]. The numerical solutions to this problem, obtained using a refined version of the PHOTON codes based on the Transfer Matrix Method are presented here. The checkerboard regions were sliced into thin layers along z with thicknesses consisting

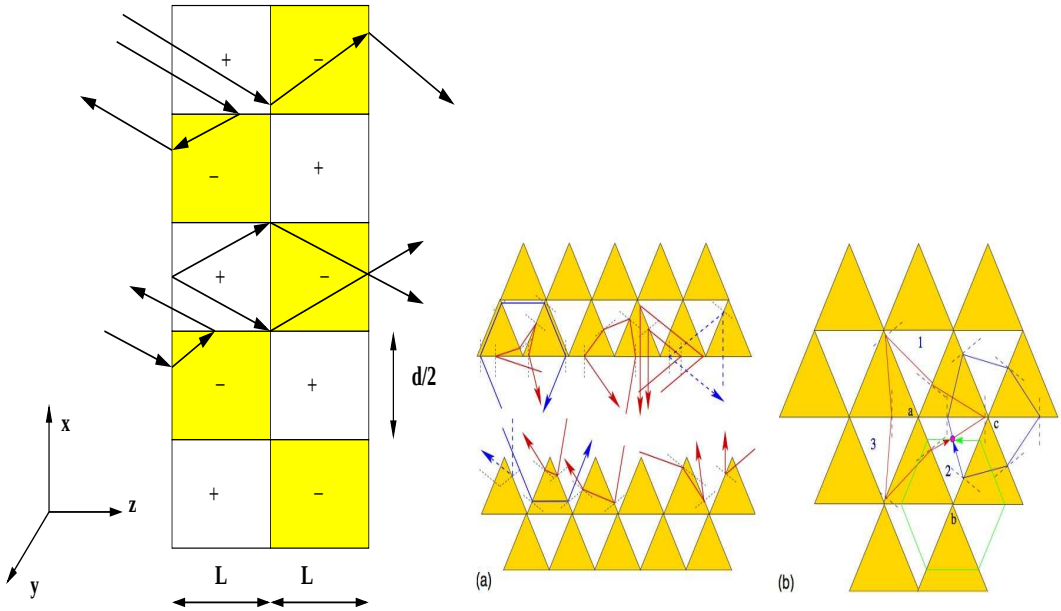

Figure 5.4: A checkerboard of width L illustrating the conflict between the ray picture and the wave picture. According to the ray analysis, a ray may be transmitted or retro-reflected while the full wave solutions of Maxwell's equations validate the results of the generalized lens theorem that unit (complete) transmission occurs for all wave vectors.

of only 7 to 11 mesh points to avoid numerical instabilities [137]. The transfer matrix across each of these thin layers was calculated by propagating Maxwell's equations along the z-axis using a finite differencing scheme. The transfer matrices for these layers were then combined using a multiple scattering formalism [76] to yield the final transfer matrix for the entire system. A free space wavelength of $= 4.53\mu$m, together with periodic boundary conditions along x (with a period of $d = 1.11\mu$m or 2.22μm) and a typical layer thickness of $L = 0.45\mu$m ($\lambda/10$ were used. It should be noted that the period along x is irrelevant to the effects discussed in this chapter. It was ensured that the position of the numerical grid with respect to the checkerboard boundaries is such that the averaged values of ϵ and μ at any grid point do not become zero (singular) [148]. The other numerical approximations used are those inherent in the PHOTON codes [75, 137].

In Fig. 5.5, the transmission and reflection coefficients for a plane wave incident on this ideal checkerboard slab as a function of the parallel wave-vector k_x have been presented. In the top panels (a) and (b), the results obtained using 202 mesh points across period d have been shown. It is found that although the transmission is approximately one for the propagating waves ($k_x < k_0 = \omega/c$), the reflectivity and the phase (ϕ_T) of

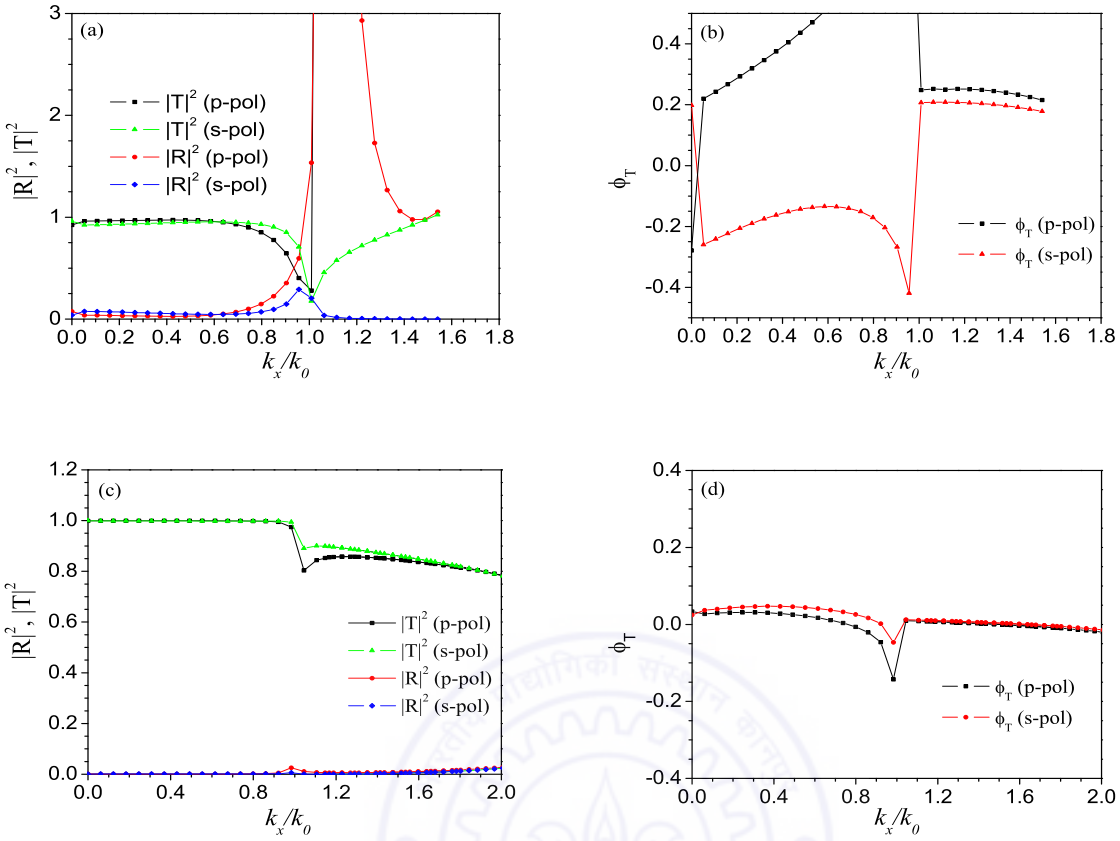

Figure 5.5: The perfect checkerboard characterized by $\epsilon_- = -1$, $\mu_- = -1$, $\epsilon_+ = +1$, $\mu_+ = +1$. These plots illustrate the importance of the fineness of the numerical grid in achieving accurate numerical results. (a) and (b): The response of the same system as calculated using a numerical grid containing 202 points. A resonance (actually a numerical artefact), occurs at $k_x \simeq k_0$, for better discretization, this shifts to $k_x \simeq 3k_0$. (c) and (d): The response of the 'perfect checkerboard' as calculated using a fine numerical grid consisting of 262 points. The transmittivity is nearly zero and the phase change of the transmitted component (ϕ_T) is nearly zero throughout.

the transmission are non-zero (for both p- and s-polarized light). The transmission coefficient also becomes very large for subwavelength $k_x > k_0$. One also observes the appearance of a resonant response of a slab polariton at subwavelength wave-vectors whereas the generalised lens theorem predicts that no resonance will be excited for any finite value of k_x for $\epsilon = \mu = \pm 1$. This spurious resonance shifts to larger values of k_x as the numerical mesh size is decreased. In the lower panels (c) and (d), the response obtained for better discretization (262 points across d), has been plotted. The spurious resonance now shifts to a point beyond $k_x = 3k_0$ and the transmittivity becomes closer

to unity with zero phase shift. The reflectivity is zero as well over a large range of wave vectors upto the resonance wave vector. This behaviour has been illustrated in Fig. 5.5 (c), for wave-vectors upto $k_x = 2k_0$ for both states of linearly polarized light. Fig. 5.5 (d) shows the phase change of the transmitted wave for the same wave-vectors and it is observed that ϕ_{T} is nearly zero throughout, as expected using the generalized lens theorem. Near $k_x \simeq k_0$, a slight discrepancy with the complementary media theorem may be observed. This arises due to the impedance mismatch caused by an expansion of plane waves in free space and it may be removed if the impedance matching is improved (See [22]).

The sensitivity of the solutions to numerical errors and excitation of spurious resonances, may be explained by considering the dispersion of the finite difference equations on a simple cubic lattice in media with spatially constant material parameters [76]:

$$\begin{aligned} \omega^2(k) &= \frac{c^2}{\epsilon\mu a^2} 4\sin^2(ka/2) \\ &\simeq \frac{c^2k^2}{\epsilon\mu}\left[1 - \frac{1}{12}(ka)^2\right]. \end{aligned} \tag{5.9}$$

Here a is the numerical grid size. This evidently tends to the dispersion for the continuum Maxwell equations only when $ka \ll 1$, or particularly for very small a when subwavelength wave-vectors are considered. The above dispersion can be written as

$$k^2 = \epsilon\mu\frac{\omega^2}{c^2}\left[1 + \frac{1}{12}(ka)^2\right], \tag{5.10}$$

The second term can then be regarded as arising from a deviation, $\delta\mu$ in μ (or in $\delta\epsilon$ in ϵ) from the ideal case of $\epsilon = \mu = \pm 1$ that has been considered here. The deviation,

$$\delta\mu = \frac{\mu(ka)^2}{12} \tag{5.11}$$

in the real part of the permeability gives rise to a resonant excitation on a slab of NRM

of thickness t with a parallel wave-vector (k_x) [140],

$$k_x d = -\ln(\frac{\delta\mu}{2}) = -\ln(\frac{k_x^2 a^2}{24}) \tag{5.12}$$

in the limit of large parallel wave-vector $k_x \gg k_0$.

In the limit $k_x a \ll 1$, the parallel wave-vector for this spurious resonance induced by the discretization will be $k_x \sim$ (a large number)$/d$. In the ideal continuum limit of $a \to 0$, we have $k_x \to \infty$, as expected from the continuum equations. Thus, at any level of discretization, a spurious resonance of the system (s) for some finite k_x will always be excited in a numerical calculation. The value of the the parallel wave-vector $k_x^{(s)}$ for the spurious resonance gives the range of k_x significantly smaller than the $k_x^{(s)}$ for which the calculations would have converged. In our problem of the checkerboard, d can be taken to be the larger dimension of the checkerboard cell. In that case, the expression above in the long wavelength limit gives $k_x^{(s)} \sim 3k_0$ for $d \sim \lambda/2$ and $k_x^{(s)} \sim 8k_0$ for $d \sim \lambda/4$. This approximate estimate is in reasonable agreement with the numerical calculations where retardation effects also play a role and the geometry is also more complicated than a simple slab.

The other significant deviation, mainly at $k_x \sim k_0$, can be attributed to the numerically approximate impedance matching at the interfaces. Thus, within the accuracy of our numerical scheme, the generalised lens theorem for this system has been verified for $k_x < 2.5k_0$.

5.4 Dissipative Checkerboards of Finite Extent

The properties of finite two-dimensional (2-D) checkerboards of dissipative but homogeneous NRM have been discussed in this section. A layer of a 2-D checkerboard in the $x - z$ plane and of thickness L along z, along with its complementary checkerboard (of the same thickness), embedded in vacuum (Fig 5.6), is considered. Invariance along the y axis is assumed. The response of this system for the ideal lossless values of the per-

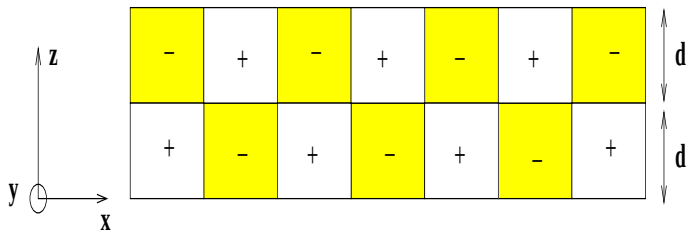

Figure 5.6: A checkerboard of finite width such as those studied in this section. It has been shown to obey the generalized lens theorem and exhibits unit transmittivity and zero reflectivity for all wave-vectors, both the propagating as well as the evanescent.

mittivity and the permeability, $\epsilon = \pm 1$ and $\mu = \pm 1$, were calculated and have already been presented in the previous section.

5.4.1 The electromagnetic response of dissipative checkerboards

The response of checkerboards was calculated for various levels of dissipation. In this section, the checkerboards studied may be described as $\epsilon_+ = (1, 0), \epsilon_- = (-1, \alpha_e), \mu_+ = (1, 0)$ and $\mu_+ = (-1, \alpha_m)$. α_e and α_m range between 10^{-4} to 0.1. In the results presented here, the same levels of dissipation are associated with both the dielectric and the magnetic properties under consideration, i.e., $\alpha_e = \alpha_m$. This analysis also tests the robustness of the focussing effects against dissipation. In Fig. 5.7 and Fig. 5.8, the transmission and reflection coefficients for dissipative checkerboards have been plotted. When the imaginary parts of ϵ and μ are nearly 10^{-4} , the results were not very different from that of the lossless system (Fig. 5.7 (a) and (b)). Even with larger values of 0.1 for both Im(ϵ) and Im(μ) (Fig. 5.8), it can be seen that although the transmission is not total, it is clearly very flat as a function of k_x even for sub-wavelength wavevectors (Fig. 5.8 (c) and (d)). Thus, one can infer that the focussing effects in the system will be robust against dissipation, probably as robust as in the single slab lens. This is surprising in view of the divergences in the local density of modes at the corners. The gradual evolution of the checkerboard response for different levels of dissipation has been shown in Fig. 5.7 and Fig. 5.8. The transmittivity indicates that a considerable amount of subwavelength information can still be transferred, inspite of the dissipation in the system. The results for the checkerboards with realistic levels of dissipation indicate that

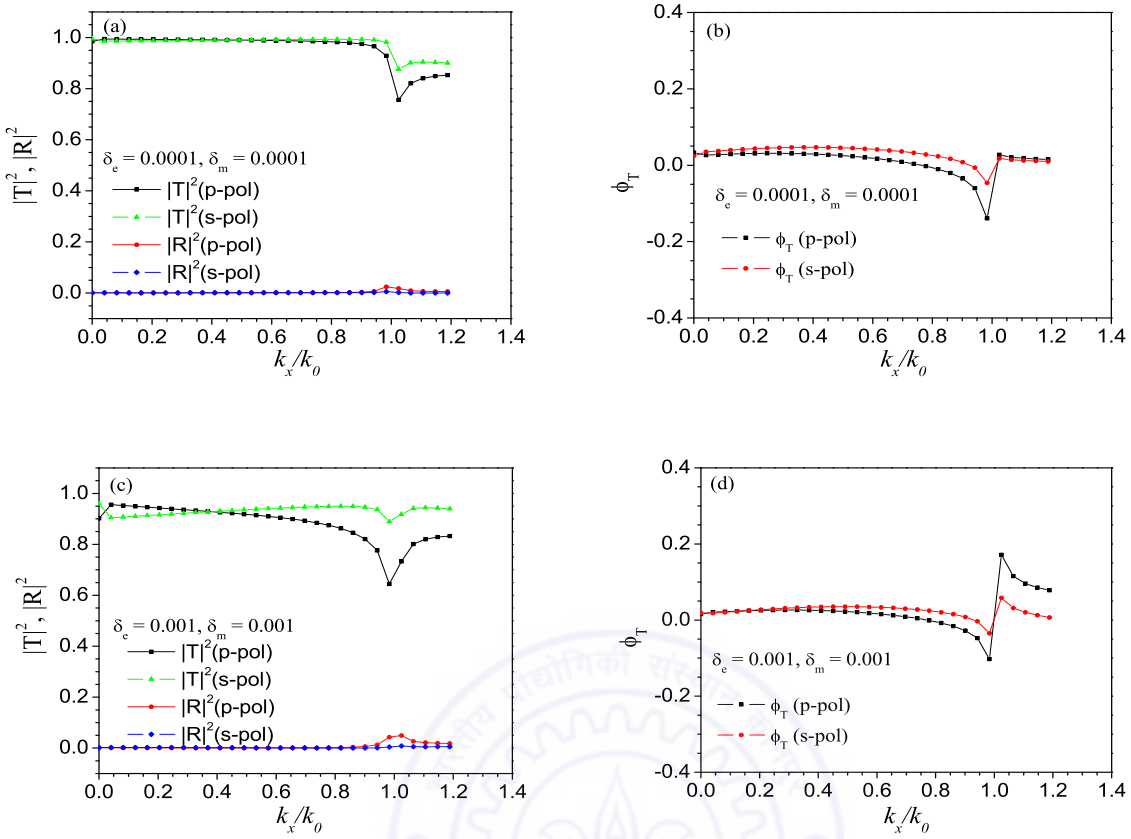

Figure 5.7: (a) & (c): The transmission properties of dissipative checkerboards whose Im(ϵ) and Im(μ) are 0.0001 and 0.001 respectively.
(b) & (d): The phase change of the transmitted component for both polarizations of light and for the same levels of dissipation in (a) & (c), respectively.

if practically implemented, these structures would continue to replicate subwavelength features of the object.

It should be noted that the dissipation here is comparable to that in silver which has been suggested and used as a near-field lens. We have also calculated the response of a silver-vacuum checkerboard with $\epsilon = -1+i0.4$ and $\mu = +1$ (Fig. 5.9). The transmittivity and reflectivity for dissipative checkerboard systems with $\epsilon = \mu = -1+i0.1$ (right panel) and a silver checkerboard with $\epsilon = -1+i0.4$ and $\mu = +1$ everywhere (left panel). can be compared. In the case of the silver checkerboard, resonant excitation of surface plasmon modes at subwavelength k_x for p-polarized waves only, can be seen.

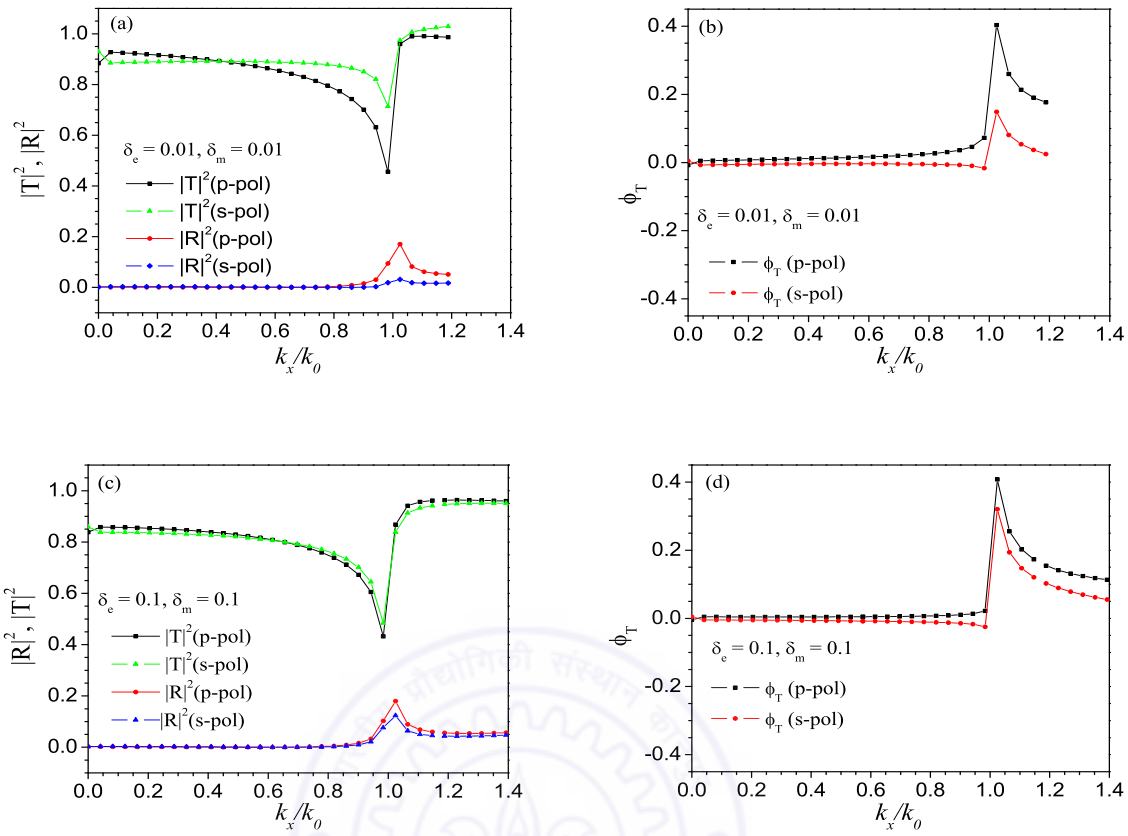

Figure 5.8: (a) & (c): The transmission properties of dissipative checkerboards whose Im(ϵ) and Im(μ) are somewhat higher, being 0.01 and 0.1 respectively.
(b) & (d): The phase change of the transmitted component for both polarizations of light and for the same levels of dissipation in (a) & (c), respectively.

5.5 Off-resonance checkerboards

In the spirit of the preceding sections, the behaviour of checkerboard systems where the permittivity and the permittivity in adjacent cells are not complementary to each other has been briefly studied here. Such off-resonant checkerboards assume importance in the light of the fact that the highly singular condition $\epsilon = -1, \mu = -1$ is difficult to achieve at a single frequency. Here the checkerboard has the following configuration: $\epsilon_+ = +1, \mu_+ = +1, \epsilon_- = -1 + \alpha_e + i\delta_e, \mu_- = -1 + \alpha_m + i\delta_m$. α_e and α_m represent the deviation of the checkerboard from the ideal condition in the real parts while δ_e and δ_m represent the dissipation. Thus, the condition of degeneracy of the surface plasmons is lifted. Together with the dissipation in the system, the deviation from the

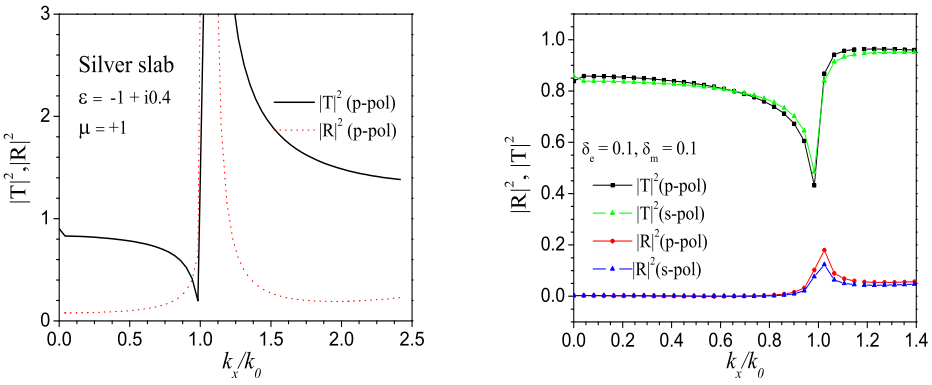

Figure 5.9: The transmission properties of a checkerboard of silver ($\epsilon = -1 + i0.4$ and $\mu = +1$), as shown in the left panel. The resonant excitation of surface plasmon modes for p-polarized light only, is observed. The behaviour of this system may be compared to the transmission properties of checkerboards of dissipative NRM, having similar levels of dissipation (shown in the right panel).

$\epsilon = \pm 1, \mu = \pm 1$ condition is expected to affect the imaging significantly. It may be noted that the values of α_e and α_m considered are such that the permittivity and the permeability remain negative in the regions concerned and surface plasmon states can exist on the boundary between a positive and a negative cell. In the four cases studied, the regions of positive and negative index are such that $\alpha_e = \alpha_m$ and $\delta_e = \delta_m$. This ensures that the regions are impedance matched. However, this will not be true always and the impedance mismatch will result in a finite reflectivity.

The transmission properties of such checkerboards have been presented in Fig. 5.10. It is found that the checkerboards remain transmittive for propagating waves. For evanescent waves, numerical artefacts begin to appear. For $\alpha_e = \alpha_m = -0.1$, near-perfect transmission is obtained upto $k_x/k_0 = 1.6$. If the deviations in ϵ and μ are increased to $\alpha_m = \alpha_e = -0.5$, the transmittivity begins to drop rapidly near $k_x \simeq k_0$, and rises rapidly thereafter indicating a resonance.

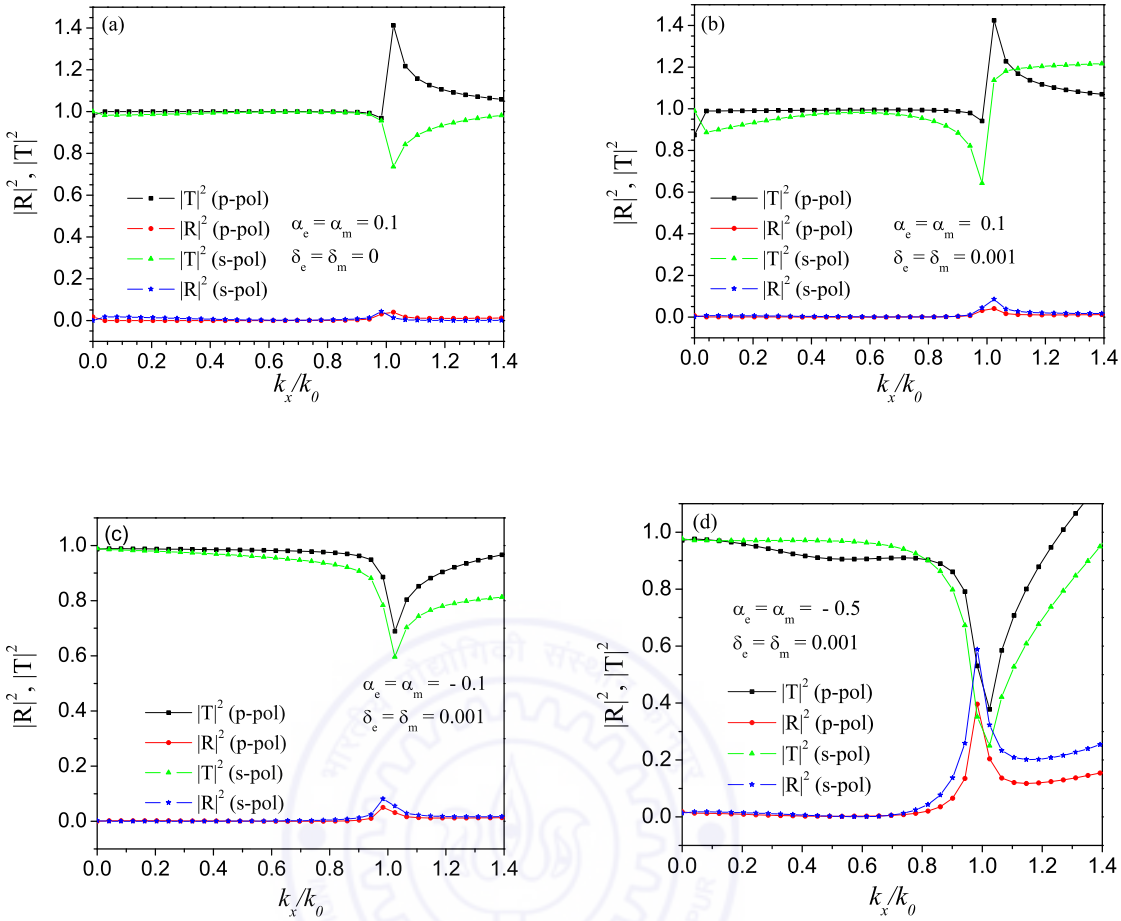

Figure 5.10: The response of off-resonance checkerboard structures (dissipative and non-dissipative). The permittivity and the permeability of these checkerboards have the generic forms $\epsilon_+ = +1, \mu_+ = +1, \epsilon_- = -1 + \alpha_e + i\delta_e, \mu_- = -1 + \alpha_m + i\delta_m$. When the mismatch ~ 0.1, perfect transmission is obtained upto $k_x \simeq k_0$ for the lossless case. For dissipative checkerboards with a higher degree of mismatch, the transmission is considerably lower for propagating waves. Numerical artefacts also start appearing for $k_x > k_0$.

5.6 Some Other Checkerboard Structures

Other structures similar to the checkerboard structures such as the one shown in Fig. 5.11 are also expected to have similar behaviour as well as follow the perfect lens theorem as long as the generalized lens theorem is obeyed. Such a checkerboard slab expected to display unit transmission for all waves as long as the different sections of checkerboard are optically complementary to each other. It is found that, as expected, these media exhibit nearly unit transmittivity and zero reflectivity even for sub-wavelength wave

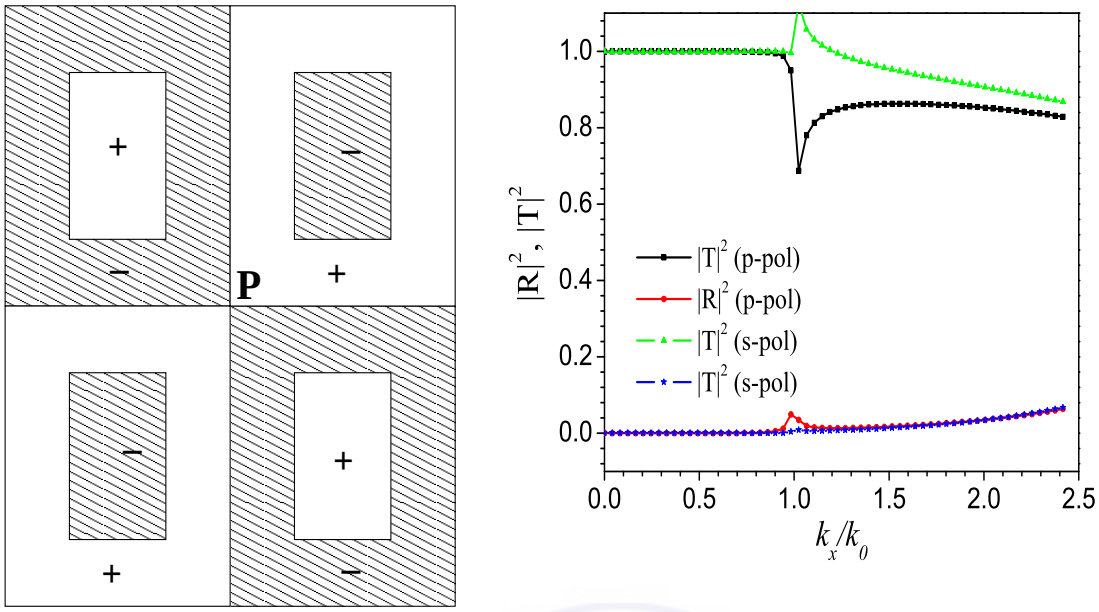

Figure 5.11: Left: An example of the unit cell of a modified checkerboard medium studied in this section. The shaded regions correspond to the negative refractive index regions. Locally enhanced fields occur near the central point (P) and these fields increase as the inner regions of negative/positive index media are increased in size. Right: The reflectivity and the transmittivity of such a checkerboard.

vectors. There are large enhancements of the electric field near the boundaries of the positive and the negative index media. The results [150] of calculations for checkerboard structures with the embedded 'defect' regions having three different thicknesses have been presented in Fig. 5.11. The transmittivity indicates that the system behaves as predicted. As seen in the earlier cases, the accuracy of the numerical grid is very important. Any small mismatches in the widths of the regions results in the appearance of numerical artifacts. The electric field distribution in the system for an incident plane wave, calculated using FEM (COMSOL^{TM}) have also been presented. Surface plasmon modes are seen to be excited on the boundaries between the positive and the negative index regions. The fields are found to be strongly confined about the central point in Fig. 5.11. The larger the inner rectangular 'defect' regions, the higher is the electric field in the *thin bridges* formed out of media with refractive indices of opposite signs. As the inner regions with the opposite indices become smaller, concentration of the electric fields in the central bridging region reduces but nevertheless the fields there are higher

compared to those in the other regions.

5.6.1 FEM calculations

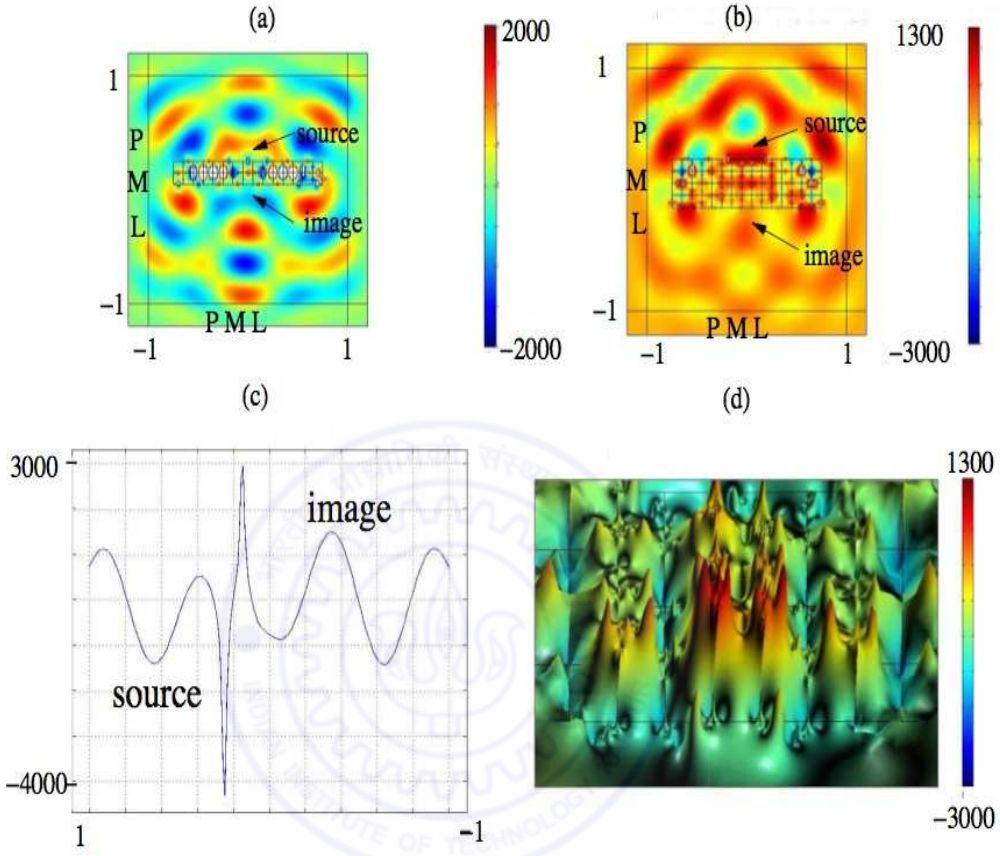

Figure 5.12: Left panel: The P-polarized eigenfield associated with a line source whose wavelength is $0.5d$ (d is about 9μm) placed at a distance $0.2d$ from a silver checkerboard slab consisting of 30 cells of side length $0.1d$, alternating air and weakly dissipative silver cells ($\epsilon = -1 + i0.01$ and$\mu = +1$). The scale on the right is in arbitrary units. (a) 2D plot of the field; (c) Profile of the field computed along a vertical segment with end points $(0,1)d$ and $(0,-1)d$.
Right panel: Same with two pairs of complementary checkerboard layers (60 cells); (b) 2D plot of the field; (d) 3D plot of the field.

In this section, the behaviour of a silver checkerboard lens of finite transverse size has been discussed first. Fig. 5.12 depicts the response of a small, slightly dissipative checkerboard system consisting of thirty cells with $\epsilon = -1 + i0.01$ and $\mu = +1$, for a line source placed at point (0, 0.6) for the p-polarization. The numerical problem was set using the weak form of Maxwell's system and discretising it with test functions

(Whitney 1-forms, or Nedelec edge elements) defined as

$$\mathbf{w_e} = \lambda_i \nabla \lambda_j - \lambda_j \nabla \lambda_i \tag{5.13}$$

on the edges between vertices i and j of the triangle of the mesh with barycentric coordinates λ_i (the FEM mesh generator is a grid-based Delauney triangulation). Such vector fields are known to have a continuous tangential component across interfaces between different media (hence exhibiting two anti-parallel wave-vectors at both sides of interfaces between complementary media). The use of such curl-confirming elements avoids the generation of spurious modes [151] and is particularly well suited for high-contrast media and left-handed materials. The use of nodal elements is problematic as the 'penalty term' or the 'stiffness' term involved in the weak formulation of the problem itself vanishes for left-handed media. The continuity of the normal components of the fields on the boundary between elements has to be enforced for the nodal element formulation, while no such condition is forcefully implemented in the edge-element approach. The (hypo) ellipticity of Maxwell's system is ensured by the small dissipation, and existence and uniqueness of the solution is a consequence of outgoing-wave conditions enforced with Perfectly Matched Layers [152] which provides a reflectionless interface between the region of interest (large middle square containing the line source and the checkerboard on Fig. 5.13, for example), and the PML (four elongated rectangles and four small squares) at all incident angles. The use of Nedelec edge elements is particularly well suited for implementation of PML as this can be seen as a geometric transform for which differential forms are well suited (pull-back properties). Numerical simulations have been carried out with an adaptive mesh of upto 91780 finite elements to check the convergence of the finite element method (implemented in COMSOL^{TM} which uses robust ARPACK solvers). One can clearly see that the source is reproduced in the focal plane of the checkerboard lens on upper left panel of Fig. 5.12 (a). Fig. 5.12 (c), represents the profile of the p-polarized eigenfield computed along a vertical segment running from point (0, 1)d to point (0, -1)d. An anti-symmetric plasmon mode excited at the upper interface between positive and negative index media (upper boundary of

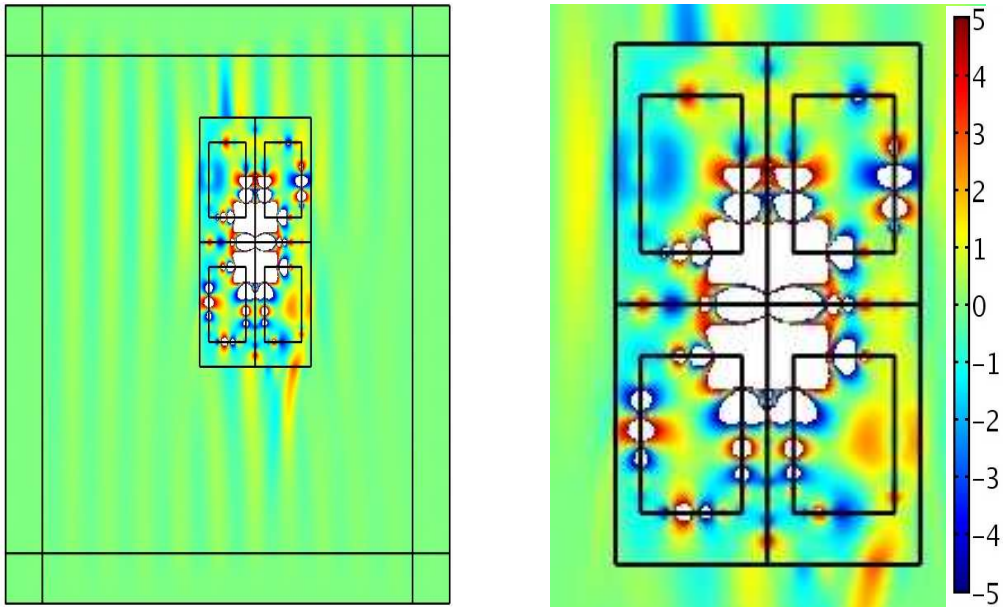

Figure 5.13: A modified checkerboard (of finite extent) of the kind studied in Sec. 5.6. Locally enhanced fields occur near the central point and these fields increase as the inner regions of negative/positive index media are increased in size.

the checkerboard) can be clearly seen.

In Fig. 5.12 (c), it can be see that the intensity of the p-polarized eigenfield is of the same order in the focal planes of the source and image. Fig. 5.12 (b) represents the imaging properties of a system consisting of two pairs of complementary cells (checkerboards of thickness $0.4d$). It is observed that the focussing effect survives. These calculations also reveal the presence of surface plasmon modes on the interface between positive and negative cells. In Fig. 5.12 (d), the 3D plot of the eigenfield exhibits plasmon resonances running along interfaces between complementary media (note the view is rotated by π compared with (b)). Some images in the neighborhood of the source are building up in the first two rows of the checkerboard (8 red peaks are located in a symmetric fashion within 8 adjacent cells with smaller peaks appearing around). It is interesting to note that the imaging effect remains visible even when the location of the source is changed. Even though the generalised lens theorem predicts only an imaging effect when the source lies close to the heterogeneous slab lens, the numerical simulation shows that the imaging is still present when the source lies two cells away from the checkerboard. However, since the evanescent waves from the object are involved, the nearer the source,

the better is the imaging expected to be. Fig. 5.12 (b) shows that the image is slightly closer to the checkerboard slab than the image. In addition, when we increase the size of the checkerboard, the imaging process is found to be robust against dissipation.

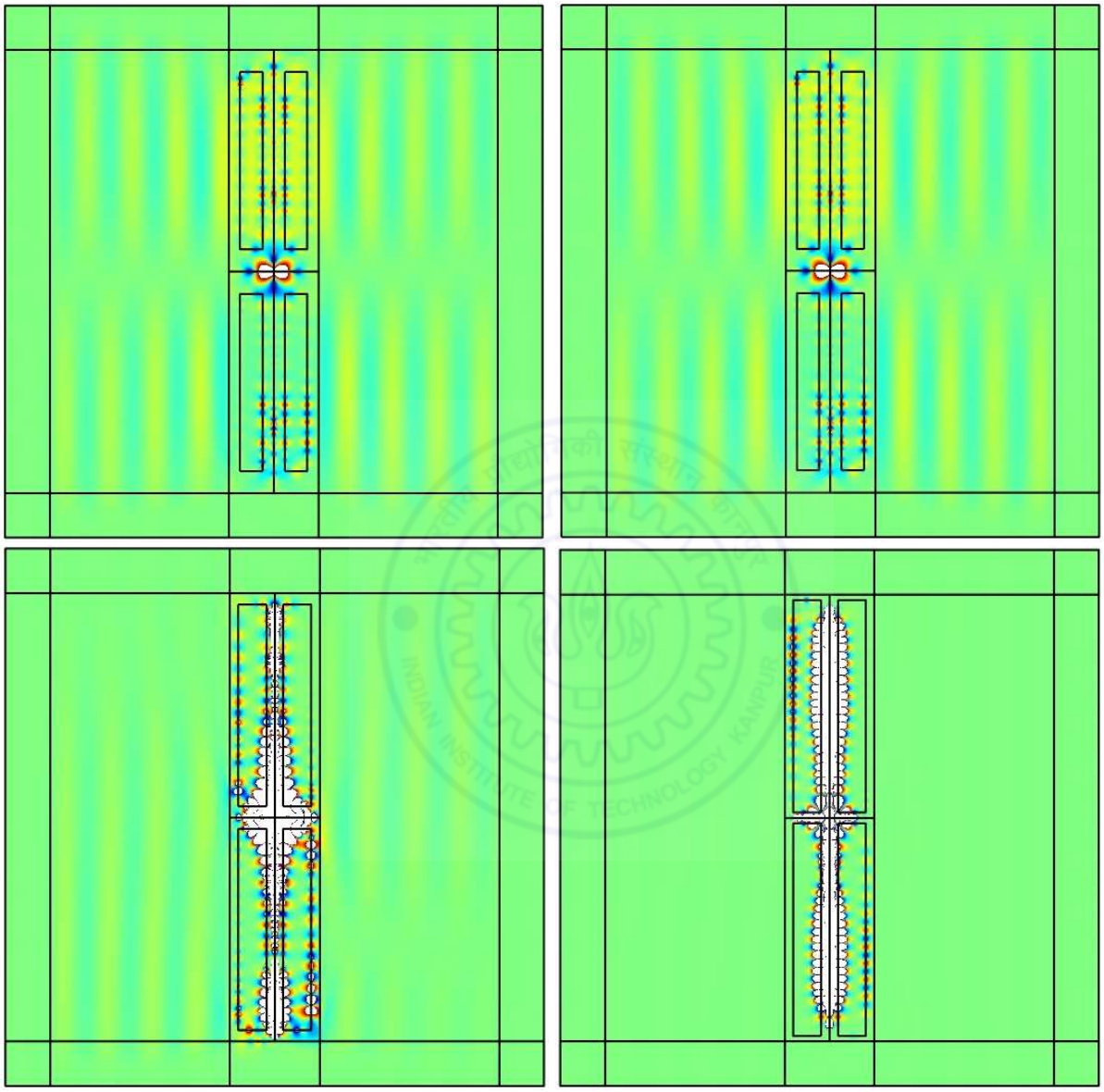

Figure 5.14: A modified checkerboard (of infinite extent) of the kind studied in Sec. 5.6. The locally enhanced fields occuring near the central point increase in intensity as the inner regions of negative/positive index media are increased in size. The fields at the central regions (white) exceed those in the neighbouring regions by several orders of magnitude as the inner regions of negative/positive index media increase in size (Bottom, left and right panels).

In Fig. 5.13 and Fig. 5.14, the results of finite element calculations of the checkerboards described in Sec. 5.6 carried out using COMSOL^{TM} have been presented. Fig. 5.13 illustrates the response of a finite checkerboard of this type when illuminated by a plane wave. The wave propagates across the medium, with large fields building up in the central part of the checkerboard. The excitation of surface plasmon modes at the interfaces between the positive and the negative index media can also be observed. The surface plasmon modes also give rise to the strongly localized fields. The distortion in the fields at the boundary of the checkerboard is due to its finite size.

Similar calculations were carried out for such infinite checkerboards of with embedded regions of media with opposite indices of refraction. The effects of the finite size of the checkerboard are seen to go away. Large localized fields, whose magnitudes exceed those in other regions by several orders of magnitude, occur at the central region of the checkerboard. These fields increase in magnitude as the embedded regions become larger. The local density of states in these regions is very high.

5.7 Conclusion

In this chapter, the ideas of the generalized lens theorem have been extended to complementary checkerboards of positive and negative index media. Checkerboards of both lossless as well as dissipative NRM have been dealt with. The behaviour of this system is quite counterintuitive and ray analyses are shown to contradict the predictions of the generalized lens theorem. It has been shown that the numerical solution of this problem is a non-trivial issue that is highly susceptible to numerical artifacts that stem from discretization issues. Using TMM-based methods with an appropriate level of discretization for the numerical grid, the behaviour of 'perfect' checkerboards was adequately simulated from the viewpoint of the generalized lens theorem. The transmittivity was shown to be nearly unity both for the propagating as well as subwavelength wave-vectors along with zero phase change for the transmitted component upto $k_x \simeq 3k_0$. A spurious resonance which formerly occurred at $k_x \simeq k_0$ for inadequate discretization was shown to

get pushed beyond $k_x \simeq 3k_0$ when finer levels of discretization were used.

Similar calculations were carried out for dissipative checkerboards. In the case of dissipative checkerboards, the imaging effects are seen to be preserved even for reasonably high levels of dissipation. Although the overall transmission is lowered, a considerable amount of subwavelength information may still be transferred for realistic levels of dissipation, comparable to that in silver which has been proposed and used as a near-field lens. The response of a silver checkerboard calculated similarly has also been compared to a dissipative checkerboard with similar loss. These calculations illustrate the fact that within the accuracy of the numerical calculations presented, focussing effects in checkerboards of NRM are reasonably robust against dissipation, at least as robust as in slabs of negative index media. This is surprising in the face of the expectation that dissipation in such singularly degenerate systems should have wiped out all such effects.

Similar calculations were performed for checkerboards whose material properties deviated by small amount from the highly singular condition $\epsilon = \pm 1, \mu = \pm 1$. In all the cases, transmission is nearly unity for the propagating waves, while for the evanescent waves, spurious resonances crop up.

The electromagnetic response of checkerboards with embedded regions of media with indices of opposite signs was studied using the transfer matrix method as well as COMSOL$^{\text{TM}}$. These checkerboards are found to obey the generalized lens theorem and exhibit perfect transmission in the absence of losses in the checkerboards. Finite element calculations reveal the presence of localized and enhanced fields in the central region of the checkerboard. The enhanced fields and the local density of states in this region increase greatly as the embedded regions of opposite index become larger in size.

Chapter 6

Future Directions

So far, the behaviour of metamaterials at optical frequencies, leading to the breakdown of effective medium behaviour and schemes for controlling metamaterial responses at optical frequencies have been examined. In addition, the electromagnetic response of checkerboard structures of negative and positive index media and its sensitivity to the numerical modelling involved has also been studied. These ideas can, however, be extended further and can be implemented in numerous applications in a versatile manner.

The breakdown of the homogenization approach is one aspect which can be further studied. The effective parameters also start showing spatial dispersion as the unit cell size of the metamaterial becomes comparable to the wavelength at resonance. In such cases, a set of restricted spatially dispersive equivalent medium parameters may be used to model the response of the metamaterial. Most material implementations are somewhere at the range of this breakdown and hence, such modelling owuld be tremendously useful to develop applications and devices.

The control scheme using coherent optical effects has been implemented here with some simplifications. These calculations may be improved by including the modulation of the incident field by the dispersive permittivity of the medium. The effect of disorder may also be modelled by defining a super-cell which contains non-identical metamaterial units and then applying periodic boundary conditions using the Transfer Matrix

Method. Further in our treatment the coherent effects all over the metamaterial are assumed to develop from a homogeneous pump field. A rigorous calculation of the inhomogeneous pump field and incorporation of this inhomogeneity into the modelling of coherent effects would be necessary for a full description of this effect. Additionally effects that are nonlinear in the probe field also required to be modelled. Similarly, the plasma-like behaviour, which has already been shown to be independent of the distribution of nanoparticles in the unit cell, can be further investigated to model the variations of the effective plasma frequency beyond the simple bulk averaging used in this thesis. For higher filling fractions, deviations from this model are expected, upto the percolation threshold.

Checkerboard structures of negative and positive index media can be built in different configurations. As long as they are optically complementary to each other, they are expected to be perfectly transmittive for all propagating and evanescent waves. In three dimensions, checkerboards present a much richer set of physical phenomena. The behaviour of three dimensional systems may be studied numerically. One may also investigate them in non-Euclidean geometries. Checkerboards give rise to very singular fields (large local field enhancements) as well as very singular density of states (large changes to emission probabilities). Investigation of these effects for various configurations of checkerboards can result in myriad applications like control and enhancement of fluorescence emission, surface enhanced Raman scatterings (SERS) and other plasmonic effects with checkerboard systems.

Appendix: Transfer Matrix Method

The PHOTON code, based on the Transfer Matrix Method was developed by Sir John Pendry *et. al.* at the Imperial College, London. The method works on a fairly simple principle: If one knows the electric and the magnetic fields in the $x-y$ plane at $z=0$, then Maxwell's equations may be used to determine the electric and the magnetic fields at $z=c$ in the $x-y$ plane. In mathematical terms, this may be represented as:

$$\mathbf{F}(z=c) = \mathbf{T}(c,0)\mathbf{F}(z=0), \tag{6.1}$$

where $\mathbf{T}$ is the transfer matrix and $\mathbf{F}$ may represent either the electric or the magnetic fields. The transfer matrix thus defines the propagation of wavefields across a slab of material and so it is also useful in determining the reflection and the transmission coefficients of the slab. If one considers an infinite medium formed by repeating the slab periodically, the Bloch condition can be applied:.

$$\exp(iKc)\mathbf{F}(z=0) = \mathbf{F}(z=c) = \mathbf{T}(c,0)\mathbf{F}(z=0), \tag{6.2}$$

and determine the dispersion $K(\omega)$ from the eigenvalues of the $\mathbf{T}$ matrix.

A discrete form of Maxwell's equations on a lattice is employed in the numerical implementation of this computational scheme [76]. The various algorithms employed in the code have been described in detail in Ref. [137]. In Fig. 6.1, we present a diagrammatic representation of the various steps involved in numerically solving Maxwell's equations on a lattice to determine either the band-structure or the transmission and the reflection coefficients of the medium.

Maxwell's equations are solved according to the scheme outlined in Fig. 6.1 to obtain the band structure or the reflection and the transmission coefficients. In order to determine the reflection and and transmission properties of a slab consisting of multiple layers, the transmission and reflection coefficients are determined for each layer and

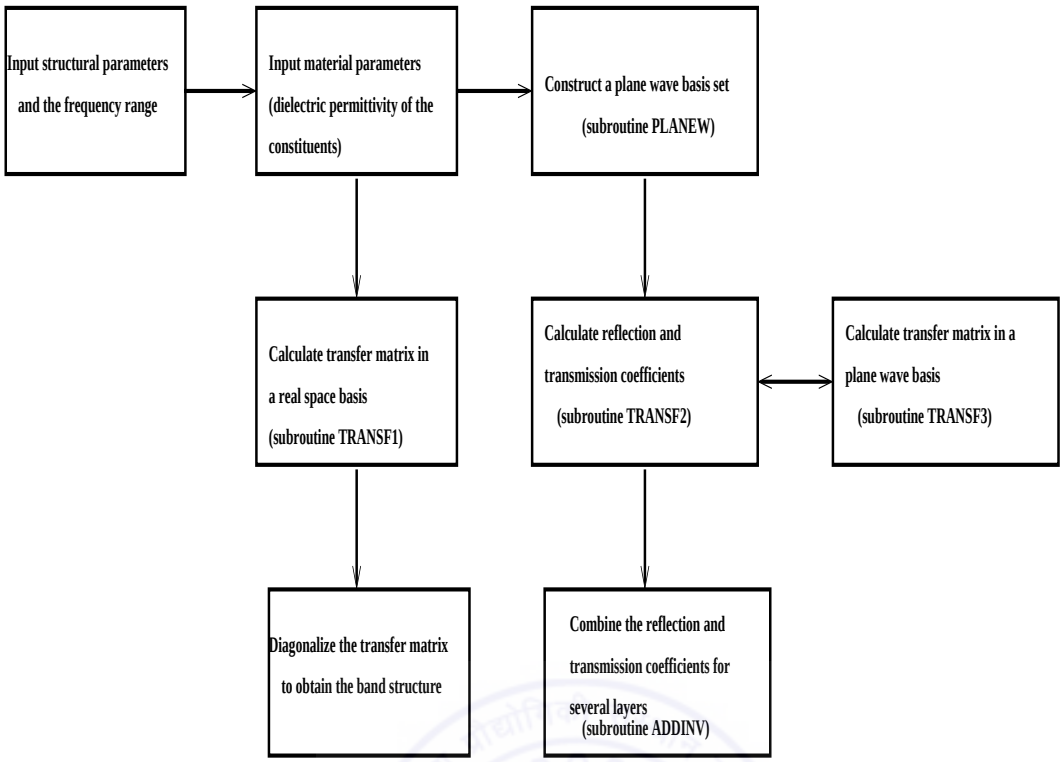

Figure 6.1: Schematic representation of the PHOTON code based on the Transfer Matrix Method. The details of the subroutines (named in capitals), can be found in Ref. [137].

then combined using a multiple scattering formalism. This is done in order to avoid the numerical instabilities that result when the z-stepping exceeds a certain number of points.

Bibliography

[1] V. G. Veselago. *The Electrodynamics of Substances with Simultaneously Negative Values of ϵ and μ. Soviet Physics Uspekhi*, 10:509–514, 1968.

[2] R. A. Shelby, D.R. Smith, and S. Schultz. *Experimental Verification of a Negative Index of Refraction. Science*, 292:77–79, 2001.

[3] C. G. Parazzoli, R. B. Greegor, K. Li, B. E. C. Koltenbah, and M. Tanielian. *Experimental Verification and Simulation of Negative Index of Refraction Using Snell's Law. Phys. Rev. Lett.*, 90:107401–107404, 2003.

[4] Jie Lu, Tomasz Grzegorczyk, Yan Zhang, Joe Pacheco Jr., Bae-Ian Wu, Jin Kong, and Min Chen. *Cerenkov radiation in materials with negative permittivity and permeability. Opt. Express*, 11:723–734, 2003.

[5] Chiyan Luo, Mihai Ibanescu, Steven G. Johnson, and J. D. Joannopoulos. *Cerenkov Radiation in Photonic Crystals. Science*, 299:368–371, 2003.

[6] Jin Au Kong, Bae-Ian Wu, and Yan Zhang. *Lateral displacement of a Gaussian beam reflected from a grounded slab with negative permittivity and permeability. Applied Physics Letters*, 80:2084–2086, 2002.

[7] P. R. Berman. *Goos-Hänchen shift in negatively refractive media. Phys. Rev. E*, 66:067603 – 067605, 2002.

[8] R. W. Ziolkowski. *Pulsed and CW Gaussian beam interactions with double negative metamaterial slabs. Optics Express*, 11:662–681, 2003.

[9] J. D. Jackson. *Classical Electrodynamics*. John Wiley, 1988.

[10] J. B. Pendry, A. J. Holden, D. J. Robbins, and W. J. Stewart. *Magnetism from conductors and enhanced nonlinear phenomena. IEEE Transactions on Microwave Theory and Techniques*, 47:2075–2084, 1999.

[11] J. B. Pendry. *Negative Refraction makes a Perfect Lens. Physical Review Letters*, 85:3966–3969, 2000.

[12] D. R. Smith, Willie J. Padilla, D. C. Vier, S. C. Nemat-Nasser, and S. Schultz. *Composite Medium with Simultaneously Negative Permeability and Permittivity. Phys. Rev. Lett.*, 84:4184–4187, 2000.

[13] A. L. Pokrovsky and A. L. Efros. *Electrodynamics of Metallic Photonic Crystals and the Problem of Left-Handed Materials. Phys. Rev. Lett.*, 89:093901, 2002.

[14] R. Marqués and D. R. Smith. *Comment on "Electrodynamics of Metallic Photonic Crystals and the Problem of Left-Handed Materials". Phys. Rev. Lett.*, 92:059401, 2004.

[15] S. A. Ramakrishna. *Physics of negative refractive index materials. Reports on Progress in Physics*, 68:449–521, 2005.

[16] S. A. Ramakrishna and T. M. Grzegorczyk. *Physics and Applications of Negative Refractive Index Materials*. CRC Press, Boca Raton, U. S. A. , 2009.

[17] Nader Engheta and Richard W. Ziolkowski. *Metamaterials: Physics and Engineering Explorations*. Wiley-IEEE Press, New York, U.S.A., 2006.

[18] G. V. Eleftheriades and K. G. Balmain. *Negative-Refraction Metamaterials: Fundamental Principles and Applications*. Wiley-IEEE Press, 2006.

[19] J. D. Joannopoulos, S. G. Johnson, J. N. Winn, and R. D. Meade. *Photonic Crystals: Molding the Flow of Light*. Princeton University Press, Cambridge, U.S.A. 185 p., 1995.

[20] K. Sakoda. *Optical Properties of Photonic Crystals.* Springer, Berlin, First Edition, 2001.

[21] F. D. M. Haldane. *Electromagnetic Surface Modes at Interfaces with Negative Refractive Index make a "Not-Quite-Perfect" Lens. arXiv:cond-mat/0206420v3.*

[22] J. B. Pendry and S. A. Ramakrishna. Focussing Light using Negative Refraction. *J. Phys. Cond. Matter*, 15:6345–6364, 2003.

[23] A. J. Ward and J. B. Pendry. *Refraction and geometry in Maxwell's equations. Journal of Modern Optics*, 43:773–793, 1996.

[24] J. B. Pendry and S. A. Ramakrishna. *Near field lenses in two dimensions . J. Phys. Cond. Matter*, 14:8463–8479, 2002.

[25] S. Anantha Ramakrishna and J. B. Pendry. *Spherical perfect lens: Solutions of Maxwell's equations for spherical geometry. Phys. Rev. B*, 69:115115–115121, 2004.

[26] M. Notomi. *Negative refraction in photonic crystals. Optical and Quantum Electronics*, 34:133–143, 2002.

[27] J. C. Maxwell Garnett. *Colours in metal glasses and in metallic films. Phil. Trans. R. Soc. London*, 203:385–420, 1904.

[28] R. Ruppin. *Evaluation of extended Maxwell-Garnett theories. Optics Communications*, 182:273–279, 2000.

[29] William T. Doyle. *Optical properties of a suspension of metal spheres. Phys. Rev. B*, 39:9852–9858, 1989.

[30] Craig F. Bohren. *Do extended effective-medium formulas scale properly? Journal of Nanophotonics*, 3:039501–039503, 2009.

[31] W. Lamb, D. M. Wood, and N. W. Ashcroft. *Long-wavelength electromagnetic propagation in heterogeneous media. Phys. Rev. B*, 21:2248–2266, 1980.

[32] C. G. Granqvist and O. Hunderi. *Optical properties of Ag-SiO2 Cermet films: A comparison of effective-medium theories. Phys. Rev. B*, 18:2897–2906, 1978.

[33] David R. Smith and John B. Pendry. *Homogenization of Metamaterials by Field Averaging (Invited Paper). J. Opt. Soc. Am. B*, 23:391–403, 2006.

[34] D. R. Smith, S. Schultz, P. Markoš, and C. M. Soukoulis. *Determination of Effective Permittivity and Permeability of Metamaterials from Reflection and Transmission Coefficients. Phys. Rev. B*, 65:195104–195108, 2002.

[35] T. Koschny, P. Markoš, D. R. Smith, and C. M. Soukoulis. *Resonant and Antiresonant Frequency Dependence of the Effective Parameters of Metamaterials. Phys. Rev. E*, 68:065602–065605, 2003.

[36] Xudong Chen, Tomasz M. Grzegorczyk, Bae-Ian Wu, Joe Pacheco, and Jin Au Kong. *Robust method to retrieve the constitutive effective parameters of metamaterials. Phys. Rev. E*, 70:016608–016614, 2004.

[37] P. A. Belov, R. Marqués, S. I. Maslovski, I. S. Nefedov, M. Silveirinha, C. R. Simovski, and S. A. Tretyakov. *Strong spatial dispersion in wire media in the very large wavelength limit. Physical Review B*, 67:113103–113106, 2003.

[38] J. B. Pendry, A. J. Holden, W. J. Stewart, and I. Youngs. *Extremely Low Frequency Plasmons in Metallic Mesostructures. Phys. Rev. Lett.*, 76:4773–4776, 1996.

[39] J. B. Pendry, A. J. Holden, D. J. Robbins, and W. J. Stewart. *Low frequency plasmons in thin-wire structures. Journal of Physics-Condensed Matter*, 10:4785–4809, 1998.

[40] D. Schurig, J. J. Mock, and D. R. Smith. *Electric-field-coupled resonators for negative permittivity metamaterials. Applied Physics Letters*, 88 - 90:041109, 2006.

[41] Sangeeta Chakrabarti and S. Anantha Ramakrishna. *Design of metallic metamaterial structures at high frequencies. Journal of Nonlinear Optical Physics & Materials*, 17:143–158, 2008.

[42] L. D. Landau and E. M. Lifshitz. *Electrodynamics of Continuous Media*. Pergamon Press, 460 p., 1960.

[43] P Gay-Balmaz and O. J. F. Martin. *Efficient Isotropic Magnetic Resonators. Applied Physics Letters*, 81:939–941, 2002.

[44] S. O'Brien and J. B. Pendry. *Magnetic activity at infrared frequencies in structured metallic photonic crystals. Journal of Physics-Condensed Matter*, 14:6383–6394, 2002.

[45] S. O'Brien and J. B. Pendry. *Photonic band-gap effects and magnetic activity in dielectric composites. Journal of Physics-Condensed Matter*, 14:4035–4044, 2002.

[46] V. Yannopapas and A. Moroz. *Negative refractive index metamaterials from inherently non-magnetic materials for deep infrared to terahertz frequency ranges. Journal of Physics-Condensed Matter*, 17:3717–3734, 2005.

[47] R. H. Ritchie. *Plasma Losses by Fast Electrons in Thin Films. Phys. Rev.*, 106:874–881, 1957.

[48] E. A. Stern and R. A. Ferrell. *Surface Plasma Oscillations of a Degenerate Electron Gas. Phys. Rev.*, 120:130–136, 1960.

[49] H. Raether. *Surface-Plasmons on Smooth and Rough Surfaces and on Gratings. Springer Tracts in Modern Physics*, 111:1–133, 1988.

[50] R. Ruppin. *Surface polaritons of a left-handed medium. Physics Letters A*, 277:61–64, 2000.

[51] S. A. Darmanyan, M. Neviere, and A. A. Zakhidov. *Surface modes at the interface of conventional and left-handed media. Optics Communications*, 225:233–240, 2003.

[52] L. Novotny and B. Hecht. *Principles of Nano-Optics*. Cambridge University Press, 2006.

[53] C. F. Bohren and D. R. Huffman. *Absorption and Scattering of Light by Small Particles*. John Wiley, New York, 1983.

[54] W. S. Warren, H. Rabitz, and M. Dahleh. *Coherent control of quantum dynamics - the dream is alive. Science*, 259:1581–1589, 1993.

[55] G. S. Agarwal and W. Harshawardhan. *Inhibition and Enhancement of Two Photon Absorption. Physical Review Letters*, 77:1039–1042, 1996.

[56] M. Shapiro and P. Brumer. *Coherent and incoherent laser control of photochemical reactions . Int. Rev. Phys. Chem*, 13:187–229, 1994.

[57] M. Shapiro, J. W. Hepburn, and P. Brumer. *Simplified laser control of unimolecular reactions: Simultaneous (ω_1, ω_3) excitation. Chem. Phys. Lett.*, 149:451–454, 1988.

[58] Claude Rulliere (Ed.). *Femtosecond Laser Pulses: Principles and Experiments* . Springer, Second Edition, 2005.

[59] S. E. Harris, J. E. Field, and A. Imamoğlu. *Nonlinear optical processes using electromagnetically induced transparency. Phys. Rev. Lett.*, 64:1107–1110, 1990.

[60] K. J. Boller, A. Imamolu, and S. E. Harris. *Observation of electromagnetically induced transparency. Phys. Rev. Lett.*, 66:2593–2596, 1991.

[61] L. J. Wang, A. Kuzmich, and A. Dogariu. *Gain-assisted superluminal light propagation. Nature*, 406:277–279, 2000.

[62] L. V. Hau, S. E. Harris, Z. Dutton, and C. H. Behroozi. *Light speed reduction to 17 metres per second in an ultracold atomic gas. Nature*, 397:594–598, 1999.

[63] C. Liu, Z. Dutton, C. H. Behroozi, and L. V. Hau. *Observation of coherent optical information storage in an atomic medium using halted light pulses. Nature*, 409:490–493, 2001.

[64] D. F. Phillips, A. Fleischhauer, A. Mair, R. L. Walsworth, and M. D. Lukin. *Storage of light in atomic vapor. Phys. Rev. Lett.*, 86:783–786, 2001.

[65] Marlan O. Scully. *Enhancement of the index of refraction via quantum coherence. Phys. Rev. Lett.*, 67:1855–1858, 1991.

[66] A. S. Zibrov, M. D. Lukin, L. Hollberg, D. E. Nikonov, M. O. Scully, H. G. Robinson, and V. L. Velichansky. *Experimental demonstration of enhanced index of refraction via quantum coherence in Rb. Phys. Rev. Lett.*, 76:3935–3938, 1996.

[67] G. Alzetta, A. Gozzini, L. Moi, and G Orriols. *Experimental-Method for Observation of RF Transitions and Laser Beat Resonances in Oriented Na Vapour. Nuovo Cimento Della Societa Italiana Di Fisica B-General Physics Relativity Astronomy and Mathematical Physics and Methods*, 36:5–20, 1976.

[68] Michael Fleischhauer, Atac Imamoglu, and Jonathan P. Marangos. *Electromagnetically induced transparency: Optics in coherent media. Rev. Mod. Phys.*, 77:633–673, 2005.

[69] M. O. Scully and M. S. Zubairy. *Quantum Optics*. Cambridge University Press, 1997.

[70] R. A. Akhmedzhanov, A. A. Bondartsev, L. A. Gushchin, N. A. Zharova, and A. G. Petrosyan. *Electromagnetically induced transparency on Zeeman sublevels in Nd3+:LaF3 crystals. JETP Letters*, 85:389–392, 2007.

[71] Rinat Akhmedzhanov, Lev Gushin, Elena Kuznetsova, Alexander Litvak, Victor Yasenkov, and Nina Zharova. *Experimental observation of electromagnetically induced transparency in Pr3+ : LaF3. Journal of Modern Optics*, 53:2449–2458, 2006. 36th Winter Colloquium on Physics of Quantum Electronics, Snowbird, UT, JAN 02-06, 2006.

[72] W. J. Jones and B. P. Stoicheff. *Inverse Raman Spectra: Induced Absorption at Optical Frequencies. Phys. Rev. Lett.*, 13:657–659, 1964.

[73] A. D. Buckingham. *Theory of the Stimulated Raman and Related Effects. The Journal of Chemical Physics*, 43:25–31, 1965.

[74] S. O'Brien, D. McPeake, S. A. Ramakrishna, and J. B. Pendry. *Near-infrared photonic band gaps and nonlinear effects in negative magnetic metamaterials. Physical Review B*, 69:241101–241104, 2004.

[75] J. B. Pendry and A. MacKinnon. *Calculation of photon dispersion relations. Phys. Rev. Lett.*, 69:2772–2775, 1992.

[76] J. B. Pendry. *Photonic Band Structures. Journal of Modern Optics*, 41:209–229, 1994.

[77] P. B. Johnson and R. W. Christy. *Optical Constants of the Noble Metals. Phys. Rev. B*, 6:4370–4379, 1972.

[78] G. Dolling, C. Enkrich, M. Wegener, J. F. Zhou, C. M. Soukoulis, and S. Linden. *Cut-wire pairs and plate pairs as magnetic atoms for optical metamaterials. Optics Letters*, 30:3198–3200, 2005.

[79] G. Dolling, C. Enkrich, M. Wegener, C. M. Soukoulis, and S. Linden. *Simultaneous negative phase and group velocity of light in a metamaterial. Science*, 312:892–894, 2006.

[80] V. A. Podolskiy, A. K. Sarychev, E. E. Narimanov, and V. M. Shalaev. *Resonant light interaction with plasmonic nanowire systems. Journal of Optics A-Pure and Applied Optics*, 7:S32–S37, 2005.

[81] S. Anantha Ramakrishna, Sangeeta Chakrabarti, and Olivier J. F. Martin. *Metamaterials with negative refractive index at optical frequencies. arXiv.org:physics/0703003*, 2007.

[82] S. A. Ramakrishna and J. B. Pendry. *The asymmetric lossy near-perfect lens. Journal of Modern Optics*, 49:1747–1762, 2002.

[83] Chiyan Luo, Steven G. Johnson, J. D. Joannopoulos, and J. B. Pendry. *All-angle negative refraction without negative effective index. Phys. Rev. B*, 65:201104–201107, 2002.

[84] S. E. Harris. *Electromagnetically induced transparency. Physics Today*, 50:36–42, 1997.

[85] G. G. Padmabandu, G. R. Welch, I. N. Shubin, E. S. Fry, D. E. Nikonov, M. D. Lukin, and M. O. Scully. *Laser oscillation without population inversion in a sodium atomic beam. Physical Review Letters*, 76:2053–2056, 1996.

[86] M. O. Scully, S. Y. Zhu, and A. Gavrielides. *Degenerate quantum-beat laser: Lasing without inversion and inversion without lasing. Phys. Rev. Lett.*, 62:2813–2816, 1989.

[87] J. B. Pendry, D. Schurig, and D. R. Smith. *Controlling electromagnetic fields. Science*, 312:1780–1782, 2006.

[88] D. Schurig, J. J. Mock, B. J. Justice, S. A. Cummer, J. B. Pendry, A. F. Starr, and D. R. Smith. *Metamaterial electromagnetic cloak at microwave frequencies. Science*, 314:977–980, 2006.

[89] Vladimir M. Shalaev. *Optical negative-index metamaterials. Nature Photonics*, 1:41–48, 2007.

[90] Zhongyan Sheng and Vasundara V. Varadan. *Tuning the effective properties of metamaterials by changing the substrate properties. Journal of Applied Physics*, 101:014909 – 014915, 2007.

[91] V. J. Logeeswaran, A. N. Stameroff, M. Saif Islam, W. Wu, A. M. Bratkovsky, P. J. Kuekes, S. Y. Wang, and R. S. Williams. *Switching between positive and negative permeability by photoconductive coupling for modulation of electromagnetic radiation. Applied Physics A-Materials Science & Processing*, 87:209–216, 2007.

[92] Hou-Tong Chen, John F. O'Hara, Abul K. Azad, Antoinette J. Taylor, Richard D. Averitt, David B. Shrekenhamer, and Willie J. Padilla. *Experimental demonstration of frequency-agile terahertz metamaterials. Nature Photonics*, 2:295–298, 2008.

[93] W. J. Padilla, A. J. Taylor, C. Highstrete, Mark Lee, and R. D. Averitt. *Dynamical Electric and Magnetic Metamaterial Response at Terahertz Frequencies. Phys. Rev. Lett.*, 96:107401–107404, 2006.

[94] Douglas H. Werner, Do-Hoon Kwon, Iam-Choon Khoo, Alexander V. Kildishev, and Vladimir M. Shalaev. *Liquid crystal clad near-infrared metamaterials with tunable negative-zero-positive refractive indices. Opt. Express*, 15:3342–3347, 2007.

[95] Jiaguang Han, Akhlesh Lakhtakia, and Cheng-Wei Qiu. *Terahertz metamaterials with semiconductor split-ring resonators for magnetostatic tunability. Opt. Express*, 16:14390–14396, 2008.

[96] T. Driscoll, G. O. Andreev, D. N. Basov, S. Palit, S. Y. Cho, N. M. Jokerst, and D. R. Smith. *Tuned permeability in terahertz split-ring resonators for devices and sensors. Applied Physics Letters*, 91:062511–062513, 2007.

[97] Thomas A. Klar, Alexander V. Kildishev, Vladimir P. Drachev, and Vladimir M. Shalaev. *Negative-index metamaterials: Going optical. IEEE Journal of Selected Topics in Quantum Electronics*, 12:1106–1115, 2006.

[98] Nikolai G. Kalugin and Yuri V. Rostovtsev. *Efficient generation of short terahertz pulses via stimulated Raman adiabatic passage. Optics Letters*, 31:969–971, 2006.

[99] S. H. Autler and C. H. Townes. *Stark Effect in Rapidly Varying Fields. Phys. Rev.*, 100:703–722, 1955.

[100] Mark I. Stockman. *Criterion for Negative Refraction with Low Optical Losses from a Fundamental Principle of Causality. Phys. Rev. Lett.*, 98:177404–177407, 2007.

[101] J. B. Pendry and P. M. Bell. *Transfer Matrix Techniques for Electromagnetic Waves. NATO ASI Series E: Applied Sciences*, 315:203, 1996.

[102] Sangeeta Chakrabarti, S. Anantha Ramakrishna, and Harshawardhan Wanare. *Coherently controlling metamaterials. Optics Express*, 16:19504–19511, 2008.

[103] F. S. Pavone, G. Bianchini, F. S. Cataliotti, T. W. Hänsch, and M. Inguscio. *Birefringence in electromagnetically induced transparency. Opt. Lett.*, 22:736–738, 1997.

[104] W. Vassen. *Laser cooling and trapping of metastable helium: towards Bose-Einstein condensation. Comptes Rendus de l Academie Des Sciences Serie IV Physique Astrophysique*, 2:613–618, 2001.

[105] Hou-Tong Chen, John F. O'Hara, Antoinette J. Taylor, Richard D. Averitt, C. Highstrete, Mark Lee, and Willie J. Padilla. *Complementary planar terahertz metamaterials. Optics Express*, 15:1084–1095, 2007.

[106] W. J. Padilla, M. T. Aronsson, C. Highstrete, Mark Lee, A. J. Taylor, and R. D. Averitt. *Electrically resonant terahertz metamaterials: Theoretical and experimental investigations. Phys. Rev. B*, 75:041102, 2007.

[107] Hou-Tong Chen, Willie J. Padilla, Joshua M. O. Zide, Seth R. Bank, Arthur C. Gossard, Antoinette J. Taylor, and Richard D. Averitt. *Ultrafast optical switching of terahertz metamaterials fabricated on ErAs/GaAs nanoisland superlattices. Opt. Lett.*, 32:1620–1622, 2007.

[108] Hou-Tong Chen, Willie J. Padilla, Joshua M. O. Zide, Arthur C. Gossard, Antoinette J. Taylor, and Richard D. Averitt. *Active terahertz metamaterial devices. Nature*, 444:597–600, 2006.

[109] Michael S. Rill, Christine Plet, Michael Thiel, Isabelle Staude, Georg Von Freymann, Stefan Linden, and Martin Wegener. *Photonic metamaterials by direct laser writing and silver chemical vapour deposition. Nature Materials*, 7:543–546, 2008.

[110] V. M. Shalaev. *Optical negative index materials. Nature Photonics*, 1:41–48, 2006.

[111] Yaroslav A. Urzhumov, Gennady Shvets, Jonathan Fan, Federico Capasso, Daniel Brandl, and Peter Nordlander. *Plasmonic nanoclusters: a path towards negative-index metafluids. Optics Express*, 15:14129–14145, 2007.

[112] Carsten Rockstuhl, Falk Lederer, Christoph Etrich, Thomas Pertsch, and Toralf Scharf. *Design of an Artificial Three-Dimensional Composite Metamaterial with Magnetic Resonances in the Visible Range of the Electromagnetic Spectrum. Phys. Rev. Lett.*, 99:017401–017404, 2007.

[113] D. A. Genov, A. K. Sarychev, V. M. Shalaev, and A. Wei. *Resonant field enhancements from metal nanoparticle arrays. Nano Letters*, 4:153–158, 2004.

[114] Qi Wu and Wounjhang Park. *Negative index materials based on metal nanoclusters. Applied Physics Letters*, 92:153114–153116, 2008.

[115] Roberto Merlin. *Metamaterials and the Landau-Lifshitz permeability argument: Large permittivity begets high-frequency magnetism. Proceedings of the National Academy of Sciences of the United States of America*, 106:1693–1698, 2009.

[116] V. A. Podolskiy, A. K. Sarychev, and V. M. Shalaev. *Plasmon modes in metal nanowires and left-handed materials. Journal of Nonlinear Optical Physics & Materials*, 11:65–74, 2002.

[117] V. M. Shalaev, W. S. Cai, U. K. Chettiar, H. K. Yuan, A. K. Sarychev, V. P. Drachev, and A. V. Kildishev. *Negative index of refraction in optical metamaterials. Optics Letters*, 30:3356–3358, 2005.

[118] Shuang Zhang, Wenjun Fan, N. C. Panoiu, K. J. Malloy, R. M. Osgood, and S. R. J. Brueck. *Experimental Demonstration of Near-Infrared Negative-Index Metamaterials. Phys. Rev. Lett.*, 95:137404–137407, 2005.

[119] Wenshan Cai, Uday K. Chettiar, Hsiao-Kuan Yuan, Vashista C. de Silva, Alexander V. Kildishev, Vladimir P. Drachev, and Vladimir M. Shalaev. *Metamagnetics with rainbow colors. Optics Express*, 15:3333–3341, MAR 19 2007.

[120] A. Alù, A. Salandrino, and N. Engheta. *Negative effective permeability and left-handed materials at optical frequencies. Optics Express*, 14:1557–1567, 2006.

[121] Andrea Alù and Nader Engheta. *Dynamical theory of artificial optical magnetism produced by rings of plasmonic nanoparticles. Phys. Rev. B*, 78:085112–085121, 2008.

[122] S. Tretyakov. *Analytical Modelling in Applied Electromagnetics.* Artech House, 2003.

[123] E. Shamonina, V. A. Kalinin, K. H. Ringhofer, and L. Solymar. *Magnetoinductive waves in one, two, and three dimensions. Journal of Applied Physics*, 92:6252–6261, 2002.

[124] E. Shamonina, V. A. Kalinin, K. H. Ringhofer, and L. Solymar. *Magneto-inductive waveguide. Electron. Lett.*, 38:371–373, 2002.

[125] D. R. Solli, P. Koonath, and B. Jalali. *Inverse Raman scattering in silicon: A free-carrier enhanced effect. Phys. Rev. A*, 79:053853–053856, 2009.

[126] A. Yariv. *Quantum Electronics.* John Wiley and Sons Inc., 1989.

[127] G. Sauer, G. Brehm, S. Schneider, K. Nielsch, R. B. Wehrspohn, J. Choi, H. Hofmeister, and U. Gosele. *Highly ordered monocrystalline silver nanowire arrays. Journal of Applied Physics*, 91:3243–3247, 2002.

[128] Q. Zhou, Z. Li, Y. Yang, and Z. Zhang. *Arrays of aligned, single crystalline silver nanorods for trace amount detection. J. Phys. D:Appl. Phys.*, 41:152007, 2008.

[129] Justin Elser, Robyn Wangberg, Viktor A. Podolskiy, and Evgenii E. Narimanov. *Nanowire metamaterials with extreme optical anisotropy. Applied Physics Letters*, 89:261102 – 261104, 2006.

[130] A. I. Rahachou and I. V. Zozoulenko. *Light propagation in nanorod arrays. J. Opt. A: Pure Appl. Phys.*, 9:265–270, 2007.

[131] A. Bratkovsky, E. Ponizovskaya, S. Y. Wang, P. Holmstrom, L. Thylen, Y. Fu, and H. Agren. *A metal-wire /quantum-dot composite metamaterial with negative ϵ and compensated optical loss. Appl. Phys. Lett.*, 93:193106–193108, 2008.

[132] T. G. Mackay and A. Lakhtakia. *On the application of homogenization formalisms to active dielectric composite metamaterials. Opt. Commun.*, 282:2470–2475, 2009.

[133] G. S. Agarwal and Robert W. Boyd. *Elimination of the band gap of a resonant optical material by electromagnetically induced transparency. Phys. Rev. A*, 60:R2681–R2684, 1999.

[134] S. E. Harris. *Electromagnetically induced transparency in an ideal plasma. Phys. Rev. Lett.*, 77:5357–5360, 1996.

[135] G. Blendstrup, D. Bershader, and P. W. Langhoff. *Resonance refractivity studies of sodium vapor for enhanced flow visualization. AIAA Journal*, 16:1106–1108, 1978.

[136] A. S. Zibrov, M. D. Lukin, L. Hollberg, D. E. Nikonov, M. O. Scully, H. G. Robinson, and V. L. Velichansky. *Experimental Demonstration of Enhanced Index of Refraction via Quantum Coherence in Rb. Phys. Rev. Lett.*, 76:3935–3938, 1996.

[137] P. M. Bell, J. B. Pendry, L. M. Moreno, and A. J. Ward. *A Program for Calculating Photonic Band Structures and Transmission Coefficients of Complex Structures. Computer Physics Communications*, 85:306–322, 1995.

[138] S. Guenneau, B. Gralak, and J. B. Pendry. *Perfect corner reflector. Optics Letters*, 30:1204–1206, 2005.

[139] S. P. Apell, P. M. Echenique, and R. H. Ritchie. *Sum rules for surface plasmon frequencies. Ultramicroscopy*, 65:53–60, 1996.

[140] D. R. Smith, D. Schurig, M. Rosenbluth, S. Schultz, S. A. Ramakrishna, and J. B. Pendry. *Limitations on subdiffraction imaging with a negative refractive index slab. Applied Physics Letters*, 82:1506–1508, 2003.

[141] R. Merlin. *Analytical solution of the almost-perfect-lens problem. Applied Physics Letters*, 84:1290–1292, 2004.

[142] Richard W. Ziolkowski and Ehud Heyman. *Wave propagation in media having negative permittivity and permeability. Phys. Rev. E*, 64:056625–056639, 2001.

[143] S. A. Cummer. *Simulated causal subwavelength focusing by a negative refractive index slab. Applied Physics Letters*, 82:1503–1505, 2003.

[144] Sebastien Guenneau and S. Anantha Ramakrishna. *Negative refractive index, perfect lenses and checkerboards: Trapping and imaging effects in folded optical spaces. Comptes Rendus Physique*, 10:352–378, 2009.

[145] Jianbing J. Chen, T. M. Grzegorczyk, B. I. Wu, and J. A. Kong. *Limitation of FDTD in simulation of a perfect lens imaging system. Optics Express*, 13:10840–10845, 2005.

[146] S. Guenneau, A. C. Vutha, and S. A. Ramakrishna. Negative refraction in 2D checkerboards related by mirror antisymmetry and 3D corner lenses. *New Journal of Physics*, 7:164–172, 2005.

[147] S. Anantha Ramakrishna, S. Guenneau, S. Enoch, G. Tayeb, and B. Gralak. *Confining light with negative refraction in checkerboard metamaterials and photonic crystals. Phys. Rev. A*, 75:063830–063835, 2007.

[148] A. A. Sukhorukov, I. V. Shadrivov, and Y. S. Kivshar. *Wave scattering by metamaterial wedges and interfaces. International Journal of Numerical Modelling-Electronic Networks Devices and Fields*, 19:105–117, 2006.

[149] X. S. Rao and C. K. Ong. *Subwavelength imaging by a left-handed material superlens. Phys. Rev. E*, 68:067601–067603, 2003.

[150] Sangeeta Chakrabarti, N. Shukla, S. Anantha Ramakrishna, S. Dhamodharan, V. N. Kulkarni, S. Guenneau, Fanny Guenneau, and Stefan Enoch. *Visible transmission of light through gold nano-checkerboards: Theory and experiments. Current Science (in preparation)*, 2010.

[151] A. Bossavit. *Solving Maxwell Equations in a Closed Cavity, and the Question of Spurious Modes. IEEE Transactions on Magnetics*, 26:702–705, 1990.

[152] J. P. Berenger. *A Perfectly Matched Layer for the Absorption of Electromagnetic Waves. Journal of Computational Physics*, 114:185–200, 1994.